THERMO-MECHANICAL PROCESSING AND CRYSTALLOGRAPHIC
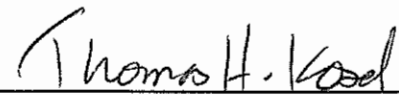
TEXTURE IN SUPER ALPHA-2 TITANIUM ALUMINIDE

A Thesis

Submitted to the Graduate School

of the University of Notre Dame

in Partial Fulfillment of the Requirments

for the Degree of

Master of Science

in Materials Science and Engineering

by

Richard George Rateick, Jr., BSME, P.E.

Thomas H. Kosel

Thomas H. Kosel, Director

Department of Chemical Engineering

Notre Dame, Indiana

November, 1994

DEDICATION

This thesis is dedicated to my parents Richard, Sr. and Barbara Rateick who gave me a family heritage rich in engineering, and with it the understanding that engineering is in the service of improving mankind's life in God's world.

TABLE OF CONTENTS

LIST OF TABLES

LIST OF FIGURES

ACKNOWLEDGEMENTS

CHAPTER 1

INTRODUCTION

Conventional titanium alloys are typically considered elevated temperature materials. However, with only few exceptions, these alloys are limited to 538°C by creep, and 593°C by oxidation resistance. In comparison, the superalloys can reach service temperatures of almost 1100°C on both counts. To the weight conscious aerospace industry, the density of superalloys, being nearly double that of titanium alloys, is significantly detrimental to their application. As a response, the Air Force has funded significant activity to develop intermetallic alloys in general,[1] and intermetallic titanium aluminide alloys specifically.[2] Much of this development has been determined to be "Critical Technology," and hence, has not been reported in the free literature.

The assessed binary Ti-Al phase diagram is presented in Figure 1.[3] Of significant importance to the research reported here is the peritectoid phase transformation from α to β and the ordering of α to α_2. As is developed in greater detail in latter sections, the β to $\alpha + \beta$ phase boundary can be significantly influenced by alloying additions. This phase boundary is referred to as the β transus. The corresponding boundary between the $\alpha + \beta$ and α phase fields is referred to as the α transus.

1
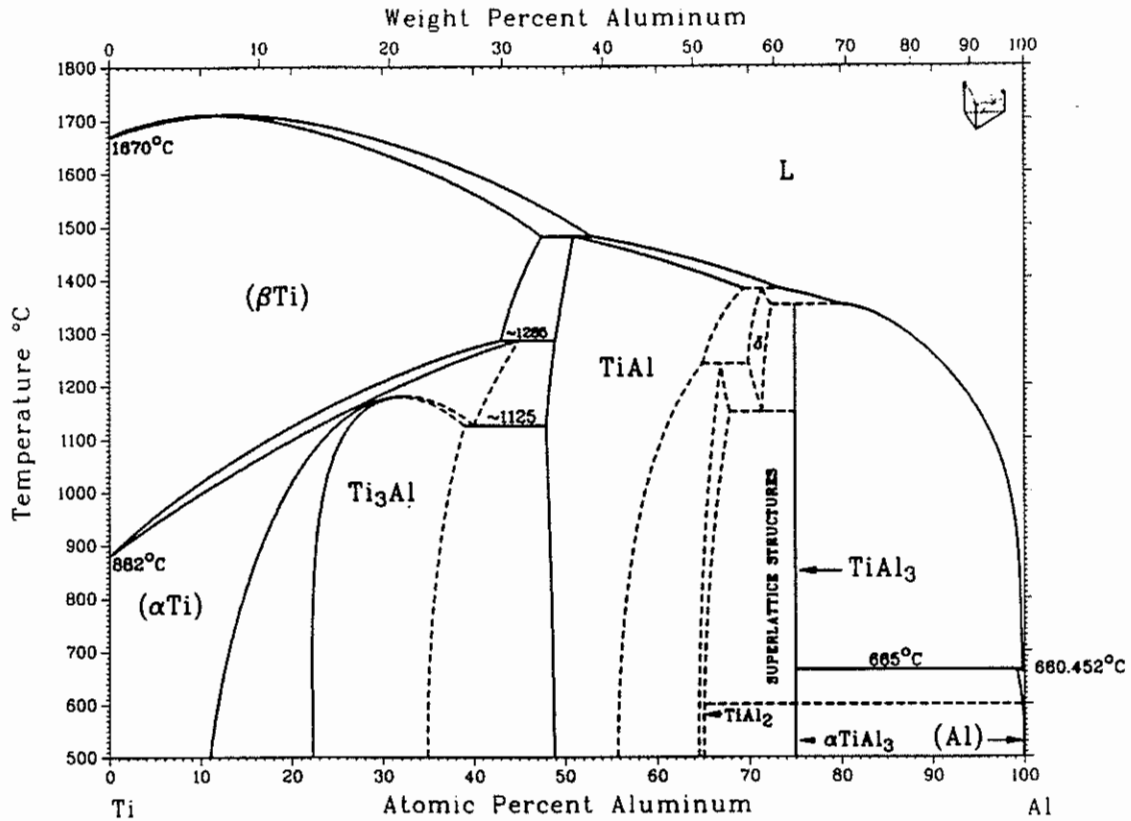
Figure 1
Assessed binary Ti-Al phase diagram.[3]

Titanium aluminide alloy development has focused on three intermetallic compounds: Ti_3Al (alpha 2, α_2), TiAl (gamma, γ), and $TiAl_3$. The γ based alloys were initially targeted for 1038°C applications and the α_2 alloys for 650°C applications.[2] While initial (pre-1972) research came to the conclusion that the α_2 intermetallic was unsuitable for structural alloys,[1] by the beginning of this thesis research project in 1989, the α_2 alloys were arguably the most extensively developed of the intermetallic based systems. The key was the recognition that stabilization of β titanium was necessary to

achieve acceptable ductility, with addition of Nb being foremost contributor.[1] The alloy*
Ti-24Al-11Nb was developed in 1975, followed by Ti-25Al-10Nb-3V-1Mo in 1982.[4]
While literally hundreds of alloys have been considered to date, these remain the only
commercially available α_2 titanium aluminide based materials.

Aluminum is an α stabilizer in Ti, as are most simple metals. This is evident in
the phase diagram shown in Figure 1. The transition metals, however, are typically β
stabilizers.[13] The Nb was thus added to the binary alloy as a β stabilizer with the intent
to provide room temperature ductility not observed in the ordered α_2 phase. The Nb,
however, significantly negates the reduced density which obtains from high Al
concentrations. Vanadium, with a density of 5.8 g/cc vs. 8.55 g/cc for Mo and 2.70 g/cc
for Al, was added both to reduce the alloy density and to allow use of Ti-V master alloys.
An interim composition of Ti-25Al-(10-12)Nb-(2-4)V resulted, however, it did not meet
United States Air Force property goals: tensile properties of near-α Ti-6Al-2Sn-4Zr-2Mo,
and creep rupture of the cast nickel based alloy Inconel 713C (Ni-12.50Cr-4.20Mo-
2.20(Nb-Ta)-6.10Al-0.80Ti-0.12C-0.012B-0.10Zr).[4]

The potencies of β stabilizers and the elastic shear moduli of alloys have been
directly related to the electron/atom ratio in the alloy. Thus, at a given composition, the
farther to the right in the periodic table from Ti, the greater the β stabilizing potency and

---

* Alloy compositions are stated in the convention of the titanium industry.
Intermetallic alloys are defined by compositions in mole percent. Conventional alloys are
defined by compositions in weight percent. After the first reference, the element symbols
are omitted.

elastic shear modulus.[13] Molybdenum, being a more potent β stabilizer than V, was added with the effect of increasing the tensile modulus.[4] Of the β stabilizers, Mo has the greatest effect on reducing creep rate.[5] The result was the composition Ti-25Al-10Nb-3V-1Mo, which met the property goals. It is interesting that, in the end, the densities of the initial ternary vs. the final quintinary alloys were identical: 0.156 lb/in^3. The β transus for this alloy was found to be in the range of 1065°C to 1093°C.[4]

The alloy Ti-25-10-3-1 was identified in 1989 as a material offering significant potential to reduce the weight of gas turbine engine control system components. Engine actuators were the initial target component. This thesis project grew from the recognition that, while the alloy was commercially available, no standard means of converting billet to forged product existed. Thus, the primary focus of this research was to develop and characterize a thermo-mechanical processing schedule for billet conversion. It was decided that creep resistance vs. ductility should be the principal guide to development of thermo-mechanical processing (TMP) technology.

This thesis describes the development rationale and results of TMP, beginning with billet mill product form. The remaining chapters then address the development of crystallographic texture, as detected through metallographic, tensile, and x-ray diffraction investigations of the forged product.

CHAPTER 2

THERMO-MECHANICAL PROCESSING

Thermo-mechanical processing is essential to achieve desired mechanical properties. Blackburn and Smith,[4] in the original work on Ti-25-10-3-1 retrospectively emphasized the importance of the ingot breakdown process. Since the starting material for the present work was commercial mill product, little control over mill proprietary ingot and billet processing was possible. However, subsequent thermo-mechanical processing decisions were controllable within the scope of this project, which could have a decided impact on achieving a material balancing creep resistance with low temperature ductility, fracture toughness and fatigue resistance.

The following is a review of the literature on thermo-mechanical processing of Ti alloys, focusing on the selection of thermo-mechanical processing methods and parameters for use in the project. The actual thermo-mechanical processing schedule is then presented, followed by results and discussion concerning the forging campaign. Lacking thermo-mechanical processing information at the start of this project, it was necessary to develop a process schedule based on the literature and references to processing of other Ti alloys.

The striking similarity of processing effects on the intermetallic and disordered alloys justified the latter point.

2.1   Thermo-Mechanical Processing Background

The first Ti forging was made in October 1949 at the U.S. Naval Gun Factory.[6] Since then, forging has provided the primary method of forming Ti components.[7] For the α_2 aluminides, forging, as opposed to casting, has been central to the achievement of microstructure and property control. For the present investigation, the shape of the forging was not critical, hence, open die upset forging (pancake forging) was the process of choice, as flow was predictable and no die fabrication costs were incurred. This section is divided to discuss the thermo-mechanical processing technology variables and their effects on properties of the alloy.

2.1.1   Thermo-Mechanical Processing Technology Variables

The three upset forging processes are: conventional cold/warm die forging, hot die forging, and isothermal forging; each increasing control over parameter optimization. The primary factors for control of the forging operation are:

- Forging phase field (temperature)
- Temperature control (temperature as a function of time)
- Strain Rate
- Atmosphere
- Upset Ratio

6

Titanium alloys can be forged in either the $\alpha + \beta$ ($\alpha_2 + \beta$ for the intermetallic alloys) or the β phase fields. In general, forging above the β transus significantly reduces the flow stress (analogous here to forging pressure), reduces susceptibility to cracking, increases strain- rate, and improves die-fill for complex shapes.[31,7,8] While no comparative data has been located for the Ti-25-10-3-1 alloy, data from Coyne[8] for Ti-6Al-4V ($\alpha + \beta$ alloy) gives flow stress reductions from 21% to 56% for forging above vs. below the β transus. This can significantly reduce the press size required for a job. The reduced flow stress and strain-rate are attributed to both the significantly higher self-diffusivity of Ti in the β phase[31] (pure Ti: 6.8 x 10^{-13} cm^2·s^{-1} at β - 50°C[*] vs. 4.5 x 10^{-10} cm^{-2}·s^{-1} at β + 50°C)[9] and to the comparative ease of deformation of bcc (β) vs. hcp (α) structures, resulting from differences in the number of available slip systems. However, due to the attendant coarsening, β forging can reduce ductility.

In traditional forging operations, the metal is heated remotely from the dies. Ti alloys are typically not forged with cold dies but rather by dies heated to 260° - 426°C.[10] The thermal conductivity of Ti alloys is typically low, being about one tenth that of steel. Hence, the bulk remains at the forging temperature, while the temperature of the material in immediate contact with the dies drops considerably. Increasing the strain rate lessens the deleterious die cooling effects, but exacerbates two additional problems: adiabatic heating and increased flow stress. Adiabatic heating obtains from internal friction during

---

[*] This notation identifies differential temperature from the specified transus.

7

plastic deformation. At the higher strain rates chosen to minimize die cooling effects, the concomitant higher rate of adiabatic heat generation, coupled with the low thermal conductivity, give rise to significant temperature escalation in the forging. Scanlan and Chambers[7] reported extreme cases where the increase was on the order of 50° - 60°C; well in excess of the $\alpha + \beta$ stability range for many conventional Ti alloys. Adiabatic heating can push the forging temperature over the β transus, resulting in an overheated microstructure -- *defacto* β processing. Consequent lowering of the preheat temperature to counteract adiabatic heating results in significantly increased forging pressure, and the potential of cracking. In Ti-6-4, at a strain rate of 0.083 sec^{-1}, the forging pressure drops at 0.75 MPa/°C on upwardly approaching the β transus[18] (995°C, *c.f.* Coyne[8]). McQuillan and McQuillan[11] proposed that die cooling may be the cause of cracking of the mult[*] at the die/forging interface.

Titanium alloys typically experience significant strain-rate hardening. Cho, *et.al.,*[12] while only investigating the minimal strain-rate dependence of flow stress at room temperature, have inferred that at high temperatures, flow stress in Ti-25-10-3-1 should be highly strain-rate dependent. In the Ti-6-4 alloy, for example, the forging pressure at 950°C was observed to decrease from 110 MPa at 0.3 s^{-1} to 55 MPa at 6 x 10^{-3} s^{-1}.[18]

Reduced forging pressure is not the only effect from low strain-rate deformation, it can also affect the microstructure. If the strain-rate is lowered sufficiently, many Ti

---

[*] A mult is a workpiece at an intermediate forging stage.

alloys exhibit superplastic behavior. Dynamic recrystallization giving small grain size is thebasis for superplasticity in the $\alpha + \beta$ phase field.[13] Superplasticity above the β transus is precluded by coarsening[52] which occurs in titanium alloys. The grain refinement of transformed β, while deleterious to creep, improves ductility. Greenwood, *et.al.*[14] observed grain sizes of <10 μm and minimal grain flow in Ti-6-4 $\alpha + \beta$ forged at strain-rates of 10^{-2} to 10^{-4} s^{-1}. At higher strain-rates up to 10^{-1} s^{-1}, flow of α was observed, whereas α coarsening occurred at strain-rates lower than 10^{-4} s^{-1}. In preliminary work of Dutta and Banerjee,[15] superplastic behavior was observed in Ti-24-11 deformed in the α_2 + β region. Limited metallographic evidence exhibited α_2 coarsening following deformation at 980° and 1020°C under a strain-rate of 3.3×10^{-4} s^{-1}.

Blackburn and Smith,[4] while not performing a parametric study, employed a strain-rate of 1.7×10^{-3} s^{-1} during the first isothermal β forging campaign for Ti-25-10-3-1. The forging pressure ranged from 62 to 33 MPa while upsetting the 200 mm dia. ingot into a 350 mm dia. pancake, at an upset ratio of *ca.* 4.5. Upset ratios from 2 to 4 are recommended for this alloy.[16]

The atmosphere in the forge is also of critical significance, as interstitial elements O and N are alpha stabilizers; the source of "alpha case." The low ductility of the α phase complicates machining, and may cause cracking of the forging. However, embrittlement is typically confined to the surface because of the low diffusivity of these interstitials. Extrapolated from an Arrhenius equation from Quach-Kamimura and Béranger,[17] the

diffusion coefficient for O in CP-Ti is approximately: 1.58×10^{-10} cm$^2 \cdot$s^{-1} at β - 50°C (832°C).

A typical process metallurgical solution is to hot work in a reducing atmosphere. However, as far back as 1956, McQuillan and McQuillan[5, 11] recognized the severity of hydrogen embrittlement in Ti alloys. In due deference to α-case, it is recommended practice to forge in a slightly oxidizing atmosphere, rather than reducing,[7] to avoid the bulk hydrogen embrittlement. The α-case can be removed by pickling, a preferred process to grinding, which can efface surface cracks.[7]

Hot die forging partially addresses the die cooling problems. Die temperatures are typically 110° - 225°C below the billet temperature.[18] Since die chill is substantially reduced, lower strain-rate is possible, giving rise to both reduced adiabatic heating and forging pressures. However, strain-rates still have a lower limit controlled by cooling rate.

In the isothermal forging process, both the dies and the sample are conventionally heated to the forging temperature, thereby eliminating die cooling effects. Atmosphere control is typically provided to prevent embrittlement or α-case formation. Cameron Iron Works employs an N$_2$ atmosphere for isothermal forging in its production press,[19] addressing the hydrogen embrittlement problem, but not eliminating α-case and possible cracking. Wyman-Gordon isothermally forges *invacuo*,[20] effectively eliminating the α stabilizing and embrittling effects from terrestrial gas exposure.

Strain-rate control is the key to obtaining good forgings. The advent of isothermal forging freed the process metallurgist to exploit the low strain-rates conducive to low forging pressure, minimal adiabatic heating, controlled grain morphology and improved die fill. The metallurgical (not economic) significance of in-process time is significantly diminished. With the ordered alloys, and their attendant low ductility at low temperatures, the importance of isothermal forging cannot be overemphasized.

The successful application of the process to complex shapes was first demonstrated by Watmough, *et.al.*[21] on F-111 nose wheels made from Ti-6Al-6V-2Sn. However, the process is not without a shortcoming. The high die temperature necessitates use of superalloy die material, with its underlying fabricating difficulty. Also, the increased time-at-temperature requires improved lubricants with greater thermal stability and less reactivity with the alloys. Conventional forges must also be retrofitted with heating and atmosphere control systems. Much of Watmough *et.al.*'s[21] work centered on these issues. However, even with the added complexity, the economics of isothermal forging have been steadfastly demonstrated.[18,22,23]

Blackburn and Smith[4] succeeded in isothermally forging Ti-25-10-3-1 without cracking. Pancake forgings were made directly from the ingot in Wyman-Gordon's 3000 ton isothermal press. Post forge heat treatment was 1150°C/1 hr/salt quench to 815°C/0.5°C·s^{-1} air cool. Microstructure and creep properties observed in this study are discussed later.

2.1.2 Thermo-Mechanical Processing Effects on Properties

Mechanical property control obtains from the significant microstructural variation following processing above and below the β transus. Since complete metallographic studies of Ti-25-10-3-1 following various forging and heat treat operations have not been reported, the following discussion relies heavily on results for conventional Ti alloys. Indeed, Bassi and Peters[24] have concluded from rolling studies on Ti-25-10-3-1 that microstructural effects on strength and ductility correlate well with conventional β stabilized alloys, thus providing some justification for this approach.

Initially, it may seem more appropriate to separate discussion of forging schedule and post forging heat treatment schedule; however, the literature available does not lend itself to this approach. Instead the two are treated as a unified thermo-mechanical process with variables consisting of:

- Forging phase field (temperature)

- Heat treating phase field (temperature)

- Cooling rate from the heat treat temperature

The thermo-mechanical processing schedule derives from mechanical property trade studies. Here, creep resistance is the goal, however, this is traded against room temperature ductility, and to a lesser extent fracture toughness and fatigue resistance. An

attempt has been made to unify the microstructural descriptions, conforming to a proposed AMS[*]-SAE Recommended Practice.[25]

Much of the processing work performed to date preceded the development of a time temperature transformation (TTT) diagram. Peters and Bassi[26] have proposed the first TTT diagram for Ti-25-10-3-1, which is shown schematically in Figure 2. The TTT diagram assumes instantaneous cooling to an isothermal transformation temperature. As such, the diagram may be useful for describing transformations during isothermal forging, although it does not include the strain enhancement of diffusion rates. However, due to the bulk size of the forged pancake, and Ti's low thermal conductivity, the TTT diagram is of little use in analyzing post forge annealing/quenching operations. Here, a continuous cooling transformation (CCT) diagram is necessary.

An approximate CCT diagram was derived using the method described by Brick, *et.al.*[27] from Peters and Bassi's[26] TTT diagram. It was assumed that the CCT is delayed relative to the isothermal transformation. It was further assumed that the extent of transformation given by cooling over an interval of time along the cooling curve equals that on the TTT curve at the mean temperature of the metal over the same time interval. The start of transformation along a cooling curve was identified by continued cooling over a time interval starting at the cooling curve intersection with the isothermal curve and ending such that the mean temperature traversed over the time interval corresponds

---

[*] Aerospace Material Specification, controlled by the Society of Automotive Engineers.

13

to a point on the TTT curve for isothermal cooling over the same time interval. In practice, the time interval is arbitrarily chosen and subsequently iterated until both the time interval and the corresponding mean temperature over the cooling interval define a point lying on the TTT curve. The CCT curve is then the line joining these graphically determined points on each of the cooling curves. This is a graphical procedure.

The low room temperature ductility in Ti_3Al based alloys results from the ordered structure of the α_2 (DO_{19}). The low room temperature ductility of the α_2 phase has been attributed to limited availability of slip systems and slip planarity,[28] typical of hcp metals.

As discussed, a principal alloying objective is to increase the room temperature ductility. This is achieved by stabilizing the β phase which is bcc if disordered and takes on the B2 (CsCl) structure when ordered. Although β is ordered (B2) in the Ti-25-10-3-1 alloy, the strain compatibility of the cubic structure exceeds that of the DO_{19} (hcp) α structure. Therefore, it would seem appropriate to forge within the β phase field followed by a fast quench to maximize retained β phase-fraction.

However, β forging is typified by significant coarsening,[8] as expected from the data previously discussed. For Ti-25.7Al-12.9Nb (at%), Rowe, et.al.[30] showed grain sizes of 6-8 μm following $\alpha_2 + \beta$ annealing for 1 hour at 1040°C, compared to 300 μm for material β annealed for 1 hour at 1135°C. In a review paper, Flower[31] shows that in conventional $\alpha + \beta$ Ti alloys, β processing halves the ductility. The lower ductility was attributed to enhanced void nucleation in materials with large microstructural unit size,

14
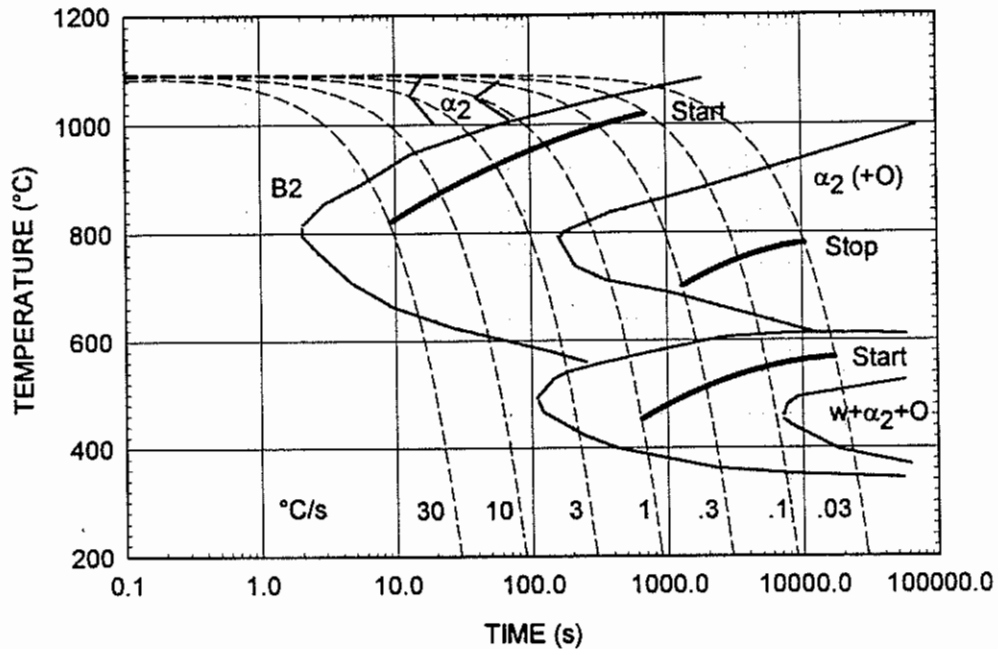
Figure 2
TTT diagram[26] and derived CCT diagram for Ti-25-10-3-1.

including prior β grain size, α platelet size. The deleterious effect of large prior β^* grain

size on ductility has also been observed in Ti-25-10-3-1 type alloys.[32] The coarsening

induced embrittlement overwhelms any ductilizing effect of increased β phase fraction

resulting from β forging. Since room temperature ductility is a critical manufacturing.

assembly, and maintenance issue, $\alpha_2 + \beta$ forging is thus desirable by default. In may

cases, β solution treatment follows $\alpha_2 + \beta$ forging. The intent is to increase the β phase

---

* In $\alpha + \beta$ titanium alloys, heat treatment above the β transus and subsequent
cooling gives rise to a microstructure where the grain boundaries of the prior high
temperature β phase remain evident as defined by precipitation of α. These are referred
to as prior β grain boundaries.

fraction to improve ductility without increasing the prior β grain size to the extent associated with β forging.[33]

Creep resistance is the *raison d'être* for this alloy. While several creep studies have been performed on the Ti-25-10-3-1 alloy, a uniform thermo-mechanical processing schedule has yet to be defined which optimizes for creep resistance. Blackburn and Smith[4] reported the first creep results. Post β forging β heat treatment was 1150°C/1 hr./salt quench to 815°C/0.5 hr. air cool. A radial section showed an approximately equiaxed grain structure with average prior βgrain size of 1.5 mm x 2.5 mm. The orientation of the anisotropy was not given. At both the mid radius and at the outside diameter, highly elongated transformed β* grains were observed along the flow direction, with sizes of 2.5 mm x 7.5 mm. The elongated transformed β grains were attributed to lack of recrystallization in the affected areas during the β anneal. Creep and ductility differed for material from equiaxed and elongated transformed β regions, with the larger prior β grain size giving rise to increased creep rupture strength and poorer ductility. The formation of elongated transformed β grains in the flow direction has been noted for generic Ti alloys, following deformation processing.[34] The α_2 precipitate morphology was found to be independent of the elongation of the transformed β grain. While cooling rates were not given, formation of fine Widmanstätten α_2 was consistent with the CCT

---

* Transformed β is what remains after formation of various α phase structures, etc. on cooling below the transus. The boundary of a transformed β grain is a prior β grain boundary.

diagram within the range of practicable cooling rates. While the ingot processing was to Blackburn and Smith's[4] own admission highly suspect, *i.e.*, insufficient working was performed to break down the ingot microstructure, the study demonstrated an important issue: prior β grain morphology greatly affects the creep rate.

Blenkinsop, *et.al.*[5] studied the effect of cooling rate from the β solution temperature on the near-α Ti alloy Ti-6Al-5Zr-0.5Mo-0.25Si (IMI-685). On water quenching (~100°C/s), a martensitic α developed (not germane to Ti-25-10-3-1), leading to dismal creep performance. Typical of Ti alloys,[31,3, 34, 60] slower cooling rates gave rise to increasingly coarser basketweave microstructures[*]. The creep rate likewise decreased directly with cooling rate, showing a minimum with fast furnace cooling rates of ~1°C/s. Progressively slower cooling rates to 0.8 °C/s encouraged increased creep rates.

Bania and Hall[35] investigated the effect of post forging heat treatment temperature on creep resistance. The near-α Ti-6242-Si (Ti-6Al-2Sn-4Zr-2Mo-0.08Si) alloy was warm die $\alpha + \beta$ forged. Subsequent heat treatment at $\beta + 11°$[†], $\beta - 6°$, $\beta - 14°$ and $\beta - 28°$ gave a series of microstructures with equiaxed primary α concentrations of 0%, 7%, 19% and 35%, respectively, in a transformed β matrix. Minimum creep rates[‡] (post primary

---

[*] Basketwheave structures are typified by Widmanstätten plates precipitated in a woven pattern as opposed to in colonies or groups of parallel plates.

[†] β-transus 993°C.

[‡] The minimum creep rate is quoted when a steady state creep rate can not be determined due to lack of a tertiary region. The minimum creep rate is the minimum slope of the creep curve, usually occuring at the end of the test.

creep regime) decreased monotonically with decreasing primary-α phase fraction. This reinforces the notion that β heat treatment improves creep resistance.

Moving on to the aluminides, Mishra and Banerjee[36] investigated the effects of cooling rate from the β solution treatment (1150°C) in Ti-25Al-11Nb. Cooling rates increasing from 0.02 °C/s to 10°C/s decreased the α_2 plate size in the transformed β. A transgranular Widmanstätten microstructure[*] developed at slow cooling rates, transitioning to colony[†] and finally to basketweave with increased cooling rate, as is typical of $\alpha + \beta$ Ti alloys in general.[31,34] Creep rate dependence on cooling rate exhibited the minimum behavior noted by Blenkinsop, et.al.,[5] with the lowest creep rates obtaining at 0.7°C/s (~1°C/s) cooling rates.

The first major investigation of creep in Ti-25-10-3-1 was performed by Cho, et.al.[12] Their work deserves considerable discussion as it relates properties to a variety of processing conditions. Pancakes 4.4 cm thick x 35 cm dia. were forged in the $\alpha_2 + \beta$ phase field, β solution treated and air cooled. Details of TMP were not given. Some material received a second solution treatment either in the β (1150°C/1 hr) or $\alpha_2 + \beta$ (1045°C/1 hr) fields. The duplex annealed samples were cooled at approximately 0.1°C/s, 0.5°C/s or 10°C/s from the β solution temperature to 760°C). The as received

---

[*] Transgranular Widmanstätten implies that the plates traverse the entire prior β grain. This structure is thus one colony of Widmanstätten plates.

[†] The colony microstructure consists of groups of parallel Widmanstätten plates within a prior β grain.

material consisted of a fine Widmanstätten α_2 platelet microstructure with retained ordered β (B2) matrix with 740 μm prior β grain size. The authors say that the microstructure appeared not to show deformation direction dependence. Assuming air cooling is approximately 1-10°C/s, this duplex $\alpha_2 + \beta$ microstructure follows from the CCT diagram given in Figure 2. The microstructure is similar to that obtained by Mishra and Banerjee[36] in the ternary alloy, following similar solution treatment and cooling schedules.

Duplex treated material cooled from the $\alpha_2 + \beta$ phase field exhibited a transformed β matrix containing Widmanstätten α_2 and primary $\alpha_2{}^*$. From the published micrographs, slower cooling rates favored increased α_2 phase fraction as expected from nucleation and growth theory and following the CCT diagram. Cooling rate had little effect on the size or acicularity of the α_2.

The duplex β processed material exhibited the same classic behavior as noted for the ternary aluminide.[36] With 10°C/s air cooling, the α_2 plates were not visible following normal etching practice. Prolonged etching using Kroll's reagent revealed finely dispersed α_2 in a large fraction of retained β. At controlled air cooling rates of 0.5°C·s^{-1}, a fine basketweave microstructure was observed, again with substantial retained β separating the α_2 plates. Finally under 0.1°C·s^{-1} furnace cooling, a coarser colony microstructure resulted. Retained β was expected at all cooling rates considered, based

---

* The primary α_2 was present prior to the $\alpha_2 + \beta$ heat treatment. It is distinguished from the Widmanstätten or acicular α_2 by a more blunted or even equiaxed morphology.

19

on the CCT diagram, Figure 2. Cho, *et.al.*,[12] did not investigate the retained β phase for decomposition products other than α_2.

At 650°C,* the $\alpha_2 + \beta$ duplex processed material exhibited the highest creep rate. In light of less than spectacular tensile strengths, marginally better ductility compared to the β duplex processed material and lower ductility compared to the as received material, the $\alpha_2 + \beta$ solution treatment is not recommended. The creep performance was consistent with other reports.[35]

A more complicated scenario developed for the β duplex annealed product at 650°C. At high stress (414 MPa), the minimum creep rate was observed for material cooled at $0.5°\text{C·s}^{-1}$. However, at stresses of roughly 300 MPa or less, the $0.1°\text{C·s}^{-1}$ cooled material exhibited the lowest creep rate. The transition is evident in a plot of strain-rate $d\varepsilon/dt$ vs. stress σ. The plot given in Figure 3 represents the power law creep equation:

$$\frac{d\varepsilon}{dt} = A\sigma^n e^{\left[\frac{-E_a}{RT}\right]} \tag{1}$$

where A is a constant, n the stress exponent, E_a the apparent activation energy, R the gas constant and T the temperature.

Cho, *et.al.*[12] attributed the transition to a possible change from room temperature to elevated temperature deformation mechanisms. In each case, colonies of Widmanstätten

---

* This is the generally accepted maximum use temperature for the α_2 aluminides.
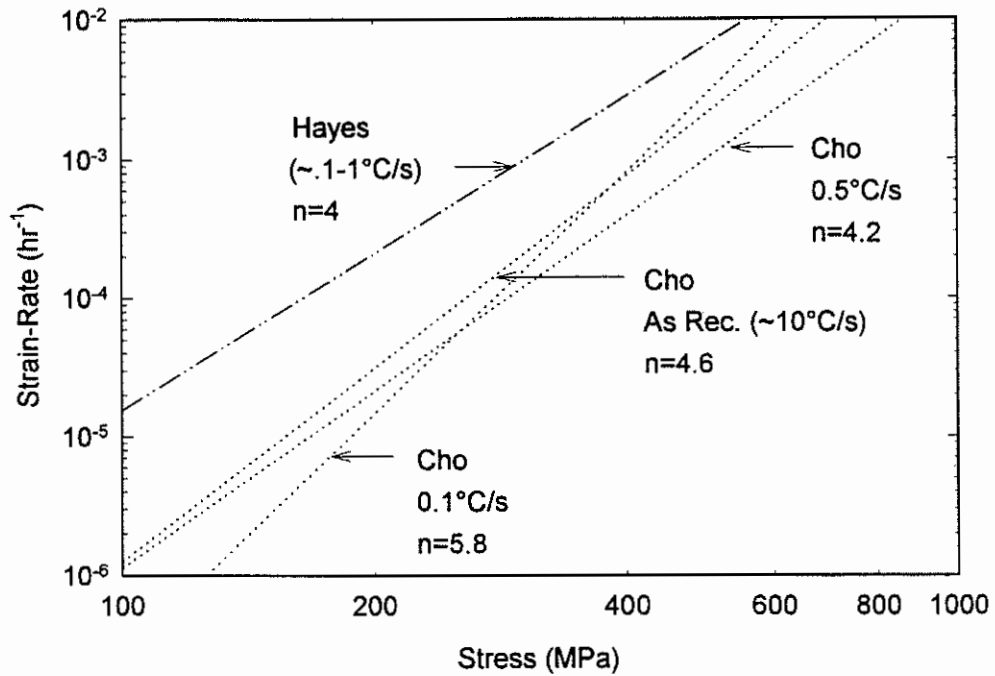
Figure 3
Stress dependence of the strain-rate at 650°C for β solution treated Ti-25-10-3-1, adapted from Cho, *et.al.*[12] and Hayes.[37]

plates exist. It is the coarseness of the colonies that affects the transition. Two factors were identified which affect the high stress creep behavior. The effective slip length, and thus the ease of creep deformation, scaled directly with α_2 plate size and inversely with cooling rate. Ease of creep deformation also scaled directly with retained β phase fraction (sections 3.1), in direct proportion to cooling rate. As these two factors scale oppositely as functions of cooling rate, an optimum microstructure represents a weighted compromise.

Moving up to 750°C, the picture simplifies as shown in Figure 4. Stress and cooling rate interaction is no longer observed. Creep rates for material cooled at 0.1 and within the range of 0.1 to 1°C·s⁻¹ from the duplex β heat treat temperature were quite

21

similar, with the former slow cooled material performing slightly better. Again, the colony microstructure was desirable, although its scale had less effect. Retained β phase fraction decreased with cooling rate. The small monotonic increase in creep resistance with decreasing cooling rate, followed from the poor creep performance of β compared to α (or α_2).
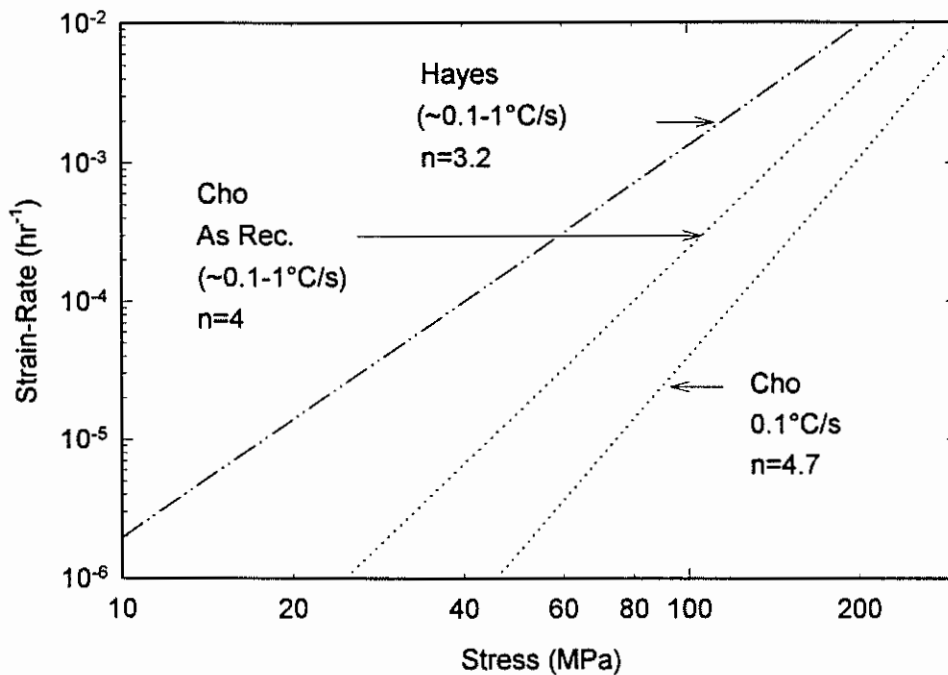
Figure 4
Stress dependence of strain-rate at 760°C for β solution treated Ti-25-10-3-1, based on Cho, *et.al.*[12] and Hayes.[37]

Hayes[37] investigated the creep behavior of Ti-25-10-3-1 in both $\alpha_2 + \beta$ rolled (0.508 mm) condition and after subsequent β solution treatment (1135°C/1 hr./furnace cool). Following from the previous discussion, the $\alpha_2 + \beta$ material exhibited a fine (6-10 μm) primary α_2 precipitates in an equal β phase fraction matrix. The β solution treated material consisted of Widmanstätten α_2 plates in a β (B2) matrix. Since the cooling rate

22

was not given, it was difficult to relate the β solution treated microstructure to the CCT diagram presented in Figure 2. Assuming furnace cooling occurred at a rate near $1°C·s^{-1}$, the observed structure follows from the CCT diagram. That Hayes[37] does not observe the O and ω phases until after creep deformation, suggests the higher cooling rate.

Again, the α_2 + β treated material exhibited an order of magnitude higher creep rate compared to β heat treated material. Hayes[37] states the β solution treated material behaved similarly to the like treated as-received material of Cho, et.al.[12] However, a comparison of the n values from Hayes[37] vs. Cho, et.al.[12] (respectively: 650°C: 4 vs. 4.6; 704°C: 3.7 vs. 4.7) shows considerable difference. The E_a values were similar at 330 and 305 kJ/mol, respectively.

Figure 3 illustrates the clear superiority of the heat treatments employed in the study of Cho, et.al.[12] * This superiority extends to, and is enhanced at 760°C as shown in Figure 4. However, even with these results, the choice of cooling rate is not intuitively obvious. Considering additional information, Cho, et.al.[12] also noted without explanation that both room temperature strength and elongation decrease monotonically with cooling rate. At 0.1°C/s, the elongation was only 1%, compared with 2% at 0.5°C/s. Increasing the cooling rate to 10°C/s gave only a marginal increase in ductility to 2.4%. Therefore, for the duplex heat treated material, the 0.5°C/s controlled cooling rate provided the best

---

* It should be noted that Hayes[37] tested sheet, whereas Cho, et.al.[12] tested bulk samples. The creep rate in the foil may be enhanced by the relative proportion of surface and the grain size relative to the sample thickness (grain size: 0.150 mm, sheet thickness 0.503 mm).

property compromise. This conclusion compared favorably with results for other Ti alloys, as shown by Mishra and Banerjee[36] and Blenkinsop, *et.al.*[5]

The remaining question is whether a duplex β solution treatment provides superior creep resistance compared to a single β solution treatment with identical cooling rate. Unfortunately, the only data available on the single β solution treated Ti-25-10-3-1 was for air cooled ($\sim 10°$C/s) material.[12] Compared to single air cooled material, duplex air cooled material shows superior creep resistance at 650°C and inferior performance at 760°C. As the fast cooling condition gave rise to generally poor creep resistance, compared to the duplex annealed material at the slower cooling rates, insufficient information is available to make a decision. However, considering that in both cases the solution treatment occurs above the β transus, it seems plausible that given identical hold times at the solution temperature, and cooling histories, the two heat treatments should provide similar results.

In general, β processing of Ti alloys leads to improved fracture toughness K_{IC}.[8,31] This may seem to be in conflict with the reduced ductility observed in β processed material. However, fracture toughness and dutility are not related, *c.f.*, Coyne.[8] The equiaxed $\alpha_2 + \beta$ processed microstructures contain insufficient barriers to crack propagation. The phase boundaries in transformed β act as barriers to crack propagation. Given a transgranular Widmanstätten, or a coarse colony microstructure where the colony size is on the order of the prior-β grain size, *i.e.* slow cooled material, the cracks once arrested at a phase boundary easily propagate along the boundary in a relatively

24

unimpeded straight line, thereby giving a low K_{IC}. With a fine basketweave microstructure, *i.e.,* resulting from fast cooling, however, the significant crack deflection occurs at each phase boundary, limiting crack length and boosting K_{IC}.[31]

The implication is to use high cooling rates from above the β transus to achieve the fine basketweave conducive to high K_{IC}. Returning to the microstructures generated by Cho, *et.al.*[12] as an example, either the as received β processed or the duplex β solution treated, 10°C/s cooled microstructures would be expected to provide the greatest K_{IC}. Unfortunately, microstructures favoring high K_{IC} favor low creep resistance.

Stucke and Lipsitt,[38] investigated the effects of cooling rate and solution temperature on Ti-27Al-5Nb. The starting material was rapidly solidified followed by canning and extrusion of bar at 1204°C, above the β transus of 1182°C. The samples were solution treated at 1204°C or 1121°C, followed by quenching in either water, air, or 760°C molten salt. Resulting microstructures were all α_2, presumably due to the low concentration of the Nb β stabilizer. The microstructures of the β solution treated material showed fine and coarse Lenticular α_2 structures resulting from air and salt bath quenching, respectively. The primary conclusion put forth by this paper was that neither the quench rate nor the phase field greatly affected fatigue crack growth in this alloy.

However, this conclusion probably is not valid for alloys with higher Nb levels, where β is present. It was pointed out that the α_2 + β interface can deflect cracks. Davidson, *et.al.*[39] studied fatigue crack growth in α_2 + β processed (1000°C/15 min/air cool) Ti-25-10-3-1 rolled plate. The material had slightly elongated primary α_2 grains in

a transformed β matrix. Fatigue cracks were observed to nucleate only in the α_2 grains. This is expected considering the number of active slip systems in β vs. α_2. They present evidence of crack deflection by retained-β grains.

From this evidence it would seem that optimal fatigue resistance would obtain in material with a fine colony or basketweave structure, where significant crack deflection could occur within the transformed β phase, thus minimizing crack length. This is the microstructure that results from high cooling rates from above the β transus, *i.e.,* the microstructure giving rise to the poorest creep performance. In their early work with Ti-25-10-3-1, Blackburn and Smith[4] observed that coarse grained material had markedly lower fatigue resistance compared to fine grained material. However, as with other properties, it is difficult to comment on the process vs. property issue due to their unorthodox TMP which did not include a proper ingot breakdown operation.

An additional factor must be considered when discussing the quintinary alloy--intergranular precipitates. Intergranular precipitation in sub-transus forged material has been observed to have a deleterious effect on the fatigue resistance of this material. The β forged material has been observed to have better fatigue resistance than $\alpha_2 + \beta$ forged material, even with the attendant coarsening.[32] Blenkensop, *et.al.*[5] also briefly allude to the intergranular precipitation problem in the context of slow cooled β processed material.

An alternate processing approach distinguished by forging through the β transus temperature has been suggested[32] to preclude the grain boundary precipitation problem and the severe coarsening characteristic of β processed material. The material is heated

to just above the β transus temperature and isothermally forged between dies slightly below the transus temperature. Following deformation, the material is cooled at a controlled rate in the forge to a stabilizing temperature within the operating range for the alloy, where it is subsequently held. The forging is then cooled rapidly to room temperature, whereby it is ready for application.

2.2 Experimental Thermo-Mechanical Processing History

The ingot material used in this research was purchased from Titanium Metals Corporation[*] (Timet) as billet. Isothermal forging and heat treatment was performed by Wyman-Gordon Company[†] per specifications developed by the author. The following sections give the processing details.

2.2.1 Ingot and Conversion to Billet

The super α_2 titanium aluminide Ti-25Al-10Nb-3V-1Mo was purchased from Timet as billet product from one ingot. The ingot was from heat G-4251. The chemical composition was determined by Timet at the top and bottom of the starting ingot as shown in Table 1. This information was provided in the material certification in terms of weight percent and is given in terms of atomic percent.

27

Table 1

Ingot Composition (Atomic %)

Location	Ti	Al	Nb	V	Mo	C	Fe
Top	bal.	24.2	11.2	2.98	0.97	0.073	0.062
Botom	bal.	24.8	10.6	3.06	1.12	0.068	0.055
Mean	bal.	24.5	10.9	3.02	1.04	0.070	0.058

The billet stock was provided as two, 185.4 mm diameter by 89.4 mm high sections, and one thinner section of 31.8 mm height. While Timet considered ingot processing proprietary,[40] the following information on the ingot breakdown schedule was provided:

1. 813 mm diameter ingot β forged to 559 mm round corner square (RCS).

2. RCS α_2 + β forged to 193.7 mm round.

3. Lathe turned to 184 mm round.

4. Band saw cut into 102 mm long mults.

5. Mults fused to 89.4 mm billets.

The as cast microstructure was broken down by working above the β transus, as is typical for most titanium ingot.[31,7] Less than 40% of the final billet processing was performed sub-transus. Blackburn and Smith reported the β transus to be in the range of 1065°C to 1095°C. In the same work, the importance of the ingot breakdown processing Ti-25-10-3-1 was retrospectively emphasized.[4]

2.2.2 Billet Conversion to Forging

Open die upset forging and β phase solution heat treatment was performed by Wyman-Gordon using their production isothermal forge under the cognizance of Dr. Mansoor Khan. Isothermal forging was to be performed per the following specification.

- Starting billet diameter: 185.4 mm

- Starting billet height: 89.4 mm

- Final pancake height: 29.7 mm $\pm$ 1.5 mm

- Upset ratio: 3:1

- Environment: Vacuum (2.7 Pa - 6.7 Pa)

- Billet & die temperature: 1045°C $\pm$ 10°C (β - 20°C)

- Strain-rate ($d\epsilon/dt$): 3.3×10^{-3} s^{-1}

Height control was provided by TZM (Mo-0.5Ti-0.1Zr) blocks placed around the billet. Press head position, instantaneous strain-rate and load were recorded as functions of time throughout the forging run.

Solution heat treatment was also done at Wyman-Gordon. Control of the cooling rate from solution heat treatment temperature was critical to achieving the desired microstructure. With only one billet of Ti-25-10-3-1 to process, it was necessary to perform cooling rate trials to develop a suitable cooling practice. A Ti-6-4 pancake of the same dimensions as the Ti-25-10-3-1 forging was instrumented with a thermocouple on the midplane of the forging, 50 mm from the outside diameter (O.D.) Also, a piece of 17 mm diameter Ti-25-10-3-1 was instrumented similarly. Based on controlled cooling

rate experiments using these samples, it was found by Wyman-Gordon that a cooling rate of *ca.* $0.65°C \cdot s^{-1}$ was achievable.[41] This is discussed in greater detail in the results and discussion section.

The actual Ti-25-10-3-1 billet was instrumented with a thermocouple on the midplane at a 50 mm depth from the O.D. This temperature was recorded during the cooling process. The specification for β solution heat treatment was as follows:

- Solution temperature: $1150°C \pm 5°C$
- Hold time: 1 hr
- Furnace environment: Air
- Cooling rate to 760°C: $0.5°C \pm 0.1°C \cdot s^{-1}$
- Cooling rate to 25°C: Fan cool
- Quench medium: Air

Following heat treatment, the forging was grit blasted and chemically etched to remove scale and α case to a maximum depth of 0.25 mm per side. The etchant employed was considered proprietary to Timet.

2.3   Results and Discussion

This section describes the results of thermo-mechanical treatment given the Ti-25-10-3-1 material, and the subsequent β heat treatment of the forging.
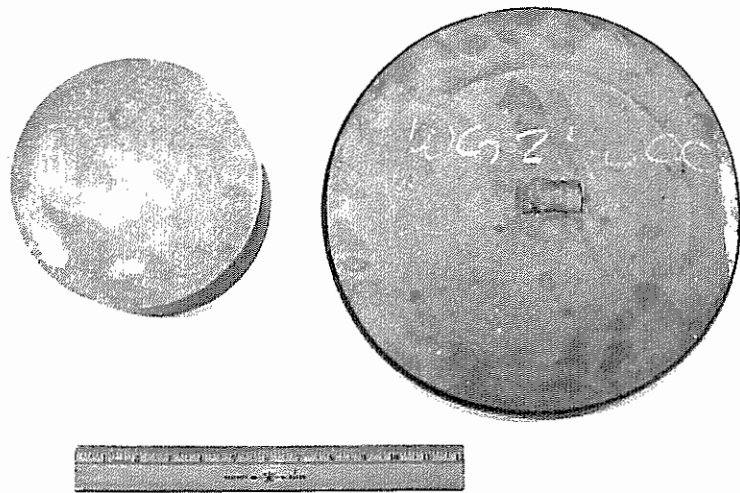
a
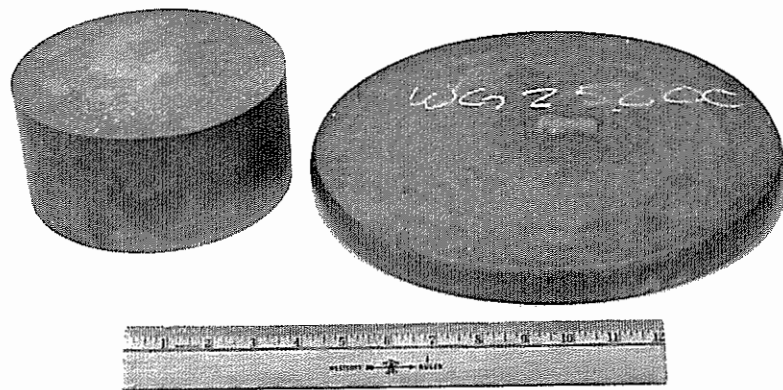
b

Figure 5
The billet as received from Timet vs. the pancake forging as
received from Wyman-Gordon. a. plan view showing material
initially in contact with the dies; b. view showing barreling of the
forging.

31

2.3.1   Thermo-Mechanical Processing of the Billet

The pancake forging was received from Wyman-Gordon as shown in Figure 5. This figure also shows the second unforged billet for comparison. The artifacts of barreling from the upset operation were evident in the two views. In the plan view of Figure 5a, a ring was observed, corresponding to the expanded O.D. of the billet. Material outside this ring was initially barreled and subsequently made reentrant die contact at some point during the forging process. Material within the ring slid along the die interface during forging. The diameter of the initial die contact area at the end of forging was 231 mm, compared to the initial 185 mm. Thus, substantial slip at the die interface occurred. This was in contrast to observations of Huang, *et.al.*[42] on Ti-25-10-3-1, deformed under nonisothermal hot die conditions, where only minimal slip and extensive dead zone was observed. The difference may be attributed to either improved lubrication at Wyman-Gordon, or to a possible deformation rate effect.

Barreling and reentrant die contact were the result of friction at the die/billet interface. The presence of reentrant die contact was evidence of stick/slip conditions at the die/billet interface. While Wyman-Gordon would not disclose the nature of the die lubricant, some bounds on its friction coefficient were determinable. Based on the concepts of the friction hill,[43,44] which is maximum at the center of die contact, the area subject to stick/slip vs. slip conditions was centered coincidently. This area increased in proportion to the extent of upsetting, *i.e.*, reduction in aspect ratio h/d, until the entire surface of the billet in contact with the die was experiencing stick/slip deformation. The

32

critical value of the friction coefficient μ_{ss} for transition from slip to stick/slip decreases with decreasing h/d. Based on Schroeder and Webster,[45] for the dimensions of the billet, μ_{ss} varied from 0.3 to 0.1 from the start to finish of the forging operation, respectively. Once the stick/slip mode was active over the entire surface of the forging, it was possible for the barreled material to make reentrant die contact as shown in Figure 5. That μ did not exceed the critical value of $\mu_c = 0.577$,[45] above which only slip deformation could occur at the die interface, was indicated by the lack of flow lines within the non-reentrant die contact zone as shown in the macrosections of the forging given in the metallography results section, Figure 13.

In general, negligible flow localization effects were observed, *i.e.*, the pancake forging was essentially circularly symmetric at all transverse (RC) cutting planes. The forging had a slight elliptical shape; however, the aspect ratio of 1.04 was very low. The initial die contact circle was eccentric about the O.D. of the forging by *ca.* 8 mm radially. The small extent of flow localization was expected from the low strain-rate[46] and the control of temperature homogeneity[47] afforded by isothermal forging.

During forging, both the forge load and press head position were separately recorded vs. time as shown in Figure 6a and 6b, respectively. Figure 6a for the initial *ca.* 100 s, shows the intrinsic press drag, *i.e.*, the force necessary to move the head, of *ca.* 741 kN (83 tons). In the calculations to follow, the press drag was assumed to remain constant. The robustness of the isothermal forge is evident in Figure 6b, where no
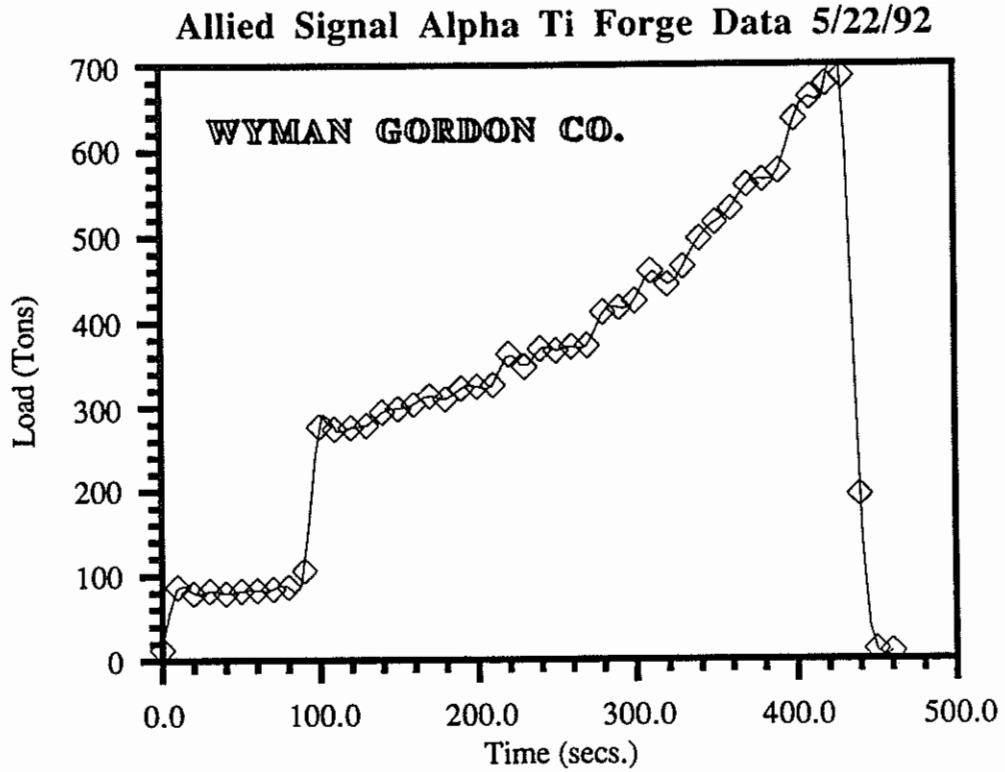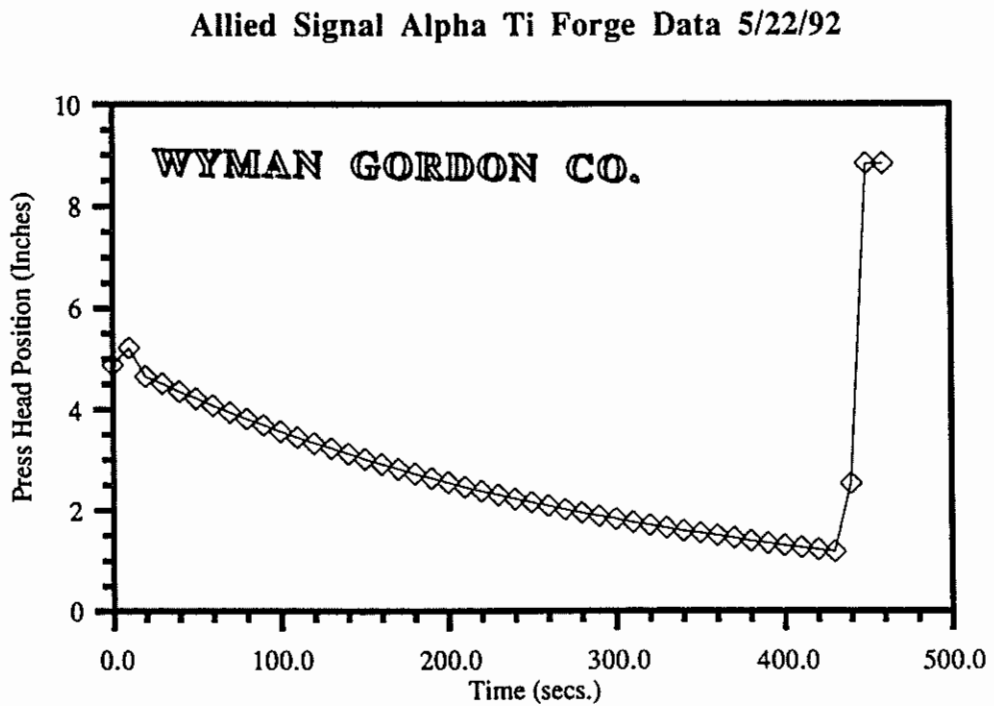
Figure 6

Isothermal forging documentation plots from Wyman-Gordon: a. load vs. time; b. press head displacement vs. time.

perturbation in the press head position vs. time was evident at incipient die contact. The measured press head displacment was affected by a zero error +1.143 mm, which at 1.3% of full stroke was impressive, given the scale of the equipment. The load in Figure 6a, while beginning to increase smoothly, after *ca.* 200 s, becomes more serrated. This could evidence the onset of stick/slip conditions.

A load vs. stroke curve was created from the digitization of Figures 6a and 6b, assuming a common time base. The load and displacement values were corrected for the press drag and position offset, respectively. This curve is shown in Figure 7. Note the monotonic load increase with deformation. This paralleled observations of Semiatin and Lahoti[48] in Ti-6242 with an equiaxed primary α in a transformed β microstructure similar
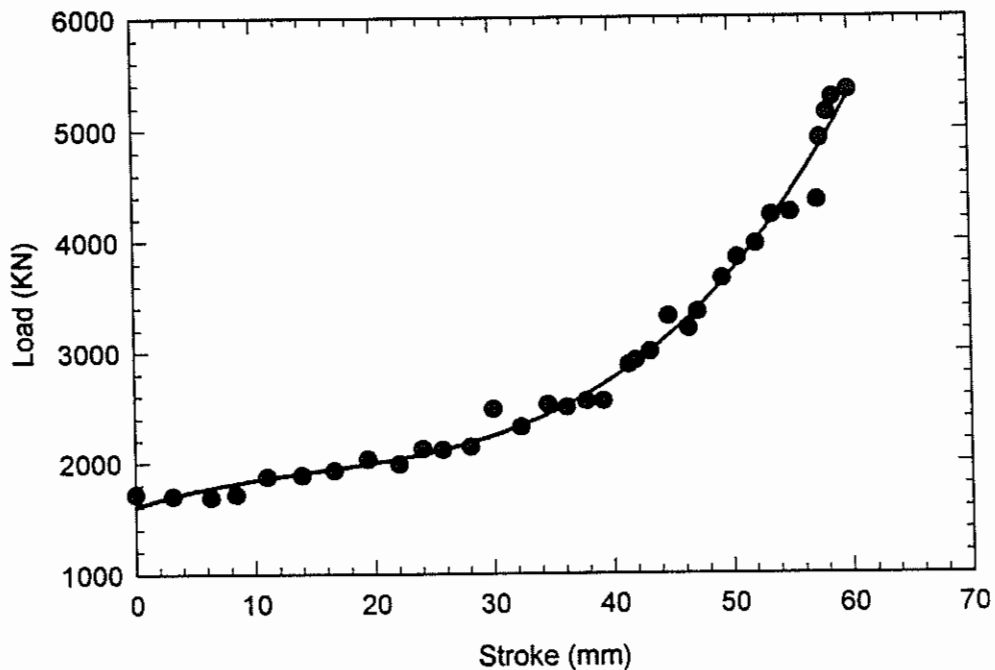
Figure 7
Forging load vs. press head stroke curve (3d order regression) for isothermal forging of Ti-25-10-3-1.

35

to the billet microstructure employed in this research. They also observed that Widmanstätten microstructures gave rise to decreasing load vs. stroke curves, and nonuniform deformation. It has been noted by Semiatin and Jonas,[46] that a maximum in the load vs. stroke curve is necessary for significant flow localization to obtain.

A true stress vs. true strain diagram was created from the load stroke curve of Figure 7, as shown in Figure 8. The analysis was based on the assumptions of volume conservation and lack of barreling.[49] Models have been put forward to account for friction at the die interface, *c.f.* Huang, *et.al.*,[42] however, not knowing the friction coefficient, these models were of little use. The true stress was

$$\sigma_T = F \frac{\ell_i}{\ell_o \pi r_o^2} \tag{2}$$

where F was the press load corrected for the press drag, r_o the initial radius of the billet and ℓ_i and ℓ_o were the instantaneous height and original height of the billet, respectively. The true strain was calculated from the usual definition

$$\epsilon_T = \ln \frac{\ell_i}{\ell_o} \tag{3}$$

The assumption of constant press head drag was not experimentally verified, and may lead to significant errors in the following analysis.

The calculated true stress vs. true strain diagram is presented in Figure 8. A second order polynomial curve fit emphasized the unorthodox concave up parabolic shape to the true stress vs. true strain curve. The scatter in the data relative to the 95% confidence band about the parabolic fit showed that a straight line fit was not appropriate. A curve of this shape would indicate initial flow softening followed by work hardening, an unprecedented behavior. Indeed, at the strain-rate and temperature employed in this research, essentially flat true stress vs. true strain curves were expected.[48] Chaudhury and Zhao[50] investigated the formability of Ti-25-10-3-1 at temperatures from 843°C to 1010°C and strain-rates from 0.1 to 8 s^{-1}. While their temperatures were lower and strain-

True Stress vs. True Strain
Rank 25 Eqn 1003 y=a+bx+cx^2
r^2=0.664181064 DF Adj r^2=0.63059917 FitStdErr=2.16553226 Fstat=30.6558248
a=61.678354 b=-22.188243
c=24.346938
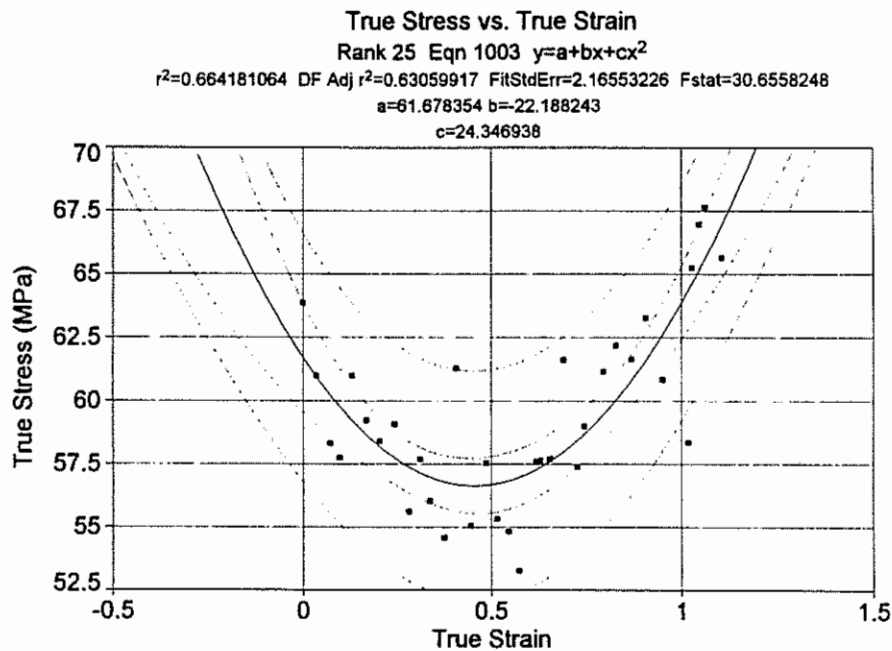
Figure 8
True stress vs. true strain diagram for isothermal forging of Ti-25-10-3-1, incorporating a 2nd. order polynomial fit and 95% confidence bands.

rates at least two orders of magnitude higher, the true stress vs. true strain was essentially flat at 1010°C and 0.1 s^{-1} strain-rate. Increasing strain-rate led to more flow softening than at low strain-rates. Decreasing temperature had a similar effect. Thus, the lower strain rate and higher temperature in the present work would not be expected to give the observed initial flow softening, but would favor the observed work hardening which occurred later in the process.

Thus, a possible explanation for the anomalous behavior observed in this research lies in the strain rate with time. It must be kept in mind that the assumption of constant press head drag may not be accurate. Wyman-Gordon recorded the strain-rate throughout the isothermal forging operation. Their plot of strain-rate vs. time is presented in Figure 9. The time base was identical to that of Figures 7 and 6. Again, note that the deformation of the billet did not start until *ca.* 100 s. Wyman-Gordon reported an average strain-rate of 0.195 min^{-1}, or 3.25 x 10^{-3} s^{-1}. This was within the implicit tolerance on the specified 3.3 x 10^{-3} s^{-1} strain-rate.

The instantaneous strain-rate varied throughout the deformation process as shown in Figure 9. This variation in strain-rate can be used to explain the anomalous true stress vs. true strain curve of Figure 8. Assuming[48,51,54] that flow stress was not strain sensitive during isothermal forging, the empirical correlation

$$\sigma_T = K' \left(\frac{d\varepsilon}{dt} \right)_T^m \tag{4}$$

38

describes the true stress σ as a function of $d\epsilon/dt$ and the adjustable parameters m and K', corresponding to the strain-rate sensitivity and proportionality constant, respectively. Figure 10 shows the σ_T plotted vs. $d\epsilon/dt$. Attempting to fit Equation 4 to these data was not prudent given the scatter in the data. Considering the industrial scale of the forge and the instrumentation, this was not unexpected. Values of $m = 0.2$ and $K' = 192$ (correlation coefficient $r = 0.8$) approximate the strain-rate sensitivity in the increasing $(d\epsilon/dt)_T$ region of Figure 9 between 250 s and 309 s. This is a reasonable value of m. However, note that it does not explain all of the data points in Figure 8. Thus, the minimum in the true stress

Allied Signal Alpha Ti Forge Data 5/22/92
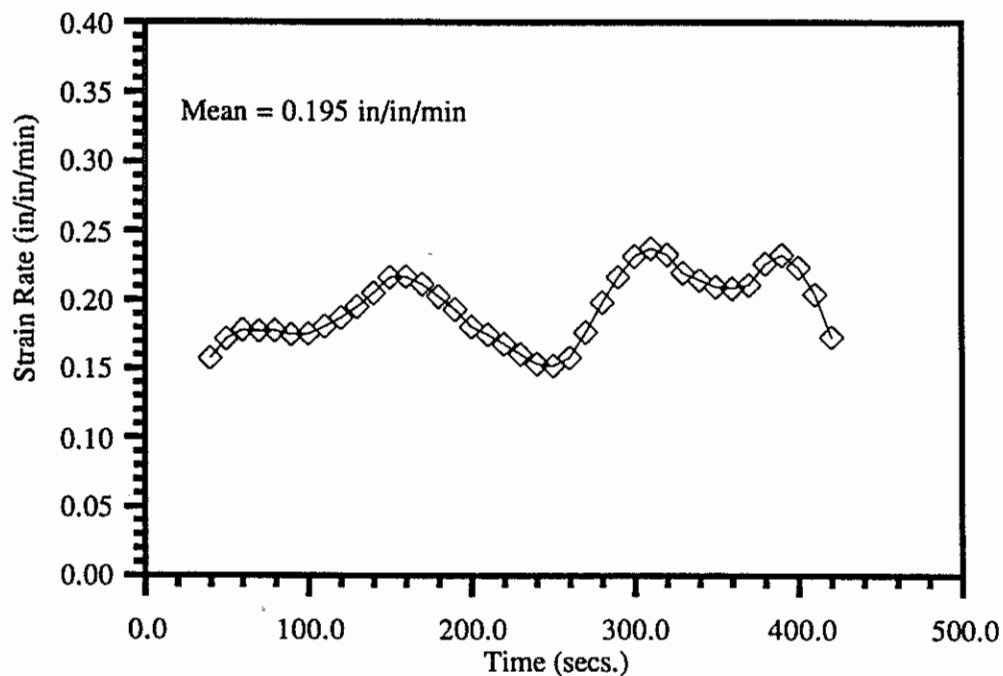
WYMAN GORDON CO.

Figure 9
Instantaneous strain-rate vs. time for isothermal forging of Ti-25-10-3-1 as
provided by Wyman-Gordon.

39

vs. true strain plot of Figure 8 might be explained by strain-rate sensitivity. However, this explanation does not adequately deal with the initial increase of strain rate shown in Figure 9, and the corresponding decrease in true stress with strain shown in Figure 8.
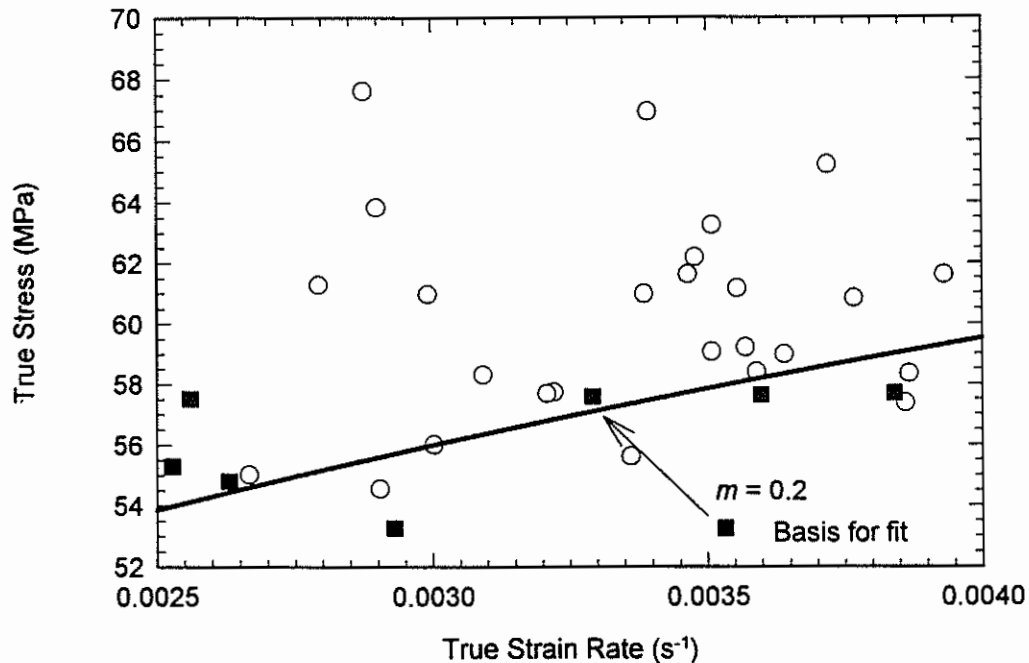
Figure 10
Strain-rate sensitivity for isothermal forging of Ti-25-10-3-1.

Davies, *et.al.*[52] reviewed the phenomenological and metallographic background to structural superplastic deformation. Materials deform as viscous solids when $m = 1$, and by slip/diffusional creep when $m = 0.1$. The first of the three criteria for structural superplasticity is that $m > 0.3$. The microstructure must also be equiaxed with a grain size less than 10 μm. In two phase solids, the grain sizes of the phases must be similar. The third requirement is similar diffusion rates in the two phases. During structural superplastic deformation, recrystallization or slip do not occur, but rather the deformation

is by grain boundary sliding. The grain boundary sliding can reduce crystallographic texture, as is discussed in detail in the Texture chapter.

It was not possible to directly assess compliance with these three criteria in this research. The observed strain-rate sensitivity was *ca.* 0.2. However, this measurement was quite crude as already noted. Based on work of Millett *et.al.*[54] on Ti-25-10-3-1, this value should be greater than 0.3 for the conditions employed in this research. The grain size of the primary α_2 was *ca.* 7 μm, as shown in Figure 16. It was not possible to measure the secondary α_2 grain size at the forging temperature. Again based on the research of Millett *et.al.*[54] the primary α_2 grain size should change appreciably at the forging temperature, and likewise the secondary α_2 should have been well under the requisite 10 μm grain size. The diffusion coefficient criterion is much harder to elaborate on, as accurate diffusion data is not available for the α_2 phase.

Yang, *et.al.*[51] investigated the superplastic behavior of Ti-25-10-3-1 over the sub β transus temperature range of 950° to 1010°C and strain-rates from 2×10^{-5} to 1×10^{-2} s⁻¹. The strain-rate sensitivity was little affected by temperature in the range tested. At 1010°C a strain-rate sensitivity of $m = 0.36$ was observed. This is not too far from the value of 0.2 crudely determined in the present investigation. Dutta and Banerjee[53] investigated the superplastic behavior of Ti-24-11 at temperatures from 950°C to 1020°C and strain-rates from 6×10^{-7} to 1×10^{-2}. The optimum conditions for superplastic deformation, *i.e.*, maximum *m,* were at 980°C and 1×10^{-4} s⁻¹; at a strain-rate an order of magnitude lower than in the research reported here. They observed the maximum in the

41

value of m as a function of strain-rate was found to shift to higher strain-rates with increasing temperature. At 1020°C, the maximum value of $m = 5.5$ occurred at a strain-rate of *ca.* 1×10^{-3} s^{-1}. Following this trend, at 1045°C, and the strain-rate employed in this research, a lower value of m would have been expected, as was observed in this research.

Greenwood, *et.al.*[14] in an investigation of the forging of Ti-6-4, discuss the transition from superplastic to isothermal forging conditions. The resulting super-plastically deformed microstructure is equiaxed. Isothermal forging is performed at strain-rates just in excess of the superplastic region of the true stress true strain-rate space. Slight elongation of the microstructure is an indication of the transition from superplastic to isothermal deformation modes. Referring to the metallography chapter, no significant elongation of the microstructure was observed in the present study. Thus, while the crude estimate of m given in this section places it outside the superplastic region, the equiaxed nature of the resulting microstructure, and other references from the literature support the assertion that the deformation in the Ti-25-10-3-1 was on the borderline of the superplastic/isothermal regions.

This transitional behavior between pure superplastic and conventional plastic deformation has been reported in the intermetallic Ti-25-10-3-1 in lab scale investigations. Millet, *et.al.*[54] investigated the isothermal forging of Ti-25-10-3-1, following development of the thermo-mechanical processing plan for this research. They investigated the forgability between 900°C and 1050°C at strain-rates from 3×10^{-4} s^{-1}

to 3.5 x 10^{-2} s^{-1} using 15 mm dia. x 26 mm cylindrical specimens taken from Timet supplied material very similar to that used in this research. The strain-rate sensitivity was $m = 0.268$, which compares quite favorably with the value estimated in this research. An activation energy for deformation was determned to be 436.5 kJ $\cdot$ mol^{-1}. This was between the activation energy of 308 kJ $\cdot$ mol^{-1} for superplastic deformation[51] and their estimate of 606 kJ $\cdot$ mol^{-1} for the activation energy for α_2 dissolution in the β phase. It should be noted, however, that activation energies are not considered highly accurate pointers to superplastic deformation. Based on the monotonically decreasing extent of strain softening with increasing temperature, they also concluded that dynamic recrystallization was a component of the deformation process in this material. On these grounds, they proposed that the Ti-25-10-3-1 deformed by a combination of superplastic and conventional dynamic recrystallization processes.

Based on experimental measurements of strain-rate sensitivity and grain size, and on the evidence from lab scale experiments from the literature, it is highly likely that the deformation of the Ti-25-10-3-1 in this industrial scale research included a superplastic component. This suggestion is further strengthened considering the texture development as discussed in succeeding sections.

2.3.2 β Heat Treatment of the Forging

Prior to heat treating the forging, Wyman-Gordon recommended an experimental evaluation of cooling rate control capability. Wyman-Gordon performed an evaluation of cooling rate control using an equivalently sized pancake of Ti-6-4. The cooling curve

43

is shown in Figure 11a. Note the initially high cooling rate during the 2 min. after removal from the heat treat furnace. This was the time necessary to place insulation over the top of the forging. The cooling rate then approached the goal of $0.5°C·s^{-1}$. The perturbations in the cooling rate at 13:54:20 and 13:56:30 were the result of manual readjustment of the insulator. A follow-on trial was performed using a small plate of Ti-25-10-3-1. The cooling curve is shown in Figure 11b. Again, note the higher cooling rate at the start.

The cooling curve for the forging is presented in Figure 12. The qualitative similarity to the small plate of figure 11b was evident. The heat treatment specification called for a cooling rate of $0.5°C\ s^{-1} \pm 0.05°C\ s^{-1}$ to 760°C. The actual cooling rate to 760°C was $0.55\ °C\ s^{-1}$ as determined by least squares regression of the digitized cooling curve. However, over the first 100 s of the cooling process, the cooling rate was *ca.* $0.8°C\ s^{-1}$. This higher cooling rate may explain the finer than expected microstructure. Briefly, a colony microstructure was expected based on the work of Cho, *et.al.*[12]
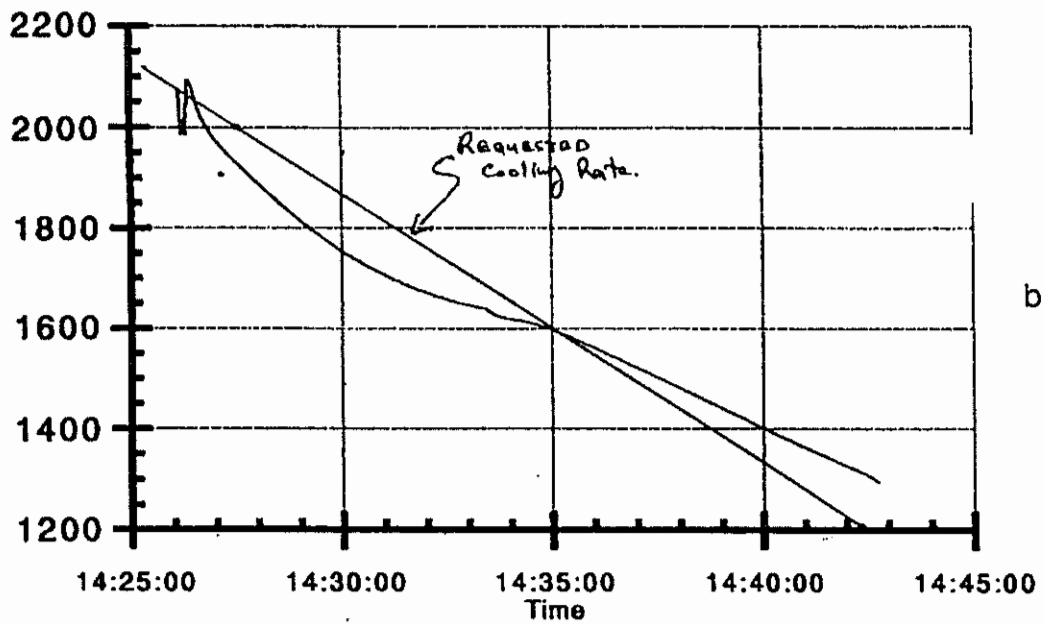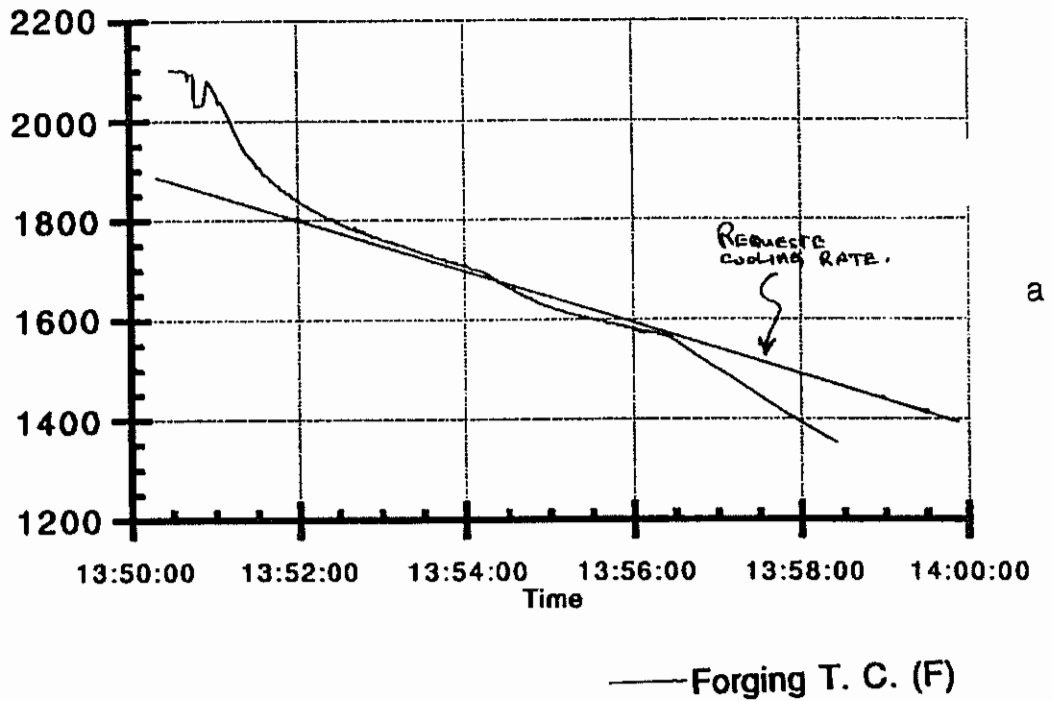
Figure 11
Cooling curves from Wyman-Gordon cooling trials: a. cooling curve for
Ti-6Al-4V of identical size to the forging; b. cooling curve for a small
sample of Ti-25-10-3-1.

45

Allied Signal Alpha 2 Ti Forging Heat Treat 5-28-92

Slope of Linear Fit = 57.4 °F/min.
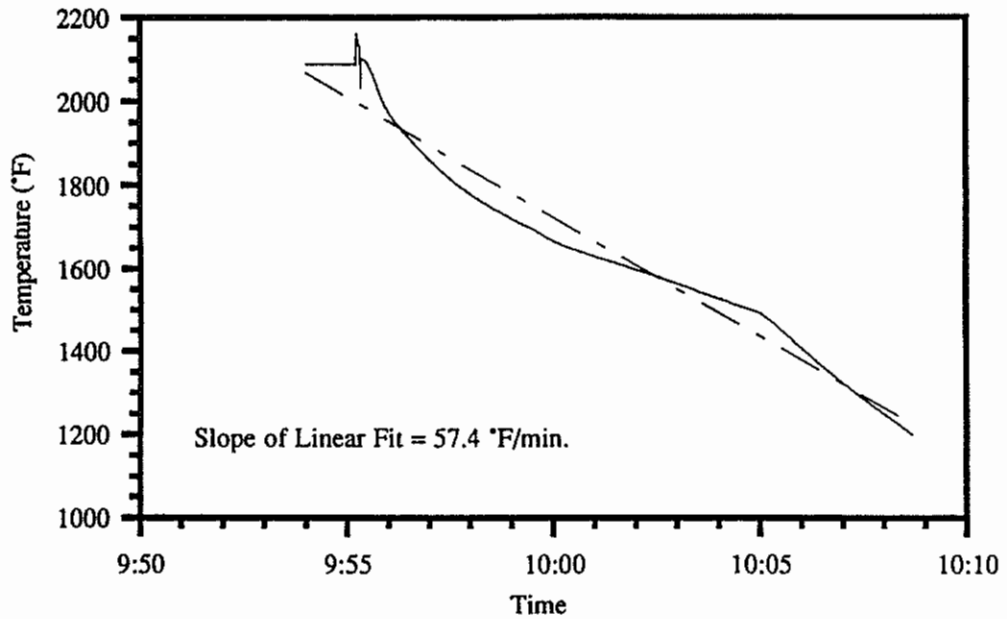
WYMAN GORDON CO.

Figure 12
Cooling curve for the Ti-25-10-3-1 forging based on thermocouple readings
at 50 mm from the forging O.D. on the T/2 plane (midplane).

CHAPTER 3

OPTICAL METALLOGRAPHY

This section presents the background, experimental methods, and results of metallographic investigations of the billet and forging. The primary objective of the optical metallographic investigation was to document the results of the thermo-mechanical processing operations. A secondary objective was to assess the use of quantitative metallographic techniques for measurement of crystallographic texture.

3.1 Background

The binary Ti-Al phase equilibrium diagram has been assessed by Murray[7] as shown in Figure 1. Although several more recent investigations of McCullough, *et.al.*[55] and Perpezko and Mishurda[56] have revealed contradictions with the assessed diagram, the fields of contention are at Al concentrations hyperstoichiometric to Ti_3Al and thus do not affect this project. Mishurda and Perpezko[56] note that from pure Ti to Ti_3Al, the assessed diagram should be taken as correct. Lipsit,[57] while also addressing the higher Al concentration phases, shows a wider $\alpha_2 + \delta$ region at both high and low Al boundaries. The α or titanium phase has the A3 hcp structure. The pure Ti_3Al α_2 phase forms congruently from the α at 1180°C. The ordered α_2 phase has the DO_{19} structure. With

47

the addition of Al, the transus temperature is found to increase from 882°C for pure Ti to 1285°C at the peritectoid point (β + TiAl ⇌ α). Above the β transus temperature, the metal has the A2 bcc structure.[3]

The commonly known phases in the quintinary alloy are α_2 (ordered hcp, DO_{19}), β (disordered bcc), B2 (ordered bcc β),[58] ω (hcp, $B8_2$)[58] and O (orthorhombic).[59] Kestner-Weykamp, *et.al.*[60] note reports of two other unidentified phases in the alloy. However, no complete analysis of equilibrium constitution in the quintinary alloy is available in the literature. Of these phases, only the α_2 and β phases are easily identifiable by optical metallography. The α titanium phase is etched less than the β phase, hence appearing as the light structure in the micrographs.[73] The β phase is the corresponding dark structure in the photomicrographs. Throughout this research, further differentiation of phases beyond α_2 and β is only presented when necessary, and for experimental data, when conclusively identified. This approximate method of identifying phases based on the binary phase diagram makes important correlations with the behavior of non-intermetallic and simpler Ti alloys more evident, and is consistent with common practice in the literature.

The metallographic structure of α_2 titanium aluminides is described following the nomenclature of a proposed AMS-SAE standard.[25,34] While this nomenclature was developed to describe α + β alloys, the substitution of the ordered α_2 phase for the α phase does not deter from proper application of the standard. It should be noted that many references given in this thesis do not follow this nomenclature.

An $\alpha + \beta$ titanium alloy processed within the $\alpha + \beta$ phase field consists of equiaxed primary α within a matrix of Widmanstätten transformed β. Large prior β grain boundaries are typically evident. In β processed material, *i.e.*, processed above the β transus, the primary α is not present. On cooling through the transus, α_2 precipitates. Within the prior β grains, is the Widmanstätten α phase. The Widmanstätten α phase forms by nucleation and growth process, just as Aaronson[61] observed in steel and cursorily in Ti-Cr. The α phase can also form from an intermediary martensitic structure.[66] From a metallographic viewpoint, the typical sequence of events in transformed β microstructures with increasing cooling rate is:

- Formation of transgranular Widmanstätten α plates, possibly separated by retained β

- Development of a coarse colony microstructure

- Interleaving of colonies to form a basket wheave structure.

- Refinement of the α plate size

- Formation of α-martensite in some alloys.

The transformation product from both diffusional and martensitic reaction in $\alpha + \beta$[62,63] and $\alpha_2 + \beta$[64] alloys generally follows the Burgers[65] orientation relationship: $(0001)_{\alpha 2} \parallel (011)_{\beta}$; $<11\bar{2}0>_{\alpha 2} \parallel <111>_{\beta}$. Weykamp, *et.al.*[66] specifically observed this orientation relationship in Ti-24-11. However, in Ti alloys, it has been observed that the basal plane can be inclined by *ca.* 0.5° to the $\{110\}_{\beta}$.[67]

In this thesis, the morphology of the α_2 transformation product is described in terms of the Dubé morphological classification system as described by Aaronson.[61] The applicability of this classification system to titanium alloys has recently been shown by Béchet, *et.al.*[68] (although not explicitly) in the β-CEZ alloy (a near β alloy).

Following this scheme, grain boundary α_2 (allotriomorphs) typically decorate the prior β grain boundaries. In $\alpha + \beta$ alloy Ti-6-4, Chesnutt, *et.al.*[69] observed an almost continuous α phase at the prior β grain boundaries following β forging and β solution treatment. Rhodes and Williams[70] noted that the interphase, *i.e.*, prior βgrain boundary phase, structure is common to most titanium alloys. They said that this structure is more complex than α or α_2. In work of Porter, *et.al.,*[71] on the metastable β alloy Ti-15V-3Cr-3Al-3Sn, the grain boundary phase thickness was inversely proportional to the tensile elongation. Porter, *et.al.*[71] noted that the grain boundary phase forms with greater thickness following slower cooling operations. This was in keeping with the nucleation and growth notion.

In work of Allison *et.al.*[72] on Ti-6Al-2Sn-4Zr-2Mo* prior β grain sizes were observed to be 250 μm following $\alpha + \beta$ rolling, β solution treatment and controlled cooling at 0.5°C/sec. In work on IMI685 (Ti-6Al-5Zr-0.5Mo-0.25Si)[73]† Guo and Baker[74]

---

*   Highly creep resistant near-α alloy and competitor in this regard to the intermetallic alloys.

†   This is a creep resistant near-α alloy intended for service to 520°C in gas turbine applications.

and Blenkinsop, *et.al.*,[5] report that prior β grain sizes of 0.5 to 2 mm are typical. The normal grain growth rate of the β phase was observed to be 3 times that of the α phase by Guo and Baker.[73] They noted that, while recrystallization did occur in the IMI685, it was limited in the high temperature α+β and β processed material, particularly in material undergoing a β heat treatment. This was attributed to the high diffusivity of Ti in the β phase field.

3.2   Experimental Procedure

Samples for macroscopic optical metallographic examination were traveling wire electrical discharge machined (EDM) from both the billet and forging by AlliedSignal Controls & Accessories (ASCA). The round billet was sectioned into a sample 29 mm x 95 mm x 24 mm in the Longitudinal (L), Radial (R), and Circumferential (C) principal directions, respectively. This sample thus extended from the center of the billet to the outside diameter. The faces were surface ground to remove 0.51 mm per side for elimination of the EDM recast layer. The analysis surfaces were subsequently wet ground on 250 grit SiC paper. The forging samples were prepared similarly. The specimen dimensions were 24.3 mm x 158 mm x 10 mm in the L, R and C orientations, respectively, extending form the center to the outside diameter of the forging. The faces of the sample in contact with the forging dies were skim-cut to remove *ca.* 1 mm.

The specimens were etched in the as surface ground condition using Keller's etch of nominal composition (1% HF, 1.5% HCl, 2.5%HNO$_3$, 95% H$_2$O, vol.)[76] This etchant was employed primarily to reveal flow lines and secondarily to reveal prior β grain

boundaries in the forging and retained α_2 in the billet. Etching was done at room temperature using a swabbing technique. Photomacrographs were prepared using a Polaroid MP-4 copy stand.

Specimens for microscopic investigation were prepared from blanks traveling wire EDM'ed from the billet and forging at ASCA. The samples were cut from the blanks using a Leco Varicut VC 50 wafering saw with a 102 mm x 0.3 mm blade (Leco 810-137). In the billet, analysis planes were aligned with the 3 principal planes. In the forging, the analysis planes were aligned with the 3 principal planes at the half thickness along L (T/2) and at the surface (T).

The samples were subsequently mounted in Bakelite. Grinding and polishing operations were performed by hand. The wet grinding sequence consisted of 320, 400 and 600 grit SiC abrasive paper. Initial polishing was performed using 6 μm diamond lapping compound on a nylon cloth. The samples were washed with Ivory soap between polishing operations and rinsed in deionized water. Subsequent polishing was performed using 1 μm deaglomerated α-Al_2O_3 on a flocked twill cloth. Final polishing was performed using 0.3 μm and 0.005 μm Al_2O_3 on flocked twill cloth.* The samples were etched using Kroll's reagent[75] of nominal composition 1.9% HF, 3.8% HNO_3, 94.3% H_2O,[76] for approximately 10 s by swabbing.

---

* The 1 μm Al_2O_3 was chosen as a softer alternative to 1 μm diamond, which gave rise to comet tailing. This phenomenon is common in alloys with both soft (here, β), and hard (here, α_2) phases. Note that even the Al_2O_3 caused comet tails if polishing were continued past the point where scratches from the previous operation were removed.

Optical metallographic investigations were performed using the Aus Jena Neophot II metallograph with Normarski differential image contrast optics. Micrographs were prepared using both Polaroid type 55 positive/negative film and a Sony thermal print system.

Grain size measurements on the macrosections were performed using the Heyn intercept method per ASTM E112. The micrographs were placed on a Summagraphics SummaSketch II digitizing tablet on which an 80 or 100 mm line was overlaid. Six arbitrarily selected parallel regions of the micrographs were scanned for each grain size measurement. The grain intercepts were counted using the Jandel SigmaScan program. Measurements were performed parallel to the edges of the micrographs, i.e., in the principal directions, and at $\pm 45°$ orientations, to identify anisotropy. Macro prior β grain sizes G were calculated using:

$$G = 10 - 6.6439 \log\left(\frac{1}{N_L}\right) \tag{5}$$

where N_L was the number of intercepts per mm of test line. Nominal diameters of average grain sections were approximated per Vander Voort[75] using:

$$d_n \approx \frac{1.125}{N_L} \tag{6}$$

53

The analysis was extended to consider grain anisotropy when the grain size measurements for the four orientations of the test lines were outside the typical precision per ASTM E112 (± 0.5 in units of G). Intercepts were counted on the three principal directions, thus requiring two micrographs of orthogonal planes. Following ASTM E112, the average number of intercepts per unit length was:

$$\bar{N}_L = \tfrac{1}{3}\left(N_{L,R} + N_{L,L} + N_{L,C}\right) \tag{7}$$

where the final subscripts indicate the principal planes. Substitution into equation 3 gives the average grain size.

The percent anisotropy was calculated using the method put forward by Saltykov, as described by Underwood.[77] For a system of partially orientated lines (grains in this context), a group of test lines was first placed parallel to the observed orientation axis, *i.e.*, the axis showing grain elongation. The number of intercepts per unit length $N_{L,1}$ was then a measure of the nonoriented or isometric length of the grains. The isometric component of the grain length per unit area was then

$$L_{A,Iso} = \tfrac{\pi}{2}\, N_{L,1} \tag{8}$$

where the coefficient $\pi/2$ derives from the random nature, *i.e.*, the isometric component of the grain shape. Intercepts counted along a set of test lines constructed orthogonally to the first set then gave a measure of the combined isometric and oriented length of the grains. The oriented component of the grain length per unit area was

$$L_{A,V} = N_{L,\perp} - N_{L,\parallel} \tag{9}$$

where $N_{L,\perp}$ was the intercept count normal to the orientation axis. The anisotropic fraction was then

$$\Omega = \frac{N_{L,\perp} - N_{L,\parallel}}{N_{L,\perp} + 0.571 N_{L,\parallel}} \tag{10}$$

where the denominator was the sum of equations 8 and 9. This latter term corresponded to the total grain length per unit area for oriented and isometric components of the grain shape. In this development, it has been assumed that intercept count equals intersection count.[75]

The number of grains per square mm was determined using:[75]

$$N_A = 0.8\left(N_{L,\perp} N_{L,\parallel}\right) \tag{11}$$

Electronic image analysis was performed on selected photomicrographs of orthogonal planes from the forging sample, to identify the Widmanstätten plate orientation. The analysis was performed at AlliedSignal Research & Technology, Des Plains, IL, using the Universal Imaging Corporation IMAGE-1 system version 4. Linear dimension calibration of the Neophot II metallograph was performed using a stage micrometer obtained from ASCA. This calibration revealed a negative 1.5% of point error in magnification at 500X. The analyzed micrographs generally imaged a triple

point. Each of the three grains was scanned individually and in union. Besides other stereological data, the chord-angle of each counted Widmanstätten plate was tabulated by the system. The histogram analysis was performed using 2.5 degree buckets with the Jandel Scientific SigmaPlot program. Polar orientation roses were plotted from the histogram data using the method described by Underwood.[77]

3.3   Results and Discussion

The microstructures observed in the billet and forging differ markedly, owing to the differences in thermo-mechanical processing. This section describes the results and presents an interpretation of the microstructrues in light of prior ingot and billet processing, which led to the forging.

3.3.1   Billet Macrostructure

The billet was analyzed after the final stage of ingot breakdown, *i.e.,* in the round section form forged from the RCS. The results of optical metallographic inspection of the billet followed directly from the ingot breakdown operation outlined by Wardlaw.[40] Photomacrographs of the LR face revealed flow in the L direction. This is illustrated in Figure 13. The flow lines were in keeping with the reduction from RCS to round cross section, where a general elongation in the L direction was necessary to conserve volume. Flow lines were not evident in the other sections parallel to the principal planes.

10 mm
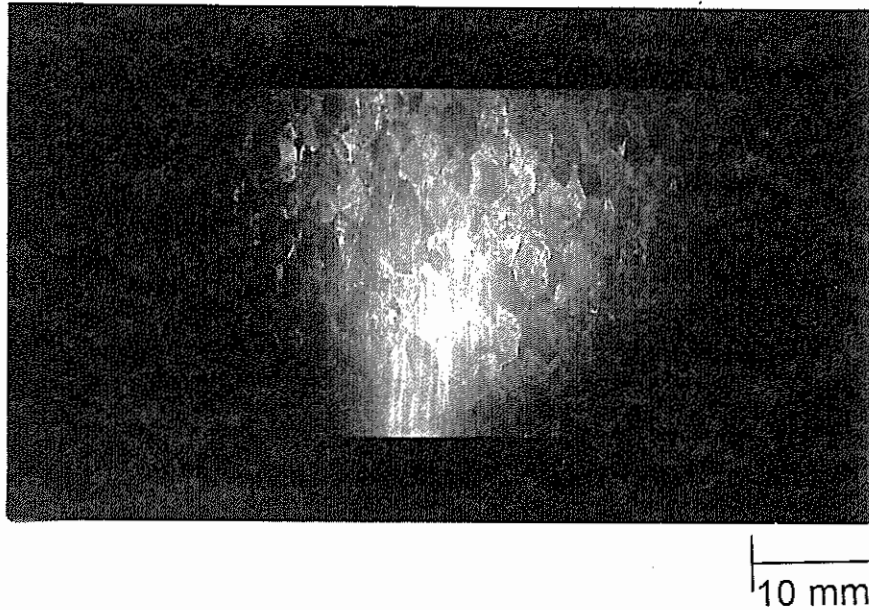
Figure 13
Photomacrograph of the billet LR face showing flow lines in the L
orientation. Keller's etch.

A prior β grain size gradient was revealed by the LR macrosection presented in

Figure 14 and in the CR plane. Finer grains were observed at the periphery of the round

billet section. This can be explained by the higher cooling rates experienced near the free

surface of the billet, strain inhomogeneity or a combination of the two effects. However,

not knowing the details of the forging process, this could not be confirmed. It was not

possible to accurately measure the prior β grain size in the fine peripheral region due to

the size of the region, and the poor resolution of grain boundaries.

15 mm
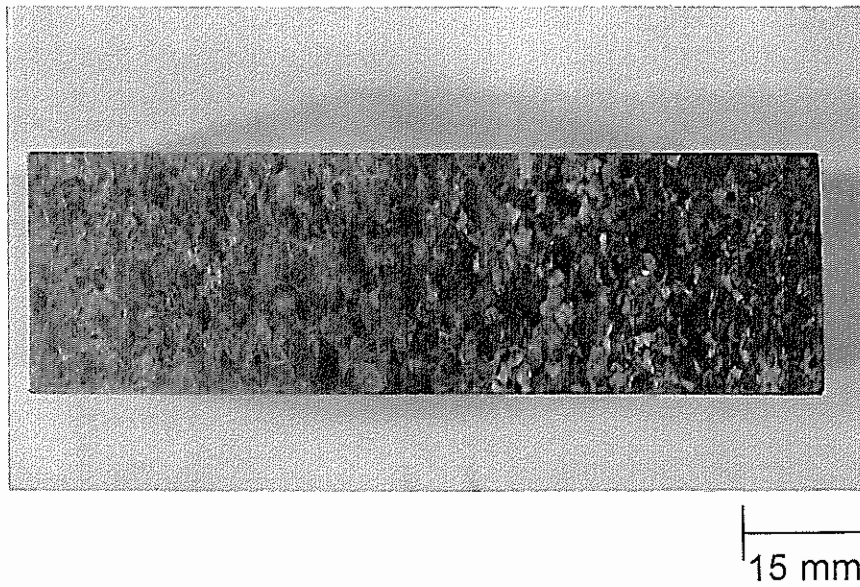
Figure 14
Photomacrograph of the billet LR face showing a grain size
gradient. The macro section was excised with the center at the
.   right and the O.D. at the left. Keller's etch.

Prior β grain sizes were measured about the 1/4 radius location for both the LR

and CR planes using the macrographs of Figure 15. Significant prior β grain shape

anisotropy was noted in the rose of intercept counts for the LR plane, with the orientation

axis along the L principal direction. As with the flow lines (Figure 13) reduction from an

RCS to round cross section with the attendant elongation in the L direction explains this

observation. The mean prior β grain size was determined using Equations 7 and 5 to be

ASTM M8.5, corresponding to a mean nominal diameter of 1.9 mm from Equation 6. Per

Equation 10 the prior β grains displayed values of Ω equal to 38% and 35% anisotropic

elongation along the L principal direction in the LR and LC principal planes, respectively

58

a

5 mm

b

5 mm
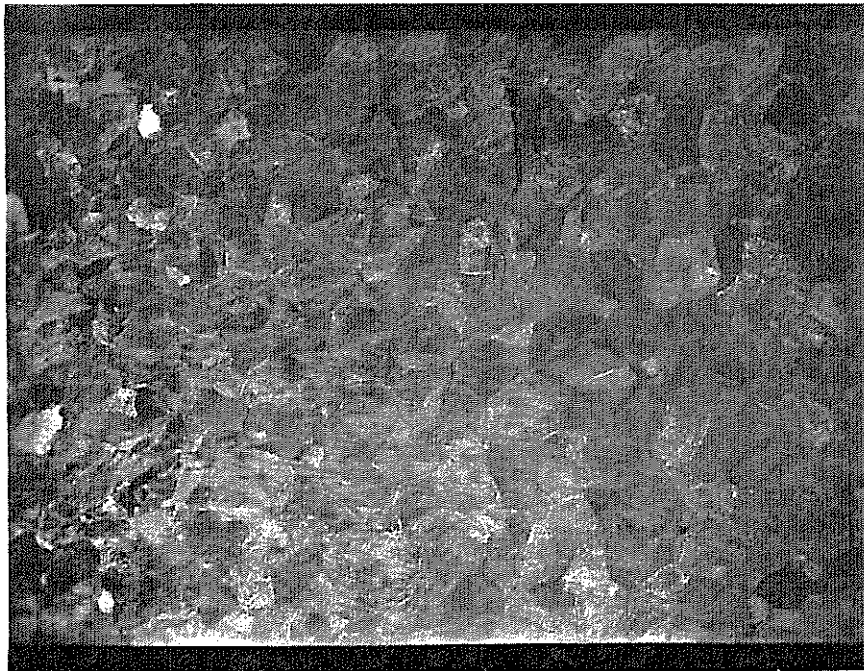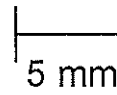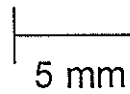
Figure 15

Photomacrograph of the billet about the ½ radius of the a. LR and
b. CR plane. Keller's etch.

In contrast, the prior β grains were essentially equiaxed in the CR principal plane (Ω = 4% along C), with grain sizes of ASTM M9 (1.6 mm mean nominal diameter).

3.3.2   Billet Microstructure

At the O.D. of the billet (Figure 16a) and at the center (Figure 16b), the microstructure consisted of primary α_2 (light, equiaxed phase) completely within a transformed β matrix of Widmanstätten α_2. These structures were isotropic. Again, Timet considered the quantitative aspects of the ingot breakdown process proprietary, hence, only speculations based on the observed structures are possible.

Qualitatively, the Widmanstätten plate size was smaller at the 185.4 mm O.D. of the billet (Figure 16a); evidence of faster cooling (*c.f.,* Cho, *et.al.*[12]) Cooling was most likely performed in air, based on the qualitative similarity of the Widmanstätten plate size to that observed in the pancake forging. Industrial economy also favors air cooling. The spheroidal shape of the primary α_2 at the O.D. (Figure 16a) compared to the polygonal shape at the center (Figure 16b) followed from the final forging operation performed during ingot breakdown. During the reduction form a 559 mm dia. RCS to 194 mm round cross section, the material nearer to the O.D. received greater work than that at the center. The occurrance of a dead metal zone at the center is typical of the reduction from RCS to round cross section, and has been observed by the author in other metals such as UNS C54400 bronze. The greater work nearer to the O.D. would enhance the recrystalization rate, thus leading to the spheroidal primary α_2. In the extreme case, an isolated prior β grain showed rectangular α_2 at the center of the billet as shown in Figure 16c.
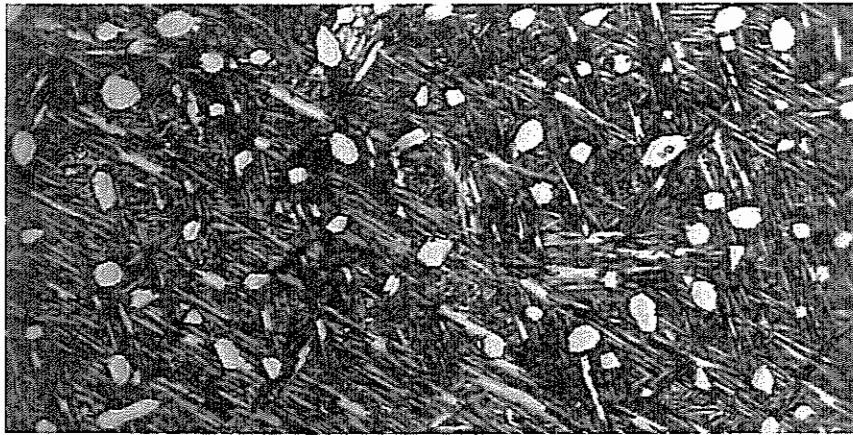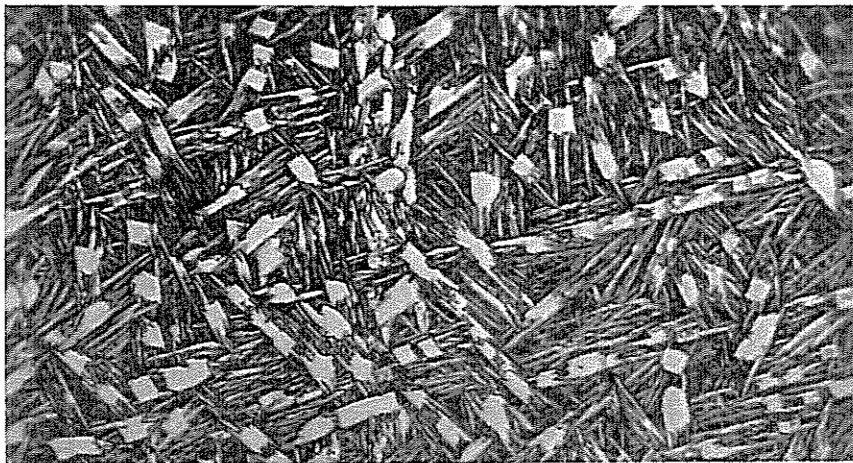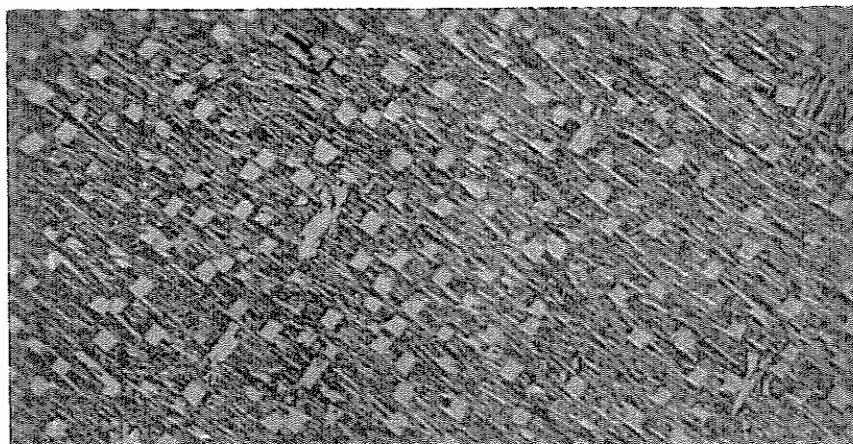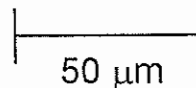
Figure 16
Billet microstructure a. LR plane at the O.D., b. LR plane at the center, c. extreme prior α_2 shape on LC plane at the center. Kroll's etch.

Prior β grain boundaries were harder to resolve in the billet than in the forging. The presence of grain boundary α_2 decoration revealed the prior β boundaries as shown in Figure 17. Here, the grain boundary phase appears continuous. However, in contrast to the forging, on higher magnification, the phase was revealed to be discontinuous. Grain boundary precipitation is discussed more fully in the context of the forging microstructure in the next section. The prior β grain boundaries were crooked. This was further evidence of a nonequilibrium microstructure, obtaining from the immediate cooling following deformation in the ingot breakdown operation.

3.3.3 Forging Macrostructure

Macro-etching of the forging revealed weak flow lines near the forging O.D. on the LR plane. The flow lines extended outward beginning at 110 mm radially from the

100 μm
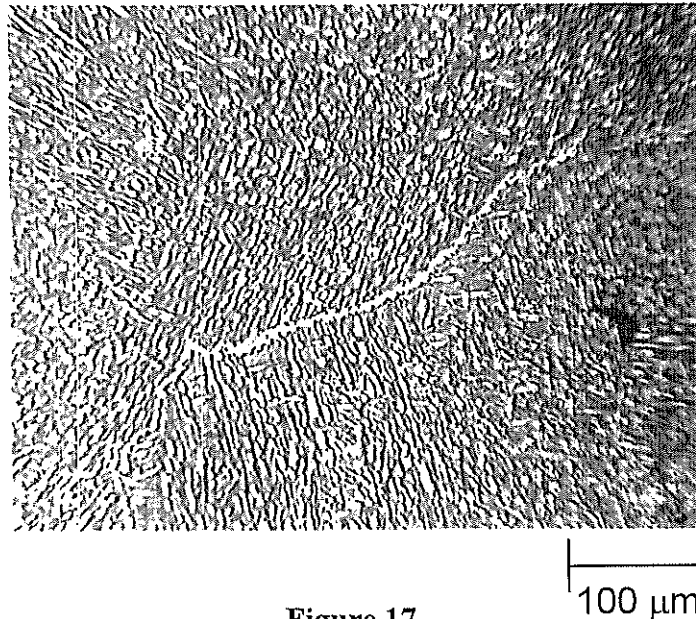
Figure 17
Grain boundary precipitation in the billet LR plane at
the center. Kroll's etch.

center. Flow lines displayed the classical shape for an open die upset forging, roughly parabolic, focusing toward the center. This shape parallels the barreling that obtains from die friction. Flow lines were not photographically reproducible. Shear bands were not observed. The minimal number of flow lines was attributable to the isothermal forging process, where dynamic recrystallization was most likely active, and also to the β solution treatment given to the forging where recrystallization also occured. The forging displayed a slight change in the prior β grain size at *ca.* 110 mm radially from the forging center which was coincident with the observation of flow lines. Figure 18 illustrates the macrostructure on the LR plane. This radius corresponded to the outside diameter of the initial die/billet interface. The material outside this radius was not initially in contact with the dies, and was only brought into die contact because of friction at the die interface.

Based on the macrographs of Figure 18, average, *i.e.*, considering anisotropy, prior β grain sizes were ASTM M9.4 (1.4 mm nominal dia.) and ASTM M10.0 (1.1 mm nominal dia.) for the LR plane of the forging, inside and outside the 110 mm radius, respectively. This marginally exceeded the precision of ±M0.5 in the ASTM grain size number.

The material just inside *ca.* 110 mm (Figure 18a, c), showed slight anisotropy in prior β grain size: G9.7, G9.2, G9.6 in R, L and C principal directions, respectively. In the LR plane, the anisotropy exceeded the minimum threshold of M0.5 ASTM grain size number. Quantitatively, per Equation 10, the anisotropy in the L orientation of the LR and LC planes was $\Omega = 10\%$. The elongation of prior β grains in the L direction did not
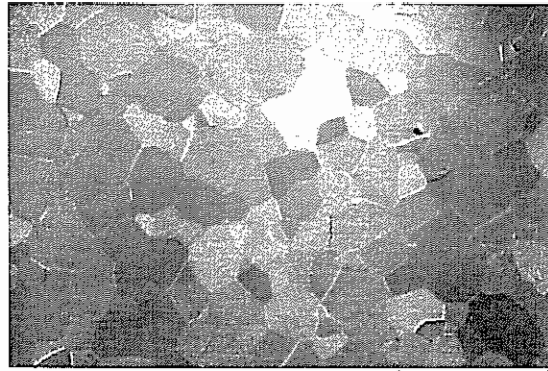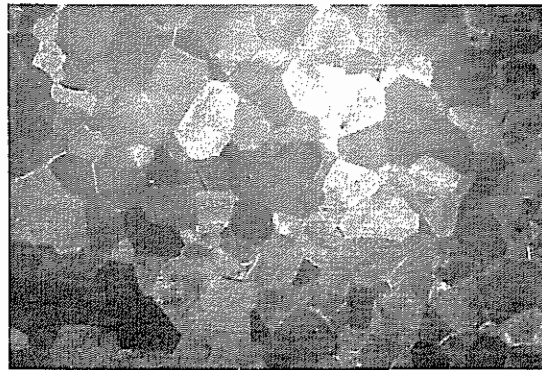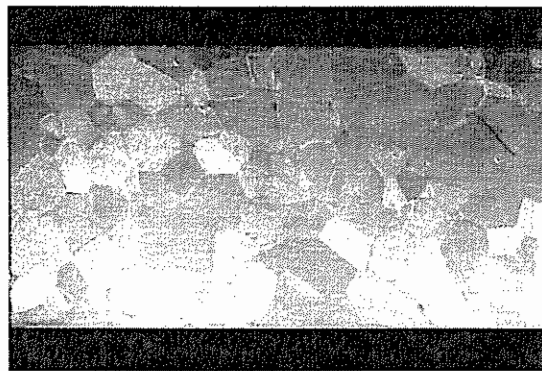
Figure 18
Forging macrostructure a. LR plane centered at *ca.* the 110 mm radius, b. LR plane
at the O.D., c. RC plane at *ca.* the 110 mm radius. Keller's etch.

64

make immediate sense given that the L direction was the upset direction. The anisotropy may have been an artifact from the billet, where 35% to 38% anisotropy was noted along the L axis. The anisotropy also was evident in the calculation of the number of grains per mm^2. Following Equation 11, N_A was 0.54, 0.53 and 0.63 grains $\cdot$ mm^{-2} for the LR, LC and CR planes, respectively.

The range of grain sizes observed in the forging were within that observed in near α alloys, c.f. Allison, et.al.,[72] Guo and Baker[74] and Blenkensop, et.al.[5] The finer grain size in the forging vs. the billet (M8.5 or 1.9 mm nominal diameter) shows that some recrystallization was occurring during forging or heat treating. Whether this was dynamic or static recrystallization could not be determined based on the evidence available. The large prior β grain sizes in the forging were not unexpected, given the high grain growth rates observed in β titanium, c.f., Allison and Baker.[72]

3.3.4 Forging Microstructure

Investigation of the forging revealed a significantly nonequilibrated microstructure. Features such as curved prior β grain boundaries and prior β grains with fewer than 6 sides were prevalent at all locations and all orientations. A four-grain corner was observed in one section. Most of the irregularly shaped prior β grains were significantly smaller than the regularly shaped, i.e., 6 sided, grains at their boundaries. Most of the grains with less than 6 sides displayed convex curvature compared with the surrounding larger grains. These grains were thus quenched in this state before reaching a state of surface energy equilibrium. That some of these small grains with fewer than 6 sides had

concave curvatures was in conflict with the concepts of surface energy driven grain growth.[78] It was possible that these small grains were instead artifacts of sectioning. However, while opportune sectioning can explain the size, it cannot explain the observation of fewer than 6 edges. The latter case is not topologically possible except if the section plane is coincident with the center of a grain corner junction, and marginally non parallel to a grain face. In this latter case, a triangular prior β grain would be possible, however, given the extent of grain boundary α_2 observed, this face would be indicative of the grain boundary microstructure and not that of the grain interior. These 3 sided grains showed the same microstructure as the other grains.

The microstructure of the forging was characterized as fine Widmanstätten at all locations within the forging. The Widmanstätten plates were discontinuous. This was consistent with other work with α_2 alloys, such as that of Lukasak and Koss[79] in Ti-Al-Nb after β phase solution heat treatment.

At the center of the forging, the plate size appears smaller in the CR planes. This is illustrated in the isometric view of Figure 20. At the center, the LR and LC planes are degenerate, hence, the observed microstructures properly were identical. Triple points were selected to show the repeatability of the observations over multiple grains. The remaining locations at various radii had isotropic Widmanstätten structures irrespective of the cutting plane location about the forging axis.

The material inside the initial die-contact circle showed essentially the same Widmanstätten plate size, except the CR planes shown in Figure 20. However, outside

66

the initial die-contact circle, the Widmanstätten plate size was significantly smaller. This progression is illustrated through comparison of the LC face in Figure 20 and the photomicrograph of Figure 19. Outside the initial die contact circle, the structure was isotropic. No differences in plate size from CR vs. LR or LC principal planes were observed.

50 μm
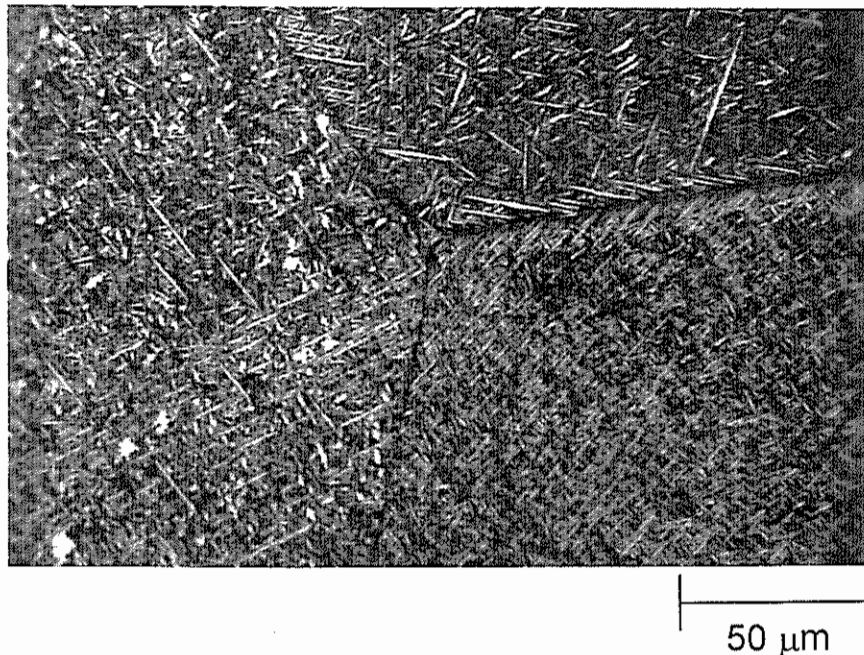
Figure 19
Reduced Widmanstätten plate size at the O.D. of the forging CL,
T/2 plane, Kroll's etch.

The abrupt change in plate size near the OD, corresponds to the finer prior β grain sizes observed in the macrostructural study of the forging. While finer plate sizes are typically associated with higher cooling rates,[12] this does not explain the abrupt change between the inner and outer initial grain boundary circle regions. This behavior cannot be related back to the structure of the billet, where the grain size was independent
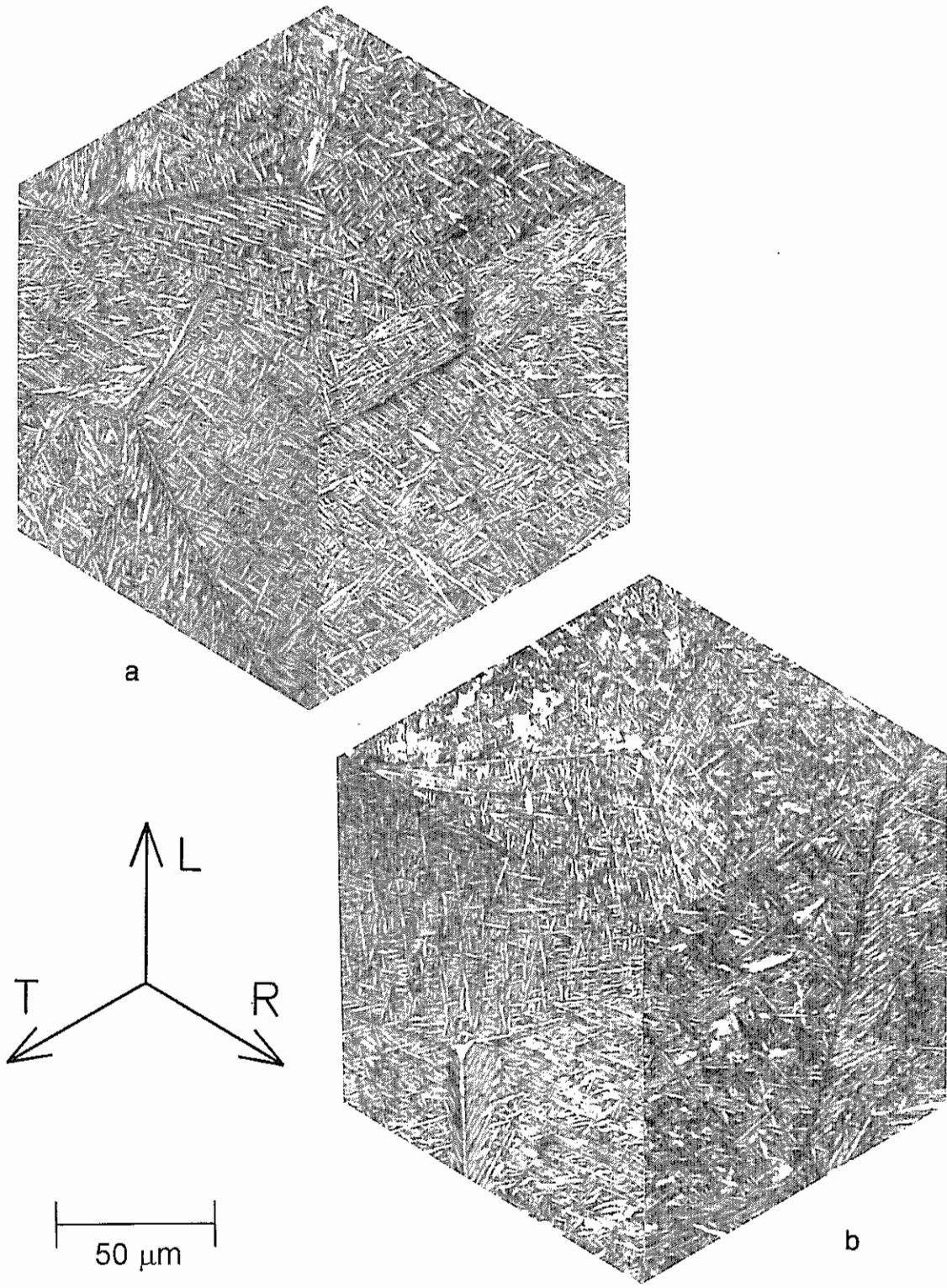
Figure 20
Optical isometric view of forging microstructure at the center: a. on the T plane; b. on the $T/2$ plane, Kroll's etch.

of radial location. It is most likely the result of the differences in the extent of deformation experienced by material on either side of the initial die contact circle.

At all locations, an α_2 grain boundary phase along prior β grain boundaries was observed. This is revealed in the pseudo-isometric views of Figure 20. An exceptionally excessive and raged example is presented in Figure 21a. Here, the grain boundary phase is clearly discontinuous. In the predominance of cases, the grain boundary precipitate appeared on casual examination to be continuous. However, closer examination revealed the discontinuous nature of the grain boundary α_2.

The Widmanstätten morphology was observed to follow the system proposed by Dubé[61] for ferrite precipitation in plain carbon steel. Grain boundary allotriomorphs were observed at all prior β grain boundaries. Based on the light grey scale, this structure consisted of α_2 and is commonly called grain boundary α within the titanium community. As noted in the background to this chapter, the presence of a grain boundary phase in α + β titanium alloys following β heat treatment is common.[69,70,71]

Primary (originating at the prior β grain boundary) as opposed to secondary (originating from the grain boundary phase) Widmanstätten sideplates were observed at the prior β grain boundaries, as shown in Figure 21a. Close examination of the prior β grain boundary in Figure 21a revealed a thin layer of β between the grain boundary phase and the primary Widmanstätten sideplates. A more typical example of primary Widmanstätten precipitation is shown in Figure 21b. This was in contrast to observations of Aaronson[61] in steel, where secondary sideplates dominate, and the primary morphology

a

50 μm

b

50 μm
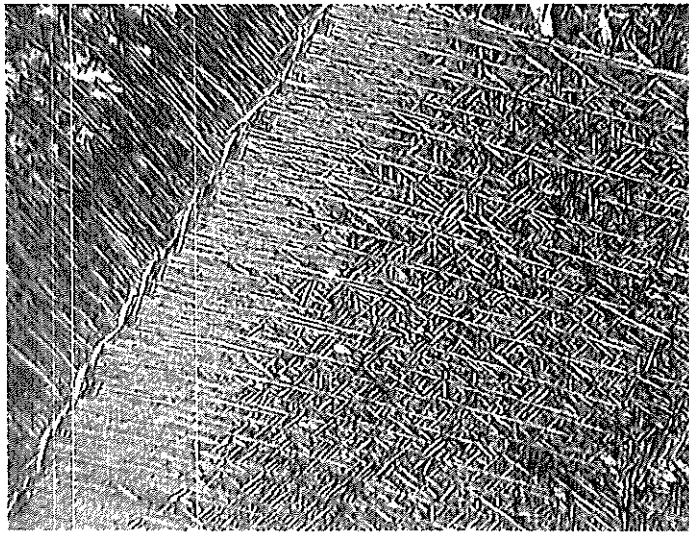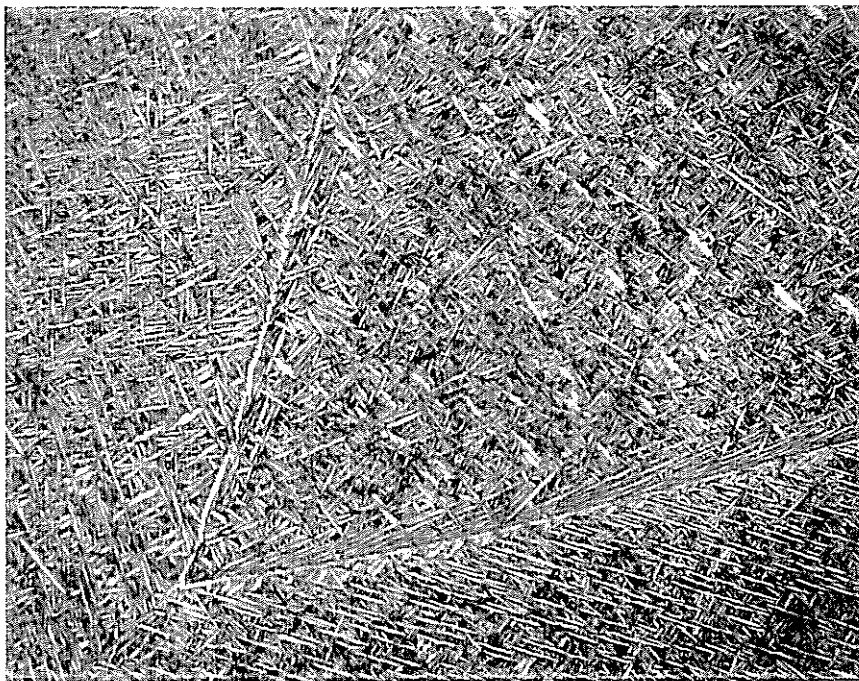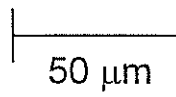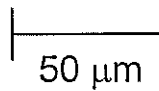
Figure 21

Widmanstätten α_2 precipitation morphology: a. primary side
plates (atypical); b. primary side plates (typical); c. secondary
sawtooth; d. possible idiomorphs (lower prior β grain), 4 grain
corner (Continued...).

70

c

25 µm

d

50 µm
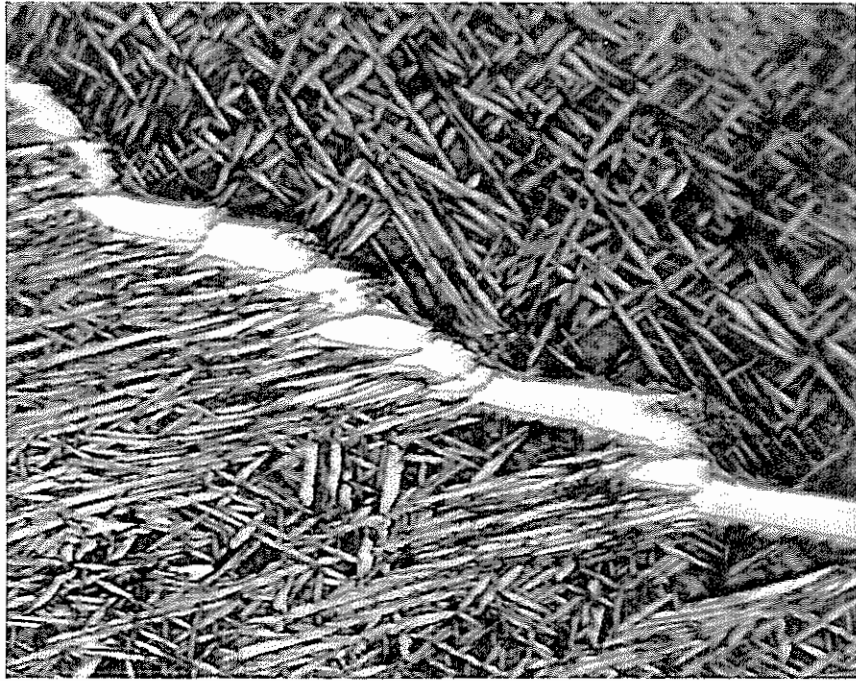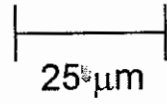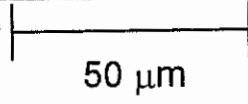
Figure 21 Continued

71

only readily occurs during annealing at temperatures near the eutectoid. However, without knowing the kinetics of α phase precipitation in the alloy, it is not possible to comment further. It is possible that the secondary sideplates formed during the relatively short transient period below the β transus, as shown in Figure 2.

Sawtooth Widmanstätten α_2 was observed at some prior β grain boundaries as shown in Figure 21c. The sawtooth morphology grew from the grain boundary phase (allotriomorph), and not from the actual prior β grain boundary of the adjacent prior β grain. Thus, this structure was classified as secondary sawtooth. Finally, it was not clear from this investigation whether the low aspect ratio features shown in Figure 21d were grain boundary idiomorphs, artifacts from sample polishing or transverse plate cross sections. These features were evident throughout the forging. Their appearance in isolated grains would favor the latter. The hard (α) -- soft (β) nature of titanium alloys can cause smearing of the soft phase, which appears much like the subject features. However, here it is the α_2 phase that would have to be smeared. This seems unlikely given its hardness relative to β. Figure 21d also shows an uncommon four grain corner.

3.3.5 Optical Image Analysis

The Widmanstätten α_2 orientation roses for the forging metallographic sample at the center are presented in Figures 22, 23 and 24. Each Figure corresponds to a principal plane at the center of the forging near the surface. Subfigure d always is an arithmetic average of the three individual histograms. In this group of Figures, subfigure e graphically illustrates the number of grains included in each analysis.

72

Widmanstatten Plate Orientation Rose
Forged Ti-25-10-3-1 Sample 1A-1
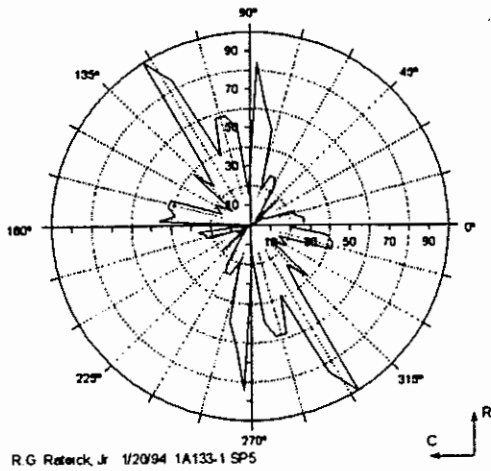
Widmanstatten Plate Orientation Rose
Forged Ti-25-10-3-1 Sample 1A-2
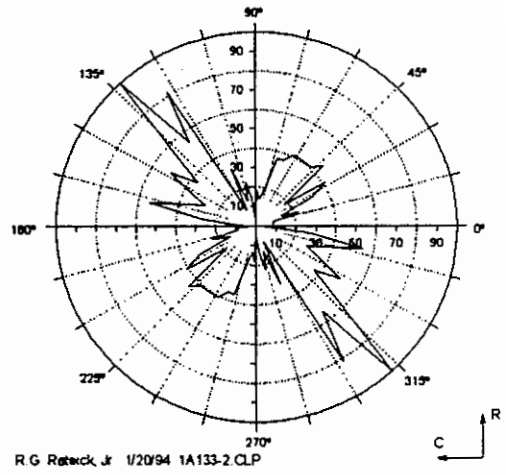
R.G. Rateick, Jr   1/20/94 1A133-1 SP5

R.G. Rateick, Jr   1/20/94 1A133-2 CLP

a

b

Widmanstatten Plate Orientation Rose
Forged Ti-25-10-3-1 Sample 1A-3

Widmanstatten Plate Orientation Rose
Forged Ti-25-10-3-1 Sample 1A-4

R.G. Rateick, Jr   1/20/94 1A133-3 CLP

R.G. Rateick, Jr   1/20/94 1A133-4 CLP

c
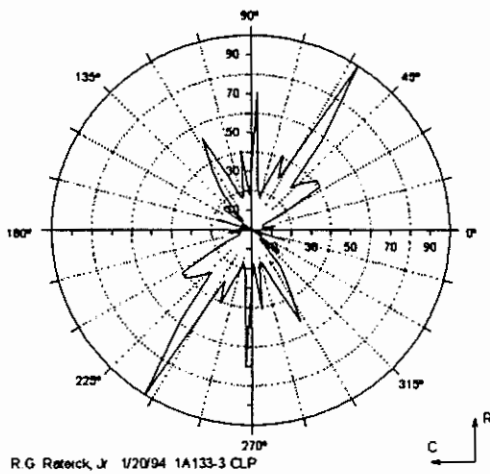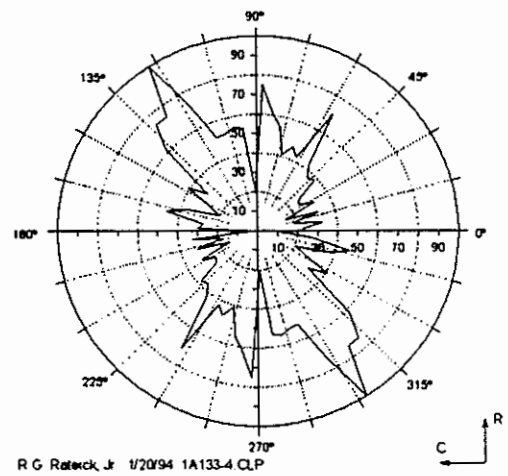
d

Figure 22

Widmanstätten orientation roses for the CR plane at the surface: a. grain 1; b. grain
2; c. grain 3; d. mean rose; e. image analysis region for the average case.
(Continued...)
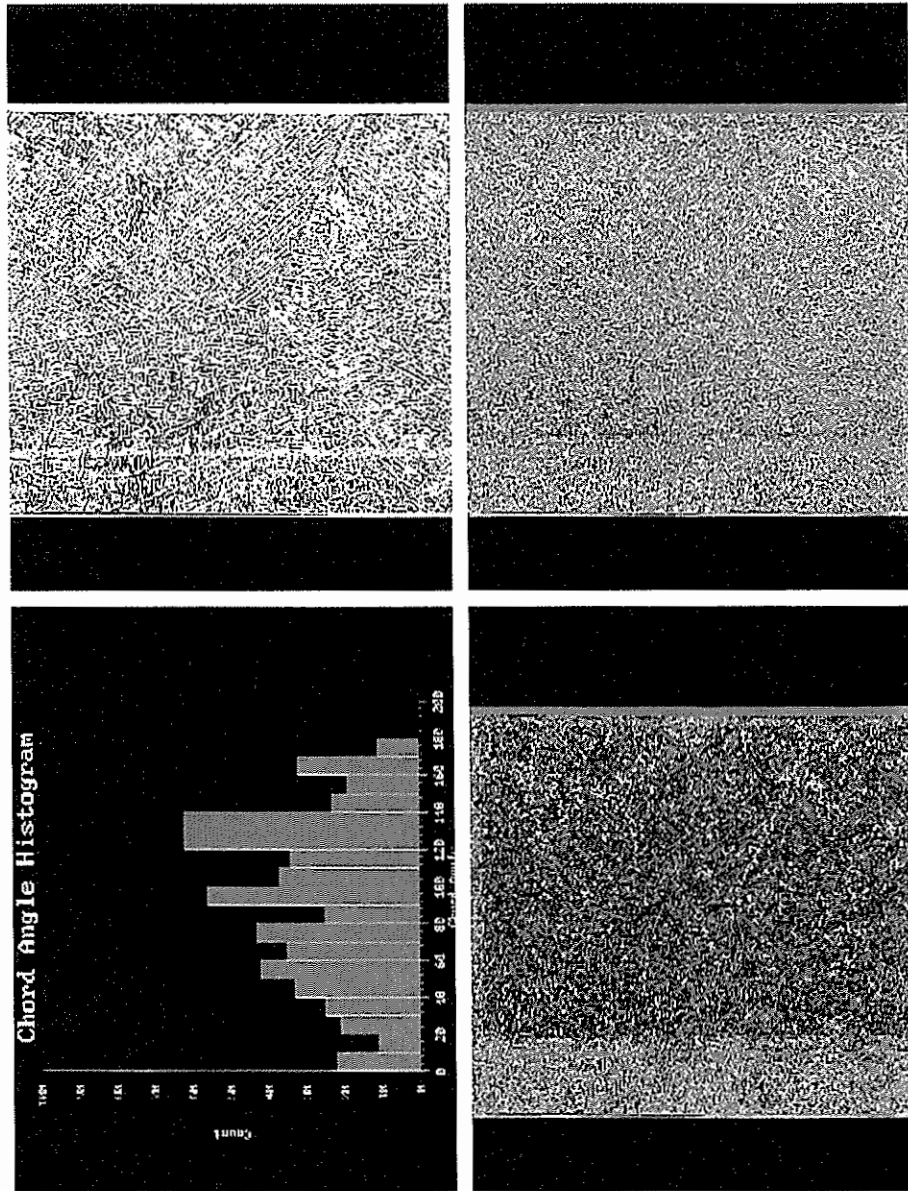
d

e

Figure 22 Continued

Widmanstatten Plate Orientation Rose
Forged Ti-25-10-3-1 Sample 1B-1
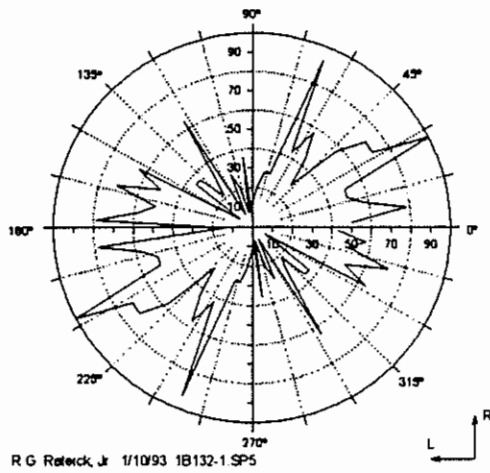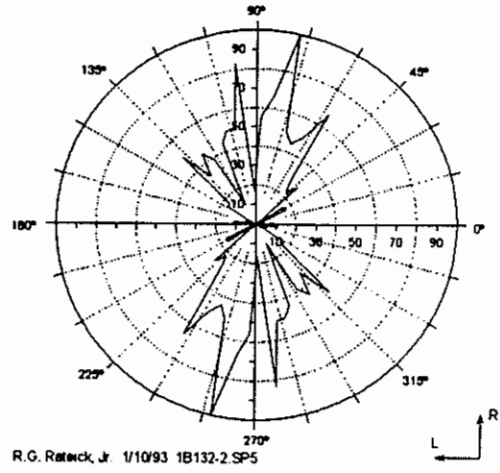
R G Rateick, Jr 1/10/93 1B132-1 SP5

a

Widmanstatten Plate Orientation Rose
Forged Ti-25-10-3-1 Sample 1B-2

R.G. Rateick, Jr 1/10/93 1B132-2 SP5

b

Widmanstatten Plate Orientation Rose
Forged Ti-25-10-3-1 Sample 1B-3

R.G Rateick, Jr 1/10/93 1B132-3 SP5

c

Widmanstatten Plate Orientation Rose
Forged Ti-25-10-3-1 Sample 1B-4

R G Rateick, Jr 1/10/93 1B132-4 SP5
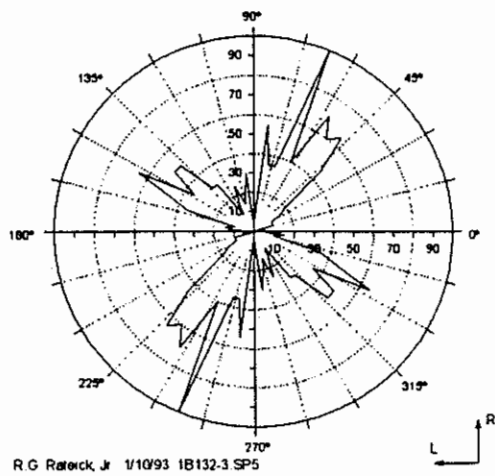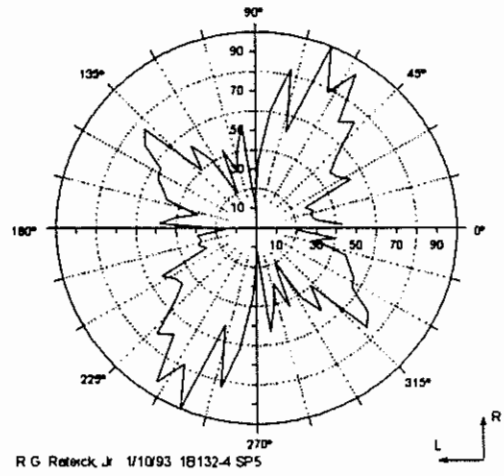
d

Figure 23
Widmanstätten orientation roses for the LR plane at the surface: a. grain 1; b. grain
2; c. grain 3; d. mean rose; e. image analysis regions for the grains respectively
located on the page.

75

b

d

a

c
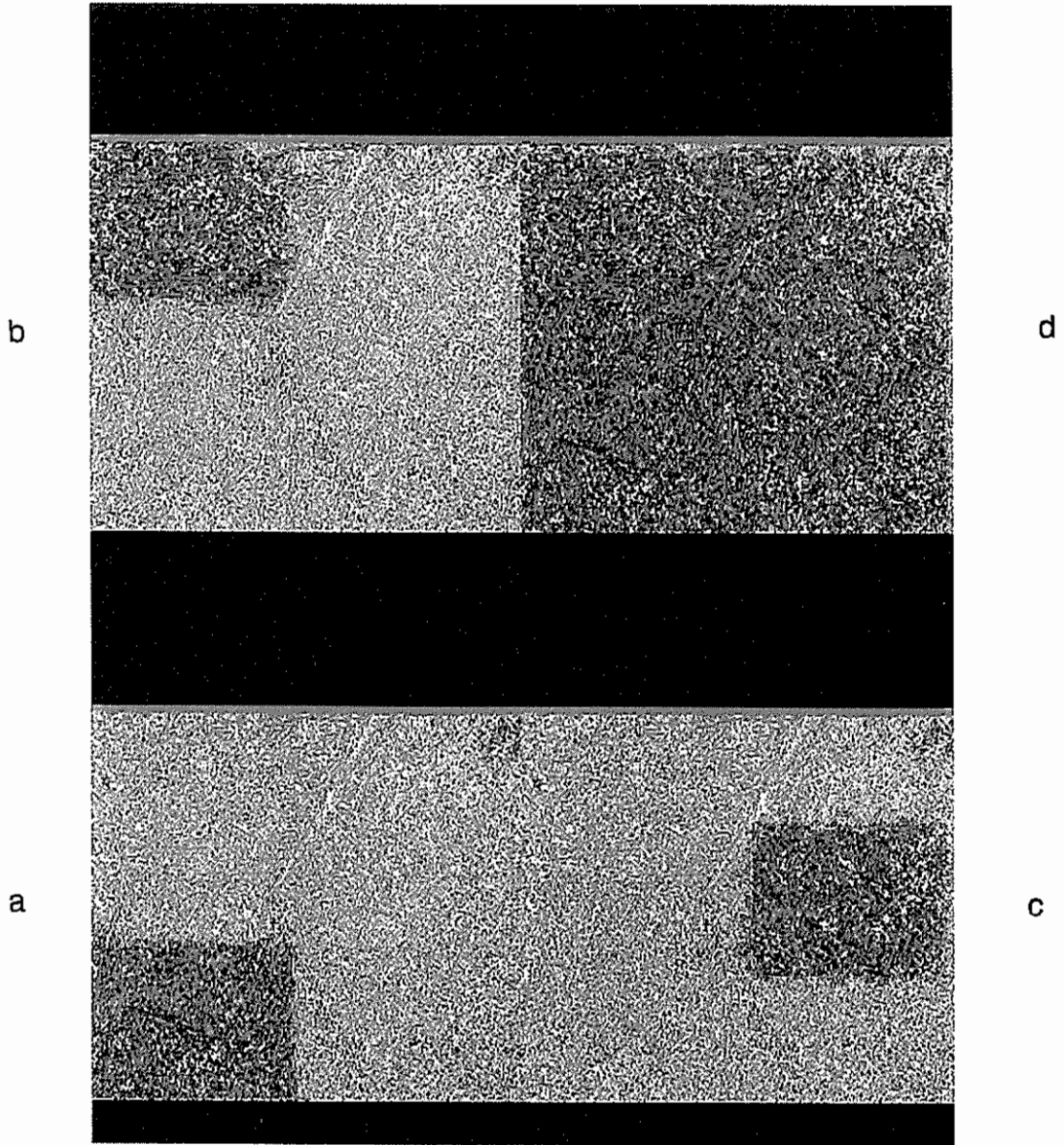
e

Figure 23 Continued

Widmanstatten Plate Orientation Rose
Forged Ti-25-10-3-1 Sample 1D-1
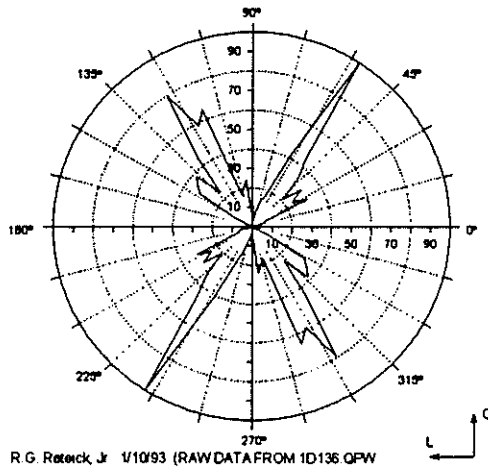
Widmanstatten Plate Orientation Rose
Forged Ti-25-10-3-1 Sample 1D-2
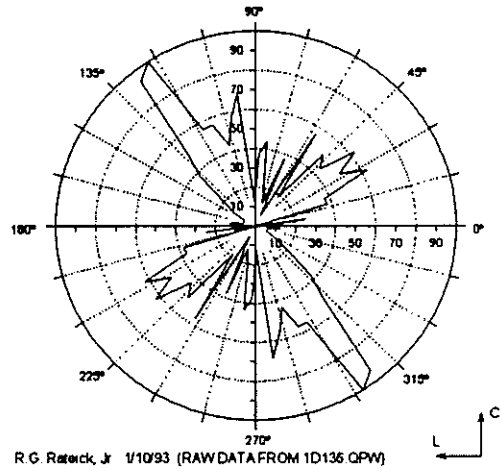
R.G. Reterck, Jr   1/10/93 (RAW DATA FROM 1D136 QPW)

R.G. Reterck, Jr   1/10/93 (RAW DATA FROM 1D136 QPW)

a

b

Widmanstatten Plate Orientation Rose
Forged Ti-25-10-3-1 Sample 1D-3

Widmanstatten Plate Orientation Rose
Forged Ti-25-10-3-1 Sample 1D-4

R.G. Reterck, Jr   1/10/93 (RAW DATA FROM 1D136 QPW)

R.G. Reterck, Jr   1/10/93 (RAW DATA FROM 1D136 QPW)

c
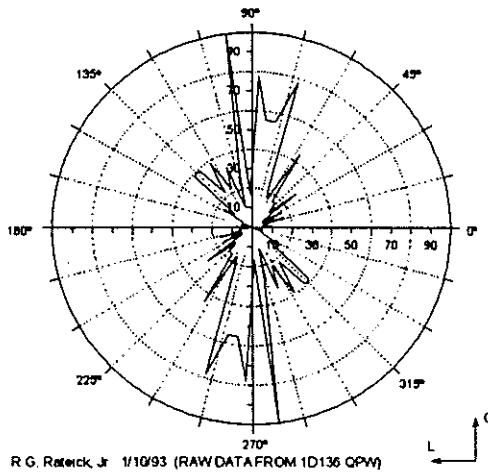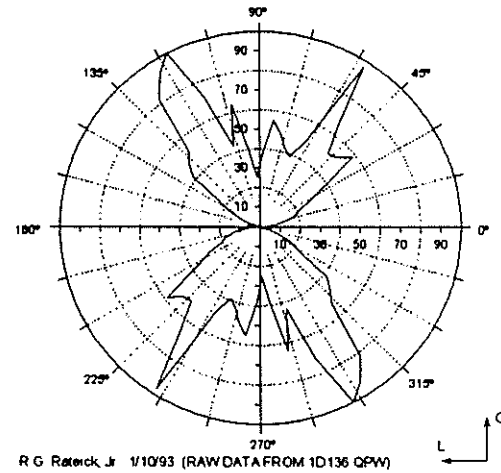
d

Figure 24

Widmanstätten orientation roses for the LC plane at the surface: a. grain 1; b. grain
2; c. grain 3; d. mean rose; e. image analysis regions for the grains respectively
located on the page.

b

d

a

c

e
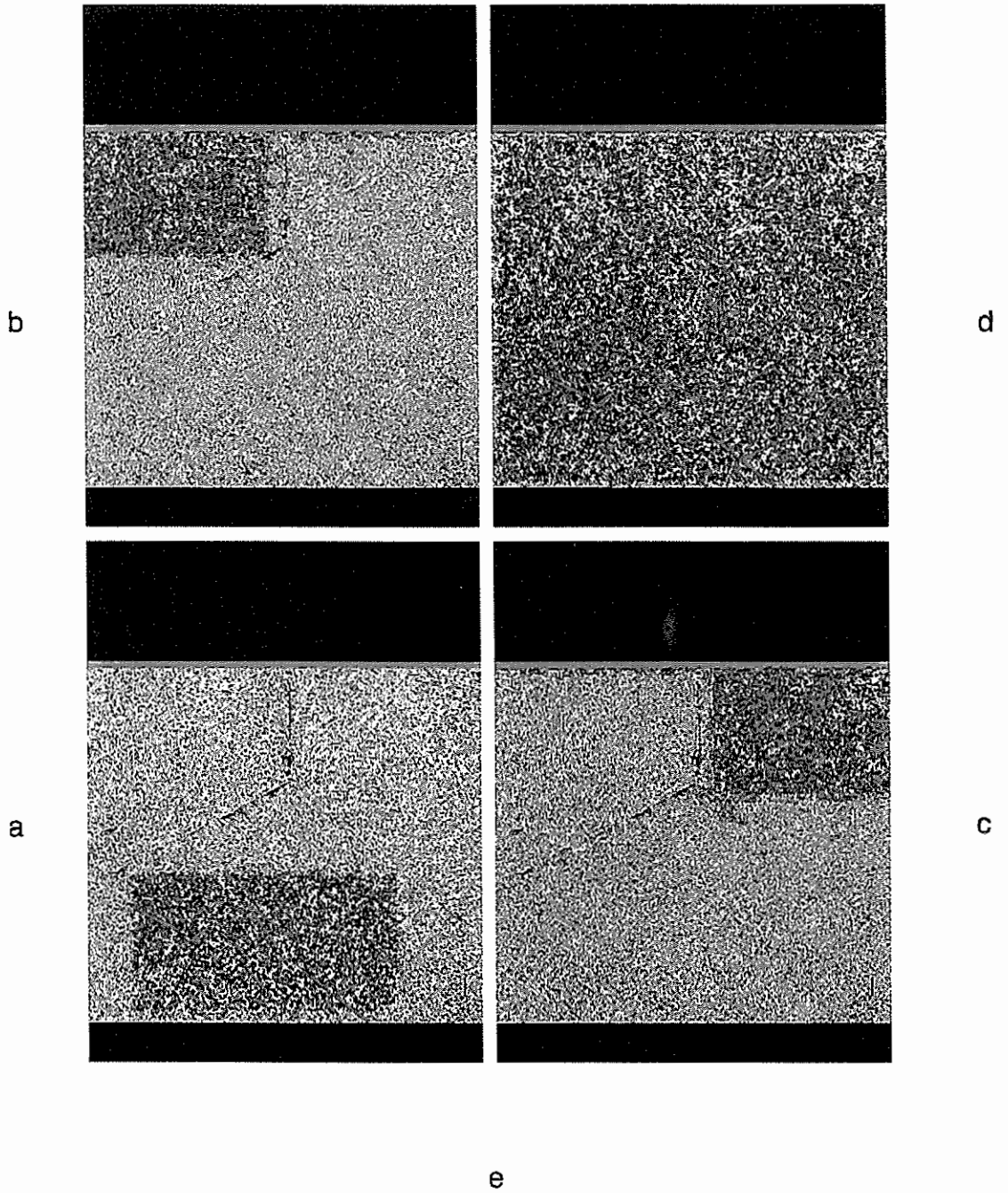
Figure 24 Continued

The α_2 plates formed on cooling from solution treatment in the single phase β phase field have been shown to follow the Burgers orientation relationship: $(0001)_{\alpha2} \parallel (011)_{\beta}$; $<11\overline{2}0>_{\alpha2} \parallel <111>_{\beta}$, *cf.*, Weykamp, *et.al.*[66] The α_2 and β interface in Ti-25-10-3-1 was wavy, showing approximately: $\{10\overline{1}0\}_{\alpha2} \parallel \{211\}_{\beta}$, $<11\overline{2}0>_{\alpha2} \parallel <111>_{\beta}$.[64] The multiplicity of the $\{211\}$ planes in a cubic lattice are 24. Of these planes, one half are non parallel. The α_2 plates thus can form with 12 unique planar orientation variants from a prior β grain. Therefore, in an arbitrary planar cross section of the prior β grain, a maximum of 12 independent α_2 variants are possible. However, these traces do not have to be on consecutive evenly spaced chord angles. Many are only slightly non parallel. Thus, within the angular resolution employed here, only 4 to 5 traces are expected in a general case as opposed to 12. The orientation roses illustrate between 2 and 3 strong α_2 variants for each individual prior β grain analyzed.

These data do not show conclusively whether all possible variants of α_2 plate formation, as predicted from the interface relation, occur with the same probability. However, the notion that the α_2 precipitate is most likely microtextured is consistent with other research that has shown that some variants are eliminated or significantly reduced in probability of occurrence through phase transformation texturing of the α phase.[80] Transformation texturing would have occurred during cooling from the β anneal.

While in principle it should be possible to determine the extent of macrotexture from a suitable average of these microtextures, insufficient numbers of grains were analyzed in this study. This is evident in the lack of correlation of the microtextures in

subfigures a-c compared to the average in subfigure d. In recent work by Humbert, *et.al.,*[81] prior β grain textures were determined based on electron back scatter patterns from the Widmanstätten α phase in Ti-6V. It should be noted that the channeling patterns contain more information on α plate orientation than the plate traces in a cross section micrograph. Thus quantitative texture assessments are possible with the former process, as opposed to the latter process employed here.

CHAPTER 4

X-RAY DIFFRACTION

X-ray diffraction experiments have been a principal basis for the determination of Al-Ti phase equilibrium diagrams. Through these studies, and the concomitant application of Vegard's law, a significant database of indexed diffraction patterns exists. Unfortunately, solution of a diffraction pattern is not simply achieved by reference to the ICDD card file. The tertiary and beyond addition of transition alloying elements can greatly affect the observed patterns. The situation is further complicated by ordering of the α_2 phase, which has not been consistently treated in the literature, *i.e.*, representation of d-spacings does not always clearly account for the superlattice structure. Finally, the recent discovery of instability of the α_2 phase further complicates the analysis.

After the literature review, this chapter presents the experimental methods, results and discussion on x-ray diffraction investigations of crystal structure in the Ti-25-10-3-1 forging and billet.

4.1 Background

The following sections present a review of the literature employed in this research to index the diffraction patterns. Note that no single source was sufficient for this task.

The diffraction patterns for the industrial alloy Ti-25-10-3-1 have not been adequately characterized and assessed in the literature.

4.1.1 Early Studies of Ti-Al Binaries

The first studies of phase equilibria in binary Ti-Al, from pure Ti to TiAl$_3$ were performed by Ogden, *et.al.*[82] and by Bumps, *et.al.*[83] Their work did not reveal ordering of the hcp α phase to the DO$_{19}$ α_2 phase. Thus, while both authors presented plots of lattice parameter vs. Al concentration, the effects of changing symmetry were not included. Ordering to DO$_{19}$ results in doubling of the *a* lattice parameter,[84] which in some works is represented as the *a'* lattice parameter.[85] Here, the more common *a* nomenclature is employed, where the context shows the state of ordering.

Discussion of the Ti$_3$Al phase in the literature is muddled, at best. The work of Ence and Margolin[86] identified a Ti$_2$Al phase. The Ti$_2$Al phase has since been found not to be in equilibrium.[87] This controversial work was the basis for the JCPDS card 16-867 for Ti$_3$Al, assigning it correctly to DO$_{19}$ (P6$_3$/mmc space group). Goldak and Parr,[88] using XRD, showed that DO$_{19}$ was the correct structure for Ti$_3$Al. Later work by Ence and Margolin[89] presented XRD data for Ti$_3$Al (Ti-23.1Al). Using hexagonal symmetry, they assigned lattice parameters of *a* = 1.152 nm and *c* = 0.465 nm. This value of *a* has no relation to current data for the JCPDS card 16-867 that gives *a* = 0.4232 nm and *c* = 0.4638 nm. Clark, *et.al.*[90] independent of Ence and Margolin[89] used XRD information in the determination of an early Al-Ti equilibrium diagram. They observed a monotonic decrease in the *c* lattice parameter of the α phase from 0 to 38 at% Al. However, a break

82

was observed in the *a* lattice parameter curve near the Ti_3Al composition. With the corroboration of observed superlattice lines, they attributed the discontinuity to an ordered Ti_3Al phase, α_2. Again, the patterns were indexed for the A3 α phase, thus requiring a doubling of the *a* parameter to represent the ordered structure as DO_{19}.

In summary, Table 2 gives the lattice parameters for the phases found in the binary Ti-Al system from pure Al to Ti_3Al. As discussed in the next section, the effect of transition metal alloying elements on the lattice parameters and equilibrium phases is significant, thus rendering the JCPDS cards of only qualitative significance.

Table 2

Summary of JCPDS Phase Information for Ti and Al-ti

Phase	JCPDS Card No	Symetry	*a* nm	*c* nm
α	5-682	A3, $P6_3/mmc$	0.2950	0.4686
α_2 Ti_3Al	9-98	DO_{19}, $P6_3/mmc$	0.5775	0.4638
β	Not available			

4.1.2   Complex Alloys, the Orthorhombic Phase

The indexing of diffraction peaks in the multinary alloys based on Ti_3Al-Nb is severely complicated by the presence of other phases besides α_2 and β. In addition, the discovery that α_2 is not truly in equilibrium provides further complication. Banerjee, *et.al.*[59] observed formation of an orthorhombic phase (o-phase) in Ti-25-12.5Nb. The new phase was observed to be a transformation product from both the β and α_2 phases. The phase was of the Cmcm space group.[59,91] In work of Weykamp, *et.al.*,[66] on continuous

cooling transformations in Ti-24-11 and Ti-25-11, the o phase was only observed in the latter. However, Peters and Bassi[26] observed the o-phase in isothermal transformation studies in Ti-25-10-3-1. Based on their TTT diagram, the calculated CCT diagram shown in Figure 2 and the work of Ward,[64] it is expected that both phases exist in the Ti-25-10-3-1 forging. Finally, Kestner-Weykamp, *et.al.*[60] observed significant variation in the *a* and *c* lattice parameters of α_2 with Nb concentration for Ti$_3$Al-Nb.

The β phase in Ti-Al-Nb alloys with high Nb concentrations (*ca.* 5 at. % Nb[92]) has been observed to order into a B2 structure on rapid (water quench) cooling, as opposed to an α martensite.[93,94] Morris[95] observed the B2 phase in a Super-α_2 type alloy. The B2 phase has been included in the TTT diagram for Ti-25-10-3-1 by Peters and Bassi.[26] These observations were based on TEM. However, according to Suryanarayana and Lee,[92] the superlattice lines from the B2 structure were too low intensity for observation by XRD.

Other structures have been observed in Ti-Al-Nb-X alloys such as ω-type phases (ω: P6/mmm, trigonal ω, ω', ω'': P$\bar{3}$m1), and B8$_2$ (P6$_3$/mmc), as summarized by Bendersky, *et.al.*[96] More recently, a DO$_3$ type structure has been observed in Ti-24-11,[97] again using TEM. The presence of these phases has not been reported based on XRD patterns.

4.1.3   Summary, Basis for Pattern Indices

Diffraction peak indexing was performed on the data generated at Notre Dame using the work of Clark, *et.al.*,[83] for the α_2 phase, Kestner-Weykamp, *et.al.*,[60] for the α_2

and o phases in Ti-24-11, Skinner[98] for the α_2 and o phases in Ti-25-10-3-1 and Ward[64] for confirmation of o phase determinations based on his work on Ti-25-10-3-1.

Neither x-ray diffraction patterns nor lattice parameter data were available in the literature for the intermetallic Ti-Al-Nb-X alloys. Peaks corresponding to the β/B2 phase were initially indexed based on the lattice parameter for pure Ti at $1173°C$[99] as corrected for temperature and then empirically corrected for the effects of alloying elements, as described later.

4.2   Experimental Procedure

X-ray diffraction (XRD) experiments were performed at the University of Notre Dame and at Lambda Research, Inc.[*] Work at Lambda Research was performed by Tom Easley under the cognizance of Paul Preve. The objectives of XRD work were as follows:

- Obtain an initial qualitative measure of crystallographic texture

- Identify α_2 reflections suitable for pole figure determination

- Identify possible convolution of α_2 and β peaks

- Determine the lattice parameter of the α_2 phase.

---

[*]   Lambda Research, Inc. 5521 Fair Lane, Cincinnati, OH 45227.

4.2.1 XRD Sample Preparation

Test samples taken from the forging for XRD analysis were intended for pole figure analysis. Figure 28 shows the labeling scheme and location. Samples were traveling wire electrical discharge machined from the forging. Analysis planes were parallel to the RC principal planes of the forging. The RC analysis planes of the samples were subsequently wet ground on 320, 400 and 600 grit SiC paper to remove the recast surface. Polishing was performed using 6 μm diamond, 1, 0.3 and 0.05 μm Al_2O_3. The specimens were macro etched for 70 s in 45%H_2O + 45%HNO_3 + 10%HF (vol.%)[76] to remove the cold worked surface layer. XRD analyses of the abrasives were performed to identify possible interferences.

The XRD pattern for the billet was determined using a sample on the LR plane machined from near the O.D. The analysis surface was wet ground using 320, 400 and 600 grit SiC paper. No etching was done.

4.2.2 Diffraction Experiments

Due to a machining error, the samples from the center of the forging (samples 25T, 25T/2, 25T/4) were cut to only 15 mm diameter as opposed to the 25 mm diameter requested. These samples were subsequently found unusable for pole figure work due to the large grain size. However, they were used for the XRD study at Notre Dame. A special sample holder was machined from virgin TFE to adapt the small sample to the Diano holder. The holder was notched in the plane of the beam to reduce peak artifacts obtaining from the reflections in the TFE. Interference from the TFE was expected to be

86

most likely at angles less than 77° 2θ, where the irradiated sample length[100] exceeded the specimen diameter. A diffraction pattern was generated from the sample holder for identification of possible interferences.

Initial XRD patterns were generated at Notre Dame using the Diano SPG-2 diffractometer employing a Fe tube. Significant fluorescence of the Ti by the Fe radiation obscured low angle reflections. While it was possible to electronically filter the fluorescence through signal processing, the work was repeated with a Cu tube. Experiments were performed using graphite monochromated Cu K_α radiation generated at 45 KV and 30 mA. The diffractometer incorporated a 3° beam slit and 0.2° detector slit. The detector slit indicated a time constant of 6 sec. for a scan rate of 1° 2θ s⁻¹. The proportional counter high voltage was set at 2450 V. Occasionally, slower scan rates were employed to improve the 2θ resolution of peak maxima.

Diffraction data were acquired by a Macintosh computer running Notre Dame developed software (X-Ray 500). The raw data files in ASCII format were transferred to an IBM compatible P.C. for subsequent analysis. Peak maxima were determined using the Jandel Scientific TableCurve program to fit Gaussian or Lorentzian distributions to the data. The appropriate peak fit was identified by the maximum correlation coefficient. The peak maxima were identified by the zero of the first derivative of the respective curve fit. Background subtraction was not performed. Note that this software was not capable of $K_{\alpha 1}$ $K_{\alpha 2}$ deconvolution, nor was it capable of the superior Pearson-7 curve fits. Diffraction patterns were prepared using Jandel Scientific SigmaPlot.

Diffraction experiments were also performed at Lambda Research[101] in conjunction with pole figure work. This was a subcontract activity under the development program reported here. Diffraction was obtained using graphite monochromated Cu K_α radiation. The diffractometer was calibrated using NIST standard silicon reference material no. 640. Data analysis consisted of Golay moving average smoothing, followed by derivative based peak maxima location.

4.2.3 Lattice Parameter Determination for α_2

Lattice parameters of the α_2 phase were determined using the method developed by Cohen[102] as described by Cullity[103] and Kaelble.[106] This was a least squares approach to minimizing random error by fitting the lattice parameter estimates at various *hkl* to some function giving the variation of error with θ and extrapolating to $\theta = 0$. The Cohen least squares extrapolation given by Cullity[103] was based on the Bradley and Jay[104] model for systematic error variation with $\cos^2\theta$. This model is appropriate for the Debye-Scherrer method. For the application of Cohen's method in the Notre Dame evaluation of lattice parameters, it was necessary modify the curve fit to model systematic error obtaining from the diffractometer. For a diffractometer, where displacement of the sample from the diffractometer axis is the primary source of systematic error, Cullity[103] gives its variation ξ as

$$\xi = \frac{\cos^2\theta}{\sin\theta} \tag{12}$$

The applicability of this error model to the Diano SPG-2 diffractometer was shown by Lehman.[105] The Cohen least squares model was then subsequently recast in terms of Equation 12, resulting in the following matrix formulation:

$$\begin{bmatrix} \sum \alpha^2 & \sum \alpha\gamma & \sum \alpha\delta \\ \sum \alpha\gamma & \sum \gamma^2 & \sum \gamma\delta \\ \sum \alpha\delta & \sum \gamma\delta & \sum \delta^2 \end{bmatrix} \begin{bmatrix} \dfrac{a\lambda^2}{3} \\ \dfrac{c\lambda^2}{4} \\ A \end{bmatrix} = \begin{bmatrix} \sum \alpha\sin(\theta)^2 \\ \sum \gamma\sin(\theta)^2 \\ \sum \delta\sin(\theta)^2 \end{bmatrix} \qquad (13)$$

Here a and c are the lattice parameters based on hexagonal symmetry, θ is the diffraction angle and A is the drift constant.[106] The value of $\lambda = 0.1541838$ nm was based on a $\frac{2}{3}$ weighted average of $CuK_{\alpha 1}$ vs. $CuK_{\alpha 2}$ component of the doublet. This was necessitated by the inability to resolve the $K_{\alpha 1}$ $K_{\alpha 2}$ doublet. The values of α, δ and γ from

$$\begin{aligned} \alpha &= h^2 + hk + k^2 \\ \gamma &= l^2 \\ \delta &= \cos^2\theta \times \sin\theta \end{aligned} \qquad (14)$$

were determined based on multiple hkl planes with reflections at diffraction angles θ.

4.2.4   Pattern Indexing

The first pass at indexing the diffraction pattern was based on the indexed patterns presented in the literature as referenced in the background section. Unidentified peaks were then subjected to sieves for all possible reflections from hexagonal and orthor-

89

hombic phases. Lattice parameters for these sieves were based on the author's initial estimates for the α_2 phase (not those reported here), and the lattice parameters reported by Kestner-Weykamp, *et.al.*[60] for Ti-25Al-12Nb, respectively. Finally, all peak assignments were checked for agreement with the extinction rules.[107]

Lacking lattice parameter data or an indexed diffraction pattern for the β/B2 phase in a Ti-Al-Nb-X intermetallic alloy, the lattice parameter for pure β titanium, was initially employed in an iterative approach to calculate the β diffraction pattern for the Ti-25-10-3-1. The lattice parameter for pure bcc β Ti was $a = 0.33065$ nm at $1173°C$.[99] Correcting for linear thermal expansion using the thermal expansion coefficient $\alpha = 12.5$ ppm $\cdot$ C^{-1} from $25°C$ to $1127°C$[108], the room temperature value of $a = 0.3249$ nm was estimated. Diffraction angles calculated from this lattice parameter were compared to the measured pattern for the billet. The billet was chosen since metallographic evidence showed a significant β phase concentration. The peak at $57.028°$ 2θ was assigned to $[200]_\beta$, from which a lattice parameter of $a = 0.3231$ nm was estimated. Using this value of a it was possible to calculate the expected diffraction angles for the β phase in the Ti-25-10-3-1. The calculated pattern was then compared against experimental patterns to effect the identification of β peaks.

4.3   X-Ray Diffraction Results and Discussion

The following sections describe the XRD results for the billet and for the forging.

4.3.1   XRD from the Billet

Figure 25 shows the diffraction patterns for the Ti-25-10-3-1 billet. The intensity axis has been presented in logarithmic form to emphasize the low intensity peaks predominating the pattern. The unidentified peaks are attributed to α_2/o. The most intense peak on the pattern corresponds to the $\beta_{(110)}$ reflection. However, as shown in the inset to Figure 25, this peak was convoluted with the $\alpha_{2\ (002)}$ and $\alpha_{2\ (201)}$ peaks at 38.78° and 40.65° 2θ, respectively. Convolution of peaks was a significant factor in the selection of peaks for pole figure determination. Table 3 gives the results of quantitative peak analysis, showing the observed peak positions vs. the calculated peak positions. The $\beta_{(200)}$ was the basis for assignment of β phase peaks. Agreement was excellent, with a maximum error of 0.45% in the observed vs. calculated 2θ positions.   From   the background section, the β phase was most likely ordered to the B2 structure. The extinction rules for B2 provide no restrictions for possible reflections.[107] Hence, superlattice lines would be expected corresponding to: (100); (111); (210); (300); (221). However, only the (210) superlattice reflection was observed. No α_2 reflections were near this peak. The possible o-phase reflections were eliminated from consideration based on extinction relations[107] for the Cmcm space group.

Table 3

Qualitative Analysis of XRD Reflections Form the Billet.

I/Io	Observed		Calculated		d	Plane
	2θ Cu K_a	d	2θ Cu K_a	d	ppm error	
0.05	35.799					(200) α2
0.17	38.789					(002) α2
1.00	39.58	1.210	39.546	1.211	22	(110) β
0.16	40.648					(201) α2
0.05	53.742					(202) α2
0.06	57.028	0.919	57.028	0.919	0	(200) β
0.03	64.218	0.856	64.514	0.854	-33	(210) β
0.11	71.554	0.813	71.558	0.813	-0.26	(211) β
0.04	77.8					(401) α2
0.04	85.062	0.774	84.925	0.774	1.9	(220) β
0.04	97.979	0.779	98.015	0.779	0.7	(310) β

Predominance of the β reflections was not unexpected considering the billet microstructure as shown in Figure 16, and its prior thermal processing in the α_2 + β region. It will be noted in subsequent discussion of the forging XRD patterns that the β phase appears to be in less abundance than in the billet. High cooling rates that most assuredly accompanied cooling of the billet following the final ingot break down forging operation would give rise to retained β. However, the forging was cooled under controlled conditions, indeed under an insulator at times, such that more time passed for decomposition of the β phase.

4.3.2 XRD from the Forging

Figure 26 illustrates the diffraction patterns for the forging, taken at the indicated axial and radial locations. The most striking feature of these patterns is the strong
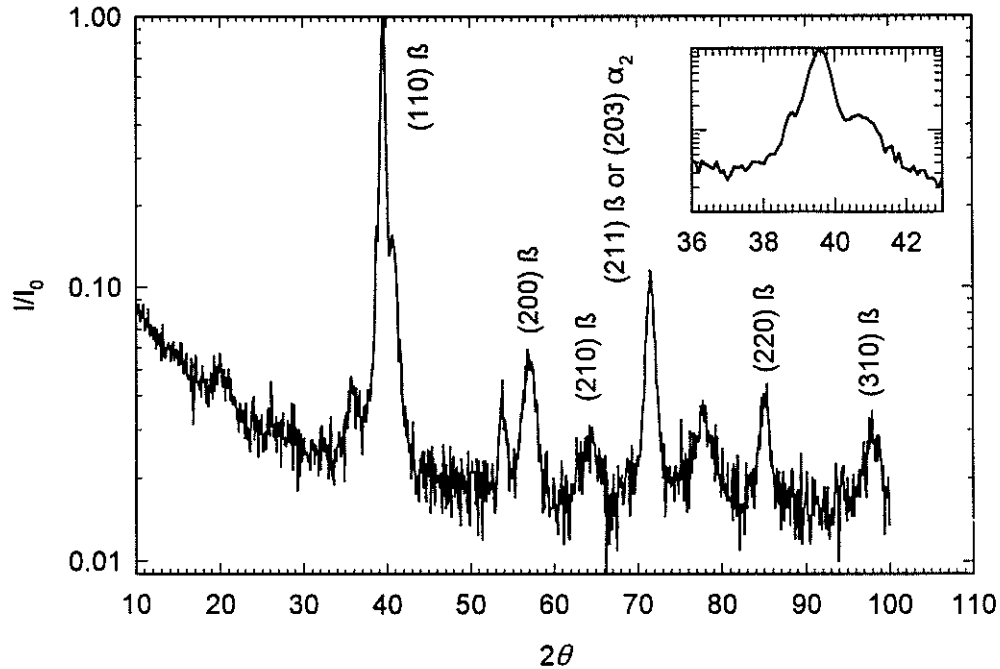
Figure 25

XRD pattern for thebillet LR face in the outer half radius. Inset shows convolution of $\beta_{(110)}$ and α_2 peaks. Monochromatic Cu K_a radiation, $1° \, 2\theta \, s^{-1}$.

variation in peak intensity, most notably the quartet in sample 25T at *ca.* 40° 2θ, which was absent from the remaining patterns. These intensity differences were initially attributed to crystallographic texture. However, after additional consideration, the intensity differences were attributed to grain size effects obtaining from the Widmanstätten precipitation within large prior β grains.

Based on the quantitative metallographic work, the nominal diameter of the average prior β grain section was 1.3 mm (ASTM G = M9.65) within the inner 110 mm radius of the forging. From Equation 11, this corresponded to 0.63 grains · mm⁻¹. For a 3° beam, Diano has provided a table[100] showing the sample irradiated length vs. 2θ. Knowing that the beam was 10 mm high, the irradiated area, and thus, the number of prior β grains irradiated was estimated. In the metallography chapter, it was shown that each
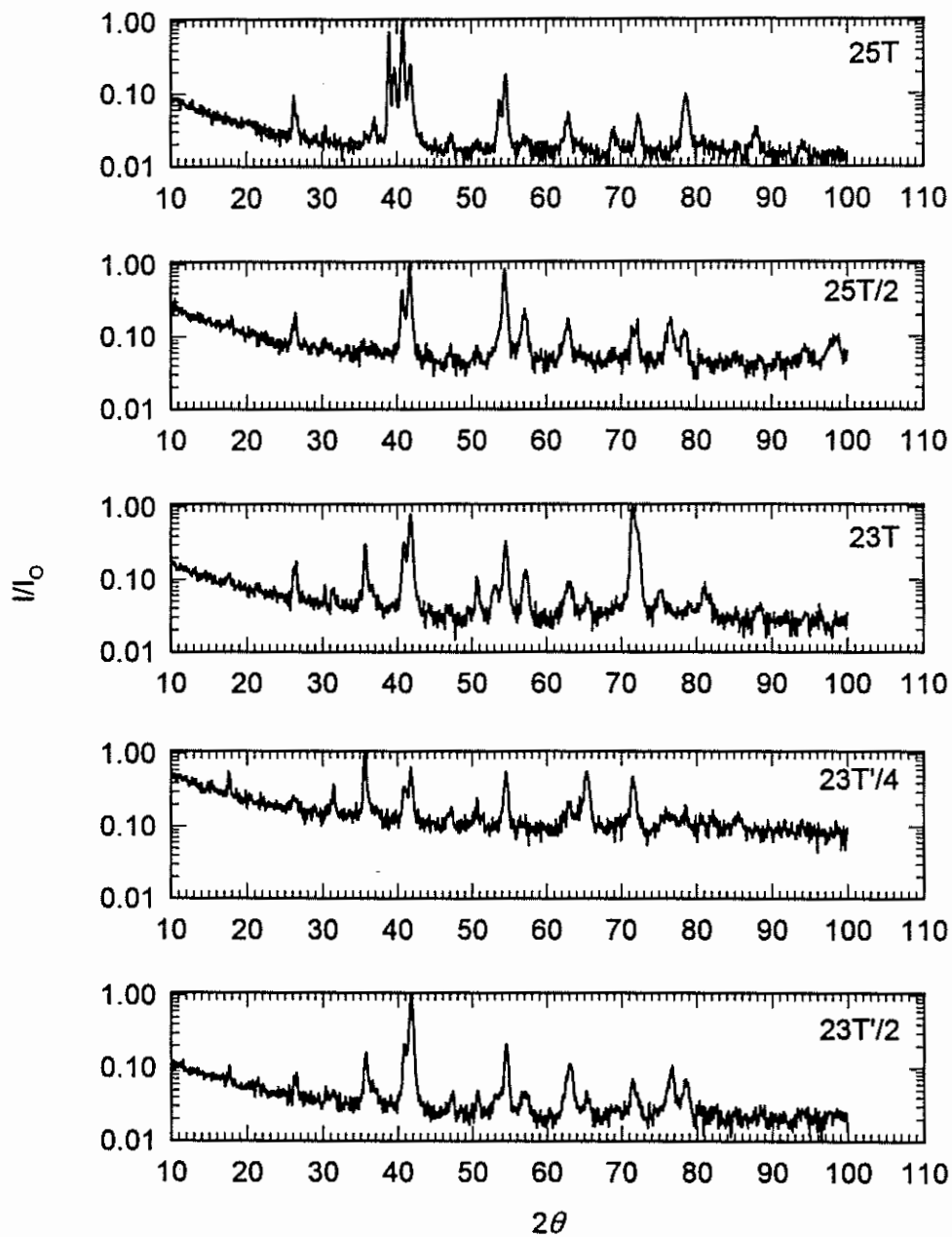
Figure 26

XRD patterns for isothermally forged Ti-25-10-3-1 on the RC plane at indicated positions. Monochromated Cu K_α radiation, 3° beam slit, 0.2° detector slit.

94

prior β grain contained *ca.* 3 unique α_2 orientations of Widmanstätten plates. The actual number of possible reflecting units of α_2 was calculated as a function of 2θ and plotted in Figure 27. Here, the sample size of 25.4 mm limited the irradiated grain count at low 2θ. From these results, a maximum of only 580 reflecting units of α_2 was responsible for the observed diffraction patterns. Note that for samples from location 23, where the diameter was only 12.75 mm, the cutoff is at a maximum of 290 reflecting units. Further reducing this number, of course, was the fact that the diffractometer does not count all reflections occurring in a diffraction cone. If it is assumed that the reflecting units are equiaxed, then Equations 6 and 11 give a unit size of 0.7 mm. According to Kaelble,[106] for stationary samples grains must be less than 0.5 μm for continuous Debye rings to obtain. Thus, the explanation for the differences in peak intensities shown in Figure 26 can be attributed to a combination of texture and large grain effects. As discussed in the texture chapter, the effect of texture was minimal.

Table 4 gives the diffraction peak analysis for the Ti-25-10-3-1 forging. Due to the wide variation in diffraction patterns as shown in Figure 26, this table is a composite of all peaks observed and identified. However, it was primarily based on sample 23T'/2. Lambda research performed a qualitative peak analysis of sample 23T'/2. Their analyses were integrated into Table 4. Of the phases, the identification of the o-phase planes was the least reliable. This resulted from the inavailabiity of accurate lattice parameter information for the o-phase in Ti-25-10-3-1, considering the large lattice parameter variation with Nb concentration shown by Kestner-Weykamp, *et.al.*[60] In addition, o-phase

peaks were in many cases convoluted with α_2 peaks. Intensity information was not given in Table 4 as it was a composite of many diffraction patterns. The two unidentified peaks could not be attributed to any of the metallographic sample preparation supplies. These peaks were not of trivial intensiy.

4.3.3   Lattice Parameter Extrapolation for the α_2 Phase

The lattice parameters for the α_2 phase were determined using Equations 12 to 14. Extrapolation was performed using all reflections from sample 23T'/2 which were attributable to the α_2 phase, *i.e.*, (100), (101), (200), (201), (210), (300), (212), and (401). The calculated lattice parameters were $a = 0.5838$ nm, $c = 0.4625$ nm with $c/a = 0.792$. These compared favorably to the work of Weykamp, *et.al.*[66] on Ti-24-11, where $a = 0.58 \pm 0.01$ nm, $c = 0.48 \pm 0.01$ nm $c/a = 0.83$, as determined based on electron diffraction.
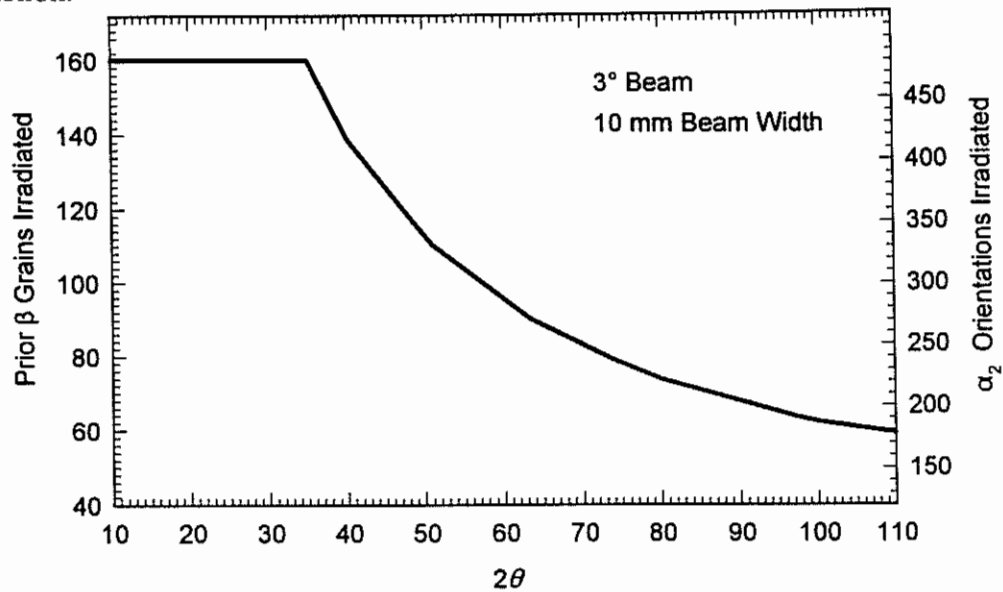
Figure 27

Estimated number of irradiated prior β grains and α_2 reflecting units for a 25.4 mm sample.

Table 4

Qualitative Analysis of XRD Results for the Forging

°2θ		Phase		
Notre Dame	Lambda Research	α_2	O	β
17.61	17.6	(100)		
26.33	26.2	(101)		
	26.4		(021)	
	30.3	(110)		
	31.2		(130)	
35.68	35.5	(200)		
	36.5		(040)	
38.59		(002)		
39.33				(110)
41.75	41.8		(041)	
47.25	47.3	(210)		
50.70	50.7	(112)		
53.10				
	53.7	(202)		
54.54	54.5	(300)		
57.10				(200)
63.07	62.9	(103)		
65.32	64.7			
71.53	71.3			(211)
	72.0		(043)	
75.23		(400)		
76.64	76.3		(402)	
78.53	78.3	(401)		
81.13	81.0		(243)	

97

CHAPTER 5

TENSILE BEHAVIOR

This chapter concerns room temperature tensile and fracture behavior of the Ti-25-10-3-1. The results show that the tensile behavior in the isothermally upset forged Ti-25-10-3-1 material was not significantly influenced by location or orientation in the forging, and hence, not significantly affected by crystallographic texture. Comparison of the results from this research with tensile properties reported in the literature is held off until the results section.

5.1   Background

This section is divided into two subsections dealing with tensile properties in titanium aluminides and fracture in titanium aluminide alloys, respectively. Minimal information on Ti-25-10-3-1 has lead to a necessity to broaden the scope of the background to include Ti-Al binary and Ti-Al-Nb ternary alloys.

5.1.1   Tensile Behavior in Titanium Aluminide Alloys

Plastic deformation in hexagonal metals is typified by a-type glide of $a_0 \frac{1}{3}<11\overline{2}0>$ dislocations on basal, prismatic or pyramidal planes or by $c + a$ type glide of

$(a_o^2 + c_o^2)^{1/2} \frac{1}{3} \langle 11\bar{2}3 \rangle$ dislocations on $\{10\bar{1}1\}$ and $\{11\bar{2}2\}$. The dominant **a**-type glide systems are controlled by the *c/a* ratio. The **c + a** dislocation motion is less prevalent than the **a**-type, being limited to high stress cases where orientation of the crystal makes **a**-type glide less favorable.[109] Operation of only the **a**-type glide systems provides only 4 of the necessary 5 independent slip systems required by Von Mises[110] for general plastic deformation of a polycrystal. However, twinning can also contribute to the Von Mises requirement of 5 independent strains.

Plastic deformation in pure **α**-Ti involves **a**-type glide on basal, prismatic or pyramidal planes.[111] In addition, **c + a** glide has also been observed on pyramidal planes, along with twinning on $(11\bar{2}1)$.[112] Thus, sufficient independent strain components are available for general plasticity in a polycrystal of **α**-Ti.

Marcinkowski[85] accurately predicted the **a**-type dislocation structures found in DO_{19} superlattice Ti₃Al. He predicted based on a suboptimal c_o/a_o ratio, here 0.792 vs. the optimal 0.8165*, $\{10\bar{1}0\}$ planes should dominate slip, with slip on $\{10\bar{1}1\}$ being less prevalent. He also predicted that an **a**-type dislocation on $\{10\bar{1}0\}$ would not dissociate to a superdislocation.

Anderson, *et.al.*[113] and Rosi, *et.al.*[114] investigated the slip systems in pure Ti. They observed that **a**-type slip occurred on $\{10\bar{1}0\}/\{10\bar{1}1\}$ planes, and $\{10\bar{1}0\}/\{0001\}$ planes, respectively. The $\{10\bar{1}0\}$ slip was dominant in both cases. The differing

---

* This is based on the superlattice structure, where the *a* latice parameter is doubled compared to the disordered state.

99

secondary slip systems were attributed to interstitial impurity effects by Churchman,[115] where Rosi[114] employed cleaner material. Twinning was observed by all three authors.

Blackburn and Williams[116] in studies of Ti-(0-25 at%)Al found a-type slip predominating on $\{10\bar{1}0\}$, but at higher strain on $\{10\bar{1}1\}$ and $\{0001\}$, with the basal slip being the most rare. At Al concentrations over 10at%, they observed superdislocations. At Al concentrations over 17at% c + a glide was not observed. Lipsitt, *et.al.*[117] in work specifically on Ti₃Al concurred with Blackburn and Williams,[116] with the exception that they observed some incidences of c + a motion. In addition, no twinning was observed. Sastry and Lipsitt[118] investigated Ti₃Al + Nb, finding a-type dislocations on $\{0001\}$ and $\{10\bar{1}0\}$, with the latter being perfect dislocations, as predicted by Marcinkowski.[85] Again, twinning was not observed.

Dislocation structures in about 20 Ti-Al-X alloys were investigated by Marquardt, *et.al.*[119] *   Unlike the earlier investigations, this work employed true polycrystalline samples heat treated in the $\alpha_2 + \beta$ phase field. They invoked the Schmidt factor to show that c + a slip was only possible when the c axis was aligned within 15° of the direction of applied stress. They further showed that only 1 in 7 prior β grains would contain α_2 favorably oriented for c + a slip to obtain. The Schmidt factor $S = \sin\chi \cos\phi$ is the ratio of the critically resolved shear stress to the applied tensile yield stress as applied to a

---

*   Actual alloy compositions were restricted by the government as Critical Technology.

single crystal, where χ and ϕ are the angle between the tensile axis and the glide plane and Burgers vector, respectively.[120]

It is thus evident that ductility in α_2 based alloys is significantly limited by the lack of twinning and the lack of **c** + **a** glide, which leaves less than the requisite 5 independent slip systems necessary for general polycrystalline ductile deformation. The addition of Nb to Ti_3Al has been observed to activate **c** + **a** type slip. Sastry and Lipsitt[28] noted that the high dislocation density in their samples prevented a quantitative analysis of the actual slip vectors. Recent work by Court, *et.al.*[121] shows that the addition of Nb gives rise to **c** + **a**/2 type slip as opposed to **c** + **a** type slip on addition of up to 4at% Nb. It must be noted that even with the 5 slip systems, Court, *et.al.*[121] observed minimal mobility of these dislocations.

Tensile properties observed in Ti-25-10-3-1 have been reported by Cho, *et.al.*[12] and by Ward.[64] These are discussed in the results and discussion section, in comparison with data from this study.

5.1.2   Fracture Morphology in Titanium Alloys

The literature contains little information on fracture morphology in Ti-25-10-3-1. While Chen, *et.al.*[122] discuss fracture, their material was heat treated in the α_2 + β condition, where the significantly different microstructure precludes comparison to the β solution treated material employed in this research. In a study of α_2 + β and β forgings, Ward[64] observed that all fractures were brittle at room temperature. River marks pointed to the origination site in most cases. The underlying microstructures were evident in the

fracture faces. In β forged material, cracking was observed at slip band intersections at the specimen surface and at prior β grain boundaries. Ward[64] also observed shear crack initiation in this microstructure.

Turning to the more widely discussed fracture morphologies in Ti-Al binary alloys and Ti-Al-Nb ternary alloys provides greater information on the expected fracture morphologies in the Ti-25-10-3-1 alloy. The dominant mode of fracture in Ti_3Al is transgranular cleavage.[118, 117, 123] Blackburn and Williams[116] observed brittle cleavage in equiaxed α_2 along the basal plane. This research implies that crystallographic texture plays an important role in the tensile properties of α_2 alloys. Kerans[123] observed some ductile fracture behavior in fatigue experiments on equiaxed α_2; however, this was not observed in the monotonic tensile experiments reported by the remaining authors.

In Nb-containing ternary alloys, fracture was again primarily by cleavage in materials with Widmanstätten structures.[28,124,125] Lukasak and Koss[79] observed that fractures typically initiated near the surface. They observed tear edges from ductile behavior of the β present in the Ti-24-11.

Malakondaiah[124] observed that in Widmanstätten structured Ti-24-11, fracture was by quasicleavage. This was the only reference using this term, which derives from ferrous metallurgy and fracture in martensitic structures. Quasicleavage applies to cleavage planes that are larger than the underlying small scale features of the microstructure.[126] It is quite appropriate in this context, as the α_2 plates and the interface/β phases form a structure that is analogous to martensitic lath structures in steel. Radical changes

in the microstructure result in a transition from quasicleavage to other processes. In a later part of Malakondaiah's[124] work, fracture in laser melted regions and heat affected zones was observed to be by transgranular cleavage.

Mechanisms have been proposed for fracture in the ternary alloys. Lukasak and Koss[79] state that fracture in the Widmanstätten structured materials is by a microcrack initiation and propagation as opposed to microvoid coalescence process, as is typical in non-intermetallic titanium alloys. Chan[127] proposed that microcracking in the α_2 was the result of slip band decohesion.

5.2 Experimental Procedure

Uniaxial tensile tests were performed in each of the three principal planes of the forging to profile the three-dimensional properties and presence of anisotropy throughout the forging. Figure 28 illustrates the location and sample numbering scheme for the tensile specimens. Some compromise was necessary in locating the specimens near the forging center, as this location represents a singularity.

Tests with the tensile axis along the L principal direction were done in two groups, one with samples located within 21 mm from the center of the forging and the other within 7 mm of the 102 mm radius of the forging. Due to restrictions imposed by the necessity of a grip section on the specimens, the gage section of the specimens was centered on the midplane of the forging.

.
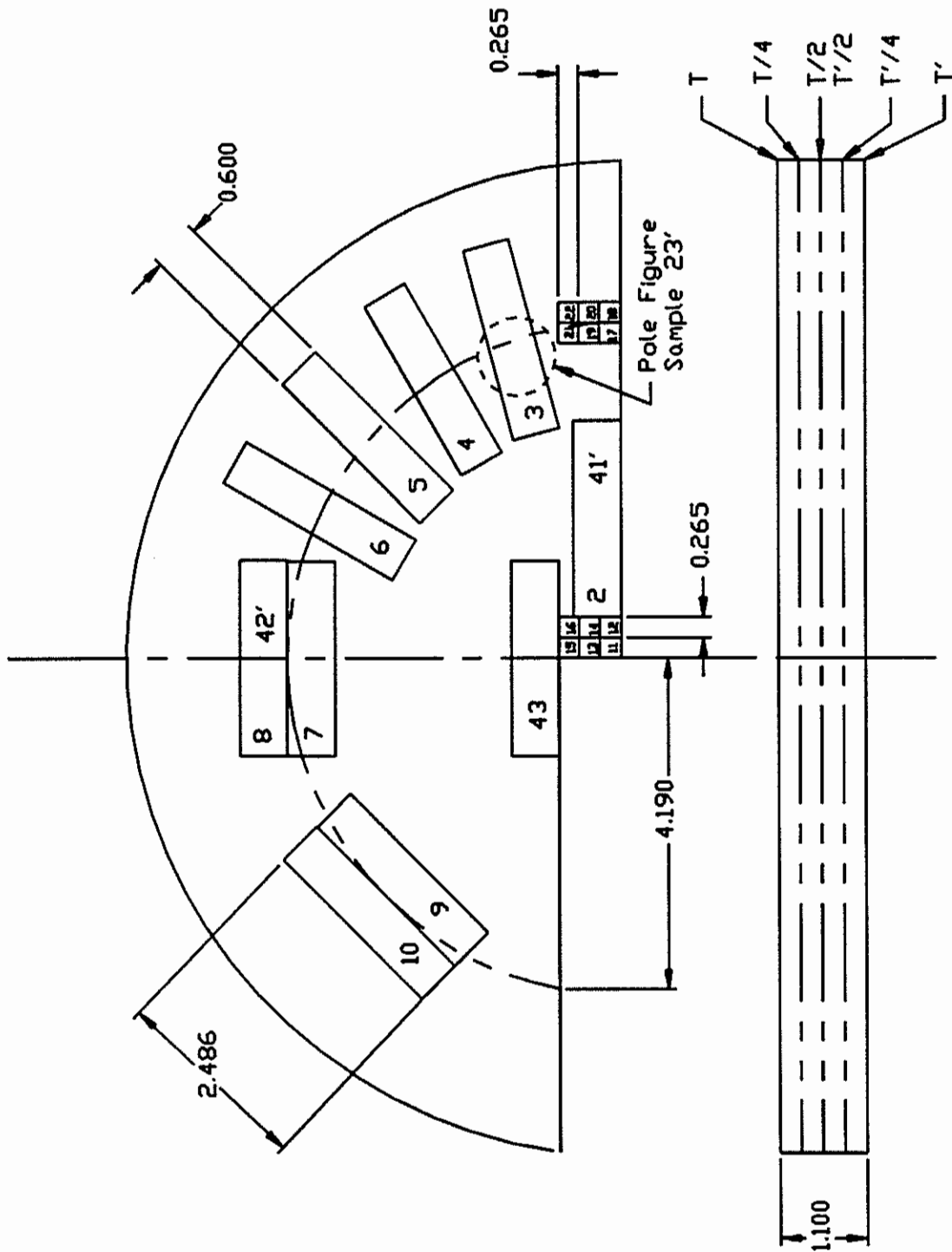
Figure 28

Tensile specimen locations and sample number scheme for the forging.

104

Specimens with the tensile axis along the R principal direction were tested with the gage section centers within 66 mm of the center of the forging and at the 102 mm radius. The tests in the C principle direction were performed similarly at 94 and 109 mm from the center of the forging. These locations were within the cylinder defined by the initial die contact circle (see the metallography chapter). The tensile properties in the C and R orientations were profiled on three CR principal planes, *i.e.*, parallel to the die contact surface at three distances from the top. These locations were identified as being on approximately the half plane (T/2), quarter plane (T/4) and surface plane (T).

Tensile specimens were machined from the forging by the ASCA machine shop in the form of blanks using traveling wire electrical discharge machining (EDM). The final geometries were crush form ground by Joliet Metallurgical (JML).[*] The L orientation blanks were ground into substandard size threaded round bar specimens as illustrated in Figure 29a. The C and R oriented blanks were ground into substandard size pin loaded dog bone specimens as illustrated in Figure 29b. In the case of the dog bone specimens, JML removed 127 - 254 μm from the surface to eliminate the EDM recast layer, which is typical of aerospace industry practice.

Room temperature tensile tests were performed on a universal testing machine by JML per ASTM B 557, except as noted in this section. Clip type extensometry was employed to measure the elongation of the 12.7 mm gage length in the C and R orientated

_____

[*] Joliet Metallurgical Laboratories, Inc., 305 North Republic Ave., Joliet, IL, 60435. Timothy A. Costa, was the cognizant engineer.
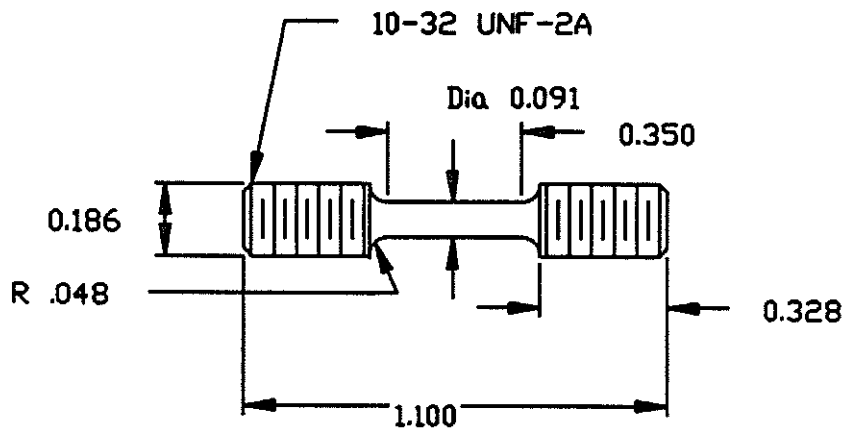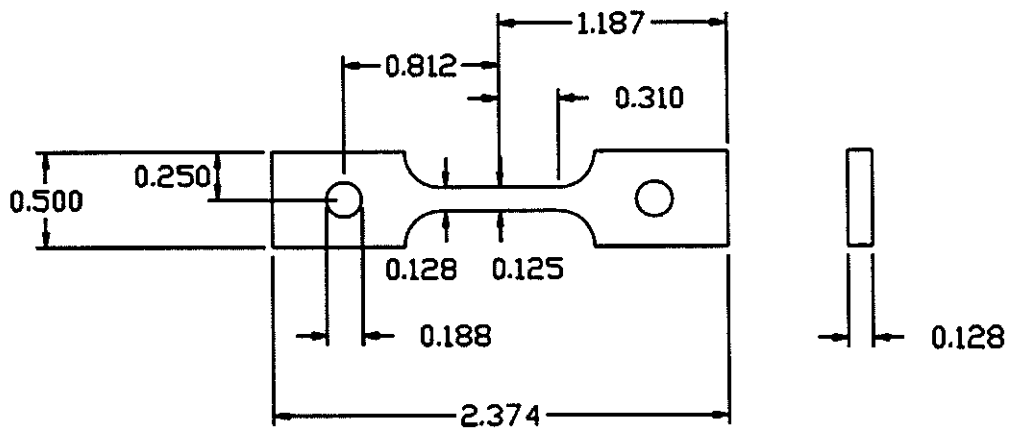
Figure 29
Tensile specimen geometry a. threaded round bar; b. pin loaded dog bone.

samples. Elongation over 25.4 mm was measured in the L oriented specimens using an extensometer mounted on the sample grips. Extensometry remained on the specimens until failure. Tests were done at a substandard strain rate of $ca.$ 550×10^{-6} s^{-1}. Ultimate tensile strength (UTS), 0.2% yield strength (YS) and percent elongation (EL) were determined for all specimens. The UTS was based on the load cell reading rather than on the strip chart record of the load displacement curve. The reduction in area was determined for the L oriented specimens only.

Weibull analysis ($c.f.$ Abernethy, $et.al.$[128]) was used to identify outliers and for design data generation. The maximum likelihood method of Abernethy, as embodied in WeibullSMITH[*] 5.23A software, was employed in the analysis. One way analysis of variance (ANOVA) was used to identify statistically significant differences in tensile properties vs. location in the forging. Sample statistics and ANOVA were performed using Jandel Scientific SigmaStat 1.01 DOS.

Electron-fractography of selected fracture faces was performed using an ISI-60A scanning electron microscope operated in the secondary electron mode. Accelerating voltage was fixed at 30 kv. The samples were first ultrasonically cleaned in acetone. A 0° tilt angle was selected to eliminate distortion of the fracture image scale.

---

[*] WeibullSMITH, Fulton Findings, 1251 W. Sepulveda Blvd. # 800, Torrance, CA 90502.

5.3   Results and Discussion

A total of 51 uniaxial tensile tests were performed. Of these, 5 load pin hole failures, 1 radius failure, 1 damaged specimen and 1 outlying result occurred. Considering the brittle nature of the material, this was a good yield. This section presents the remaining 43 tensile test results, statistical analysis, stress-strain curves and fractographic analysis.

5.3.1   Tensile Results and Statistical Analysis

The results of tensile tests are presented in Tables 5 and 6. The results were segregated based on whether sufficient elastic deformation obtained on the load displacement diagrams for accurate determination of 0.2% offset yield strength.

A Weibull plot of the ultimate tensile strength (UTS) results presented in Tables 5 and 6 is shown in Figure 30. This plot shows clear evidence of at least a bimodal

Table 5

Tensile Results where Yielding was Insignificant

Sample No	Tensile Axis	Location in Forging		UTS (MPa)	% El*
		Radial mm	Axial		
8T	C	109	T	541	0.3
42T/4	C	109	T/4	504	0.4
24T	R	7.6	T	605	0.1
6T	R	102	T	384	0.8
4T	R	102	T	408	0.5
3T	R	102	T	668	0.6
4T/2	R	102	T/2	168	0.3

* 12.7 mm gage length

Table 6

Tensile Test Results where Significant Yielding Occurred

Sample	Tensile Axis	Location in Forging		YS (MPa)	UTS (MPa)	% El*	% RA†
		Radial	Axial				
16	L	0	T/2	878	1014	5.4	6.6
15	L	0	T/2	897	1012	5.1	5.3
14	L	0	T/2	819	969	5.7	10.2
13	L	0	T/2	839	963	4.6	6.8
12	L	0	T/2	870	965	3.4	5.4
11	L	0	T/2	882	1006	4	8.1
22	L	102	T/2	800	892	3.2	3.3
21	L	102	T/2	846	951	3.7	3.3
20	L	102	T/2	837	879	2	3.3
18	L	102	T/2	812	868	2.3	2.2
17	L	102	T/2	879	974	4	4.6
24T/2	R	7.6	T/2	789	916	1.5	
24T/4	R	7.6	T/4	810	1017	4.2	
43T	R	28	T	764	939	2.9	
43T/2	R	128	T/2	788	1009	4	
43T/4	R	128	T/4	760	945	2.5	
2T	R	66	T	695	892	2.1	
41T/2	R	66	T/2	743	872	1.6	
41T/4	R	66	T/4	735	945	2.1	
2T/4	R	66	T/4	732	933	3	
5T	R	102	T	836	996	1.5	
6T/2	R	102	T/2	838	1017	2.4	
5T/2	R	102	T/2	798	955	2	
3T/2	R	102	T/2	739	919	2.2	
5T/4	R	102	T/4	837	994	2.1	
3T/4	R	102	T/4	803	952	2.6	
7T	C	94	T	861	951	1.6	
9T/2	C	94	T/2	746	914	1.8	
7T/2	C	94	T/2	785	926	2.1	
9T/4	C	94	T/4	736	894	1.7	
7T/4	C	94	T/4	819	954	1.9	
42T	C	109	T	802	983	3.1	
10T	C	109	T	787	930	1.7	
42T/2	C	109	T/2	808	914	1.5	
10T/4	C	109	T/4	783	894	1.2	

* 25.4 mm gage length for L tests
  12.7 mm gage length for R & L tests.
† Reduction in Area only measured for round bar specimens.

distribution of UTS results. Inspection of the data revealed the non-monotonic correlation of lowelongation with the low UTS values. The results shown in Table 5, which correspond to both the lowest ductility and the lower strength distribution on the Weibull plot, were thus excluded from further analysis of tensile properties. This was justified on an engineering basis by the fact that proof testing would eliminate these low ductility/low strength cases. Possible causes for the observed low ductility were surface or volumetric defects from specimen preparation or forging manufacturing, respectively. These anomalous failures at low ductility may also be attributed to bending stress during tensile testing.

Ultimate Tensile Strength (MPa)
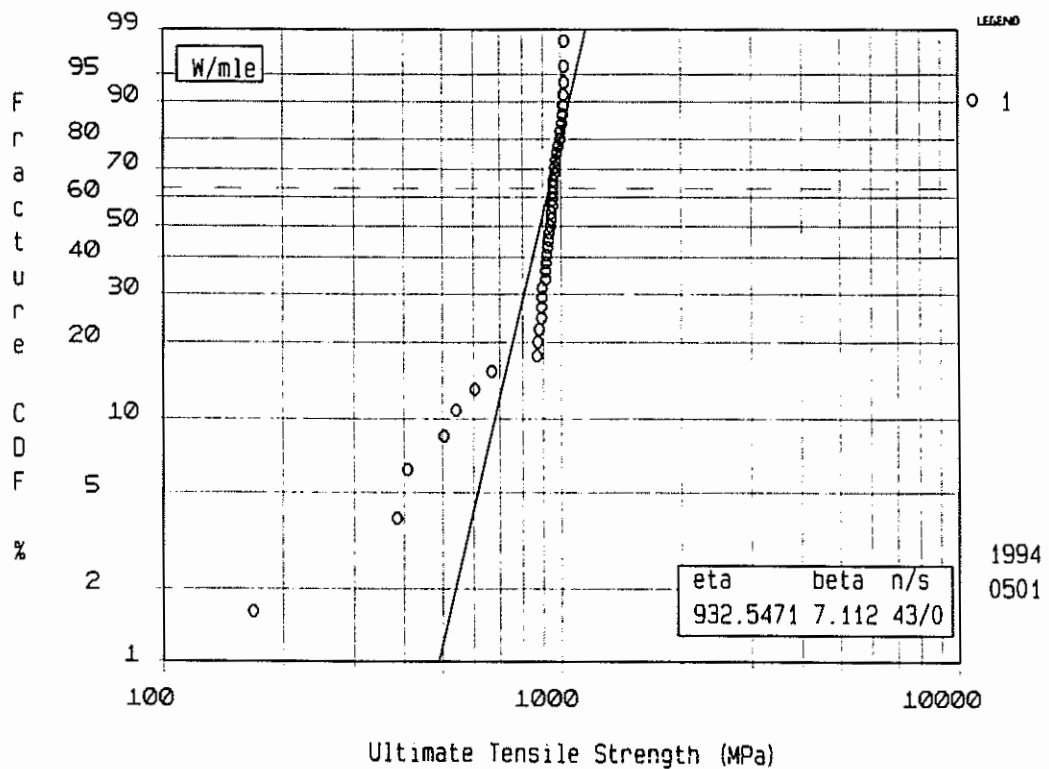
Figure 30
Weibull plot of all tensile UTS data from Tables 5 and 6.

Figure 31 shows the resulting two parameter Weibull plots of UTS and 0.2% offset yield strength (YS) for the censored data set. The upper and lower 95% confidence intervals about the maximum likelihood fit are shown on the plot. The ordinate gives the
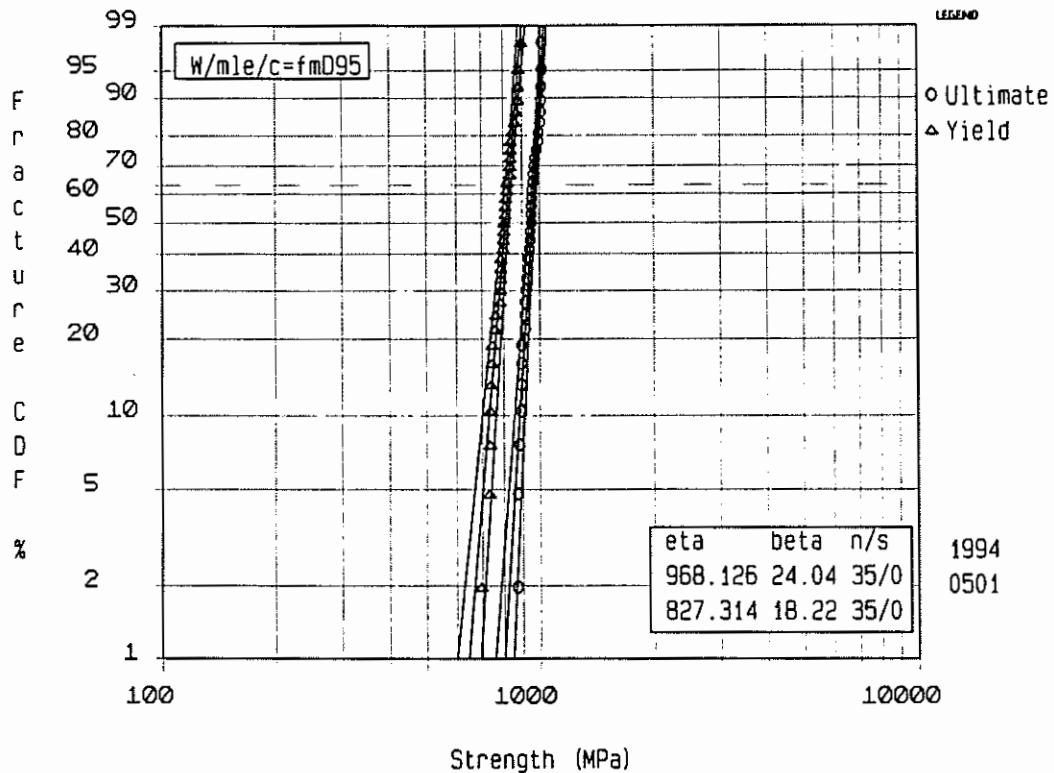
Figure 31
Weibull plot of censored tensile UTS and YS results from Table 6.

probability of fracture or yield at a given stress level. Thus, extrapolation of this curve can be employed in a probabilistic design scheme. The value of "eta" corresponds to the characteristic UTS and YS, respectively. The characteristic strengths are the stresses at which 63.2% probabilities of failure or yielding occur, respectively. In probabilistic design practice, the characteristic strengths are employed, as opposed to average strengths. The values of "beta," also know as the Weibull modulli, are the slopes of the

111

respective maximum likelihood curve fits. The values of β and η define the line along which a probabilistic design is based.

A significant advantage of Weibull statistics is that a particular form to the distribution is not assumed, *e.g.*, normal, chi-square, log normal, etc. Values of $\beta = 1$ and 3.4 were evidence of exponential and normal distributions, respectively, with the former indicating operation of random failure modes.[128] The values of β given on the Weibull plot: $\beta = 24.04$ and 18.22 for UTS and YS, respectively, were measures of scatter in the strength distributions. The lower value of β for YS implied slightly greater scatter in this sample. Qualitatively, the values of β obtaining for UTS and YS corresponded to overload type failure. From an engineering design standpoint, however, the Weibull slopes were not great enough to justify the application of standard deterministic design approaches common to metals. Rather, a probabilistic approach more in line with ceramic materials was indicated.

Insufficient data were available to resolve significant differences in UTS or YS vs. sample location using Weibull statistics. One way ANOVA, Students t-tests, and Mann-Whitney rank sum tests were performed to assess any possible crystallographic texture effects on YS in particular or on UTS. The ANOVA is intended to assess differences between three or more groups. The Students t-test and Mann-Whitney rank sum tests are intended for assessing statistically significant differences between 2 groups. The Mann-Whitney test is employed when either the assumption of normal distribution or equal variance is violated when attempting to apply the t-test. These tests were

performed with a level of significance $\alpha = 0.05$. The α is the probability of falsely rejecting the null hypothesis. The significance test results are presented in Table 7.

The results of the statistical analysis of UTS data did not show any statistically significant differences with regard to location in the forging. This was not entirely surprising, as UTS of a polycrystal is not typically affected by texture.

The analysis of YS data was less straightforward. As shown in Table 7, significant differences were observed in YS measurements, with regard to location in the forging. Statistically significant differences were observed in two of the test cases of the YS. The relevant groups showing statistically significant variation were identified by the Student-Newman-Keuls multiple comparison method. The results of this analysis are presented in Table 8 in decreasing level of significance. These differences obtained for the significance analyses which considered the entire spatial distribution of specimens and the tensile axis orientation to be independent, and also in the analysis where only the tensile axis orientation was assumed to be independent. In the latter case, data from all spatial positions were lumped based on tensile axis orientation. The table is an abbreviated multiple comparison table, showing only those cases where significant differences were indicated.

Statistically significant differences were all relative to the L oriented tensile tests. The L oriented specimens were of round bar as opposed to the rectangular cross section dog bone geometry employed for the C and R tensile axis orientations. The L oriented specimens had the highest YS, being 865 MPa at the center of the forging, and 835 MPa

Table 7

Significance Test Results for Variation of Tensile Properties with Position and Tensile Axis Location in the Forging

Independent Factors			Significance ($P < \alpha = 0.05$)			
Tensile Axis (L, R, C)	Radial Position (c, o)§	Axial Position (T, T/4, T/2)	YS	P	UTS	P
✓	✓	✓	Yes	< 0.001	No	0.09
✓			Yes	< 0.001	No	0.433
	✓		No[†]	0.701	No[‡]	0.155
		✓*	No	0.873	No	0.853

* Exclusive of L axis tensile tests due to no control of the fracture plane within the gage section..
† Mann-Whitney rank sum test (only two groups with unequal variance were compared).
‡ Students t-test (only two groups were compared).
§ Forging center (c) and outside (o).

Table 8

Statistically Significant Yield Strength Variations in the Forging

Independent Factors			Significantly Different Groups ($P < \alpha = 0.05$)	
Tensile Axis Orientation (R, L, C)	Radial Position (c, o)	Axial Position (T, T/4, T/2)		Δ Mean[†]
✓	✓	✓	(L, c,) vs. (R, c, T) *	-134. MPa
			(L, c,) vs. (R, c, T/4)	-105.
			(L, c,) vs. (R, c, T/2)	-91.
			(L, c,) vs. (C, o, T/2)	-84.
			(L, c,) vs. (C, o, T/4)	-84.
✓			L vs. R	-73.
			L vs. C	-59.

* Orientation code: (tensile axis orientation, radial location, axial location) c: center; o: outside
† Yield strength relative to (L,c,) = 864 MPa or L = 851 MPa, respectively.

at the 102 mm radius. These differences may be attributable to either texturing along the longitudinal axis of the forging, or to a sample geometry effect. If texturing were the cause, then it is surprising that statistically significant differences in YS were not observed between other positions and tensile axis orientations in the forging.

The issue of tensile specimen shape deserves further comment. Due to sample size restrictions, it was necessary to make the unfortunate decision to have multiple sample geometries. The cross sectional areas of the round bar and dog bone specimens were 4.19 mm^2 and 10.8 mm^2, respectively. Given a prior β grain size of ASTM M9.4, this corresponds to an average projected area for each prior β grain of 1.8 mm^2. Thus, the round bar and dog bone specimens contained on average 2.2 and 5.6 prior β grains across the cross section, respectively.

Although each prior β grain contains many α_2 plates, making each specimen most definitely polycrystalline, the round bar specimens were in effect highly micro-textured. From quantitative optical image analysis presented in the metallography chapter, each prior β grain potentially contained less than the 12 possible independent α_2 variants. Thus, minimal independent α_2 orientation variants were present in the round bar specimens compared to the dog bone specimens. It is the random orientation of grains in a polycrystalline material which gives rise to the Von Mises requirement of 5 independent slip systems for general plasticity. In the absence of these independent slip systems, strain incompatibilities at grain boundaries result in crack initiation. With the effectively highly microtextured round bar specimen, by virtue of its small cross sectional area, it

115

was possible that the higher YS was the result of incomplete constraint of α_2 plates necessary to minimize plasticity to the extent observed in the dog bone specimens, where more α_2 plate orientations were present. This notion is supported by the significantly* greater elongation observed for the L orientation (median %EL = 4%) specimens compared to the R and C orientations (median %EL = 2%). However, the 25.4 mm vs. 12.7 mm gage lengths employed for the L vs. R and C tensile axis oriented specimens, respectively would contradict the observed differences in elongation. Use of shorter gage length for equivalent specimens would be expected to give greater elongation due to strain concentration in the neck region, while the opposite was observed. However, since no appreciable necking occurred, differences in gage length should have little effect on reported elongation.

In summary, from the tensile results, evidently significant texturing was not present in the forging. For design purposes, the characteristic UTS and YS as given in Figure 31 should be employed with the Weibull modulli in a probabilistic method, which assumes isotropic tensile properties. The material should be treated as brittle in design, as the ductility was typically less than 5%.

---

* Based on a Mann-Whitney rank sum test with α = 0.05, due to the failure of equal variance required for a t-test.
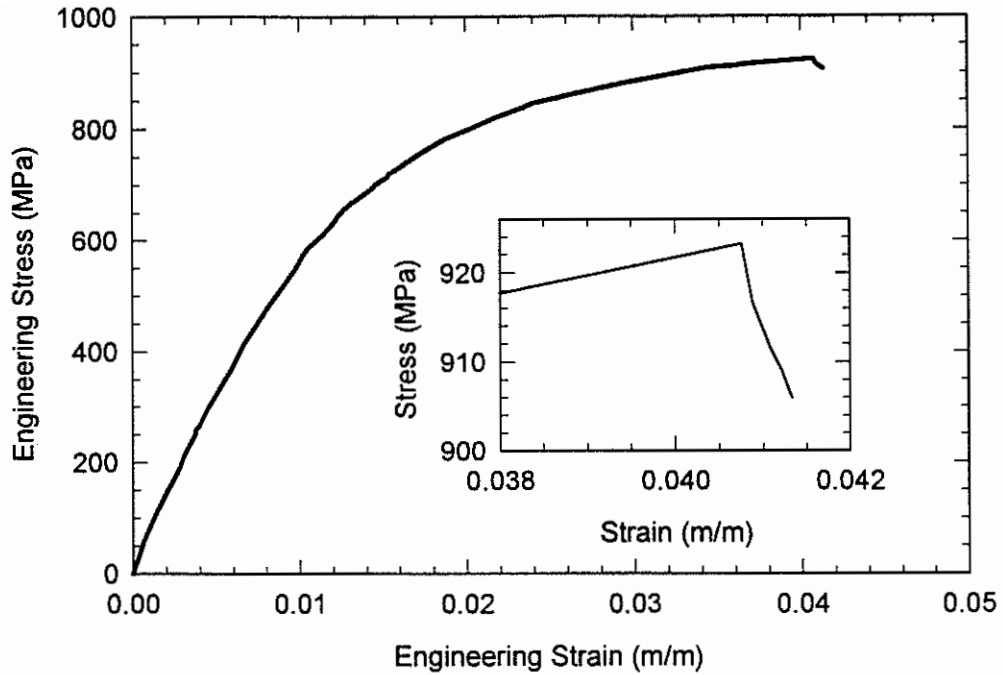
Figure 32

Engineering stress vs. engineering strain curve for sample 7T/2.

5.3.2   Stress Strain Curves

A typical engineering stress vs. engineering strain curve is shown in Figure 32. This curve was generated from the digitized load displacement curve, where the extensometer remained on the specimen through failure. Of particular interest was the abrupt engineering stress reduction after reaching the UTS. The inset to Figure 32 shows

this point more clearly. For brittle fracture, the extent of plasticity shown in this sample would not be expected. Conversely, for ductile behavior, the onset of necking would cause a smooth reduction in engineering stress after reaching the UTS. This sample essentially experienced uniform deformation to the point of complete fracture. Features

117

of this type were noted on most load-displacement curves. The amount of post UTS strain was greatest for the L oriented specimens. Ward[64] shows similar features to that in Figure 32 on stress strain curves for Ti-25-10-3-1 processed both within the $\alpha_2 + \beta$ and βregions.he only exception in his study was the microstructure which most closely* approximated that observed in this work.

The alloy contains at least two phases, of which α_2 is the least ductile. As is discussed in the fractography section, secondary transgranular cracking was observed relative to prior β grains (Figure 37). Thus, the UTS may represent the onset of general cracking. The point of complete fracture would then represent failure of the β matrix phase. In Ward's[64] work, acoustic emission revealed that most of the micro-cracking was associated with the terminal region of the stress strain curve, thus providing support for this argument. He concluded that fracture in Ti-25-10-3-1 was crack initiation controlled.

5.3.3 Fractography

The objective of fractographic investigation was to observe any textural influences on the fracture morphology and to observe any correlation of ductility with fracture features. To the former end, a subset of samples showing significant yield strength differences, as given in Table 8, was analyzed. For the latter purpose, samples from a given location showing extremes of ductility were analyzed.

---

*   Ward[64] did not investigate material processed in the $\alpha_2 + \beta$ region and subsequently annealed in the β region. The closest schedule in his work was β processing and annealing.

In general, the appearance of fracture faces was as indicated in the background section. Fracture was primarily by brittle transgranular quasi-cleavage, relative to the prior β grains. Secondary cracking was evident. Neither a fibrous zone nor shear lips were observed. However, isolated dimpling was observed. Fracture origins were evident as the origins of river marks. Table 9 presents a summary of these observations, showing both the ductility and sample location in the forging. The details of these observations follow.

Table 9

Fracture Feature Summary

Sample	Tensile Axis	Location in Forging		% El	Fracture Features				
		Radial	Axial		River	Origin	Cracks	Cleavage	Dimples
L11	L	0		4.0	✓	o.d.	✓	✓	
L12	L	0		3.4	✓	o.d.		✓	
L14	L	0		5.7	✓	o.d.		✓	
L17	L	102		4.0	✓	o.d.	✓	✓	
L20	L	102		2.0	✓	o.d.	✓	✓	✓
3T/4	R	102	T/4	2.6	✓	o.d.	✓	✓	✓
4T/2	R	102	T/2	0.3	✓	inside	✓	✓	
6T/2	R	102	T/2	2.4	✓	o.d.	✓	✓	✓
4T	R	102	T	0.5	✓	o.d.	✓	✓	✓
5T	R	102	T	1.5	✓	multiple	✓	✓	

As indicated in Table 9, river marks pointed to the fracture origin in all cases. Although the clarity of the river markings changed from sample to sample, their presence was not affected by changes in ductility or location in the forging. Figure 33 shows a typical river mark pointing to a surface type failure origin. Failures of this type may be

119
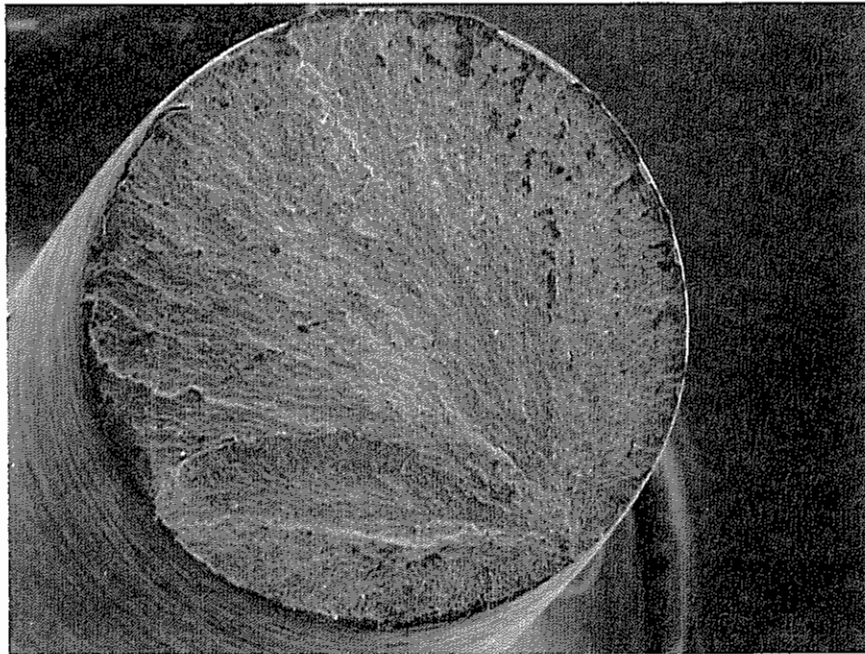
Figure 33
River markings indicate a surface originated fracture.
Sample L-14.

the result of either machining induced surface damage, or the presence of a bending moment in the test specimen, both of which are common explanations. Low stress crush form grinding was employed to minimize the former effect.

The distinction as to whether the fractures are classified as cleavage or quasi-cleavage is dependent on the frame of reference. Malakondaiah and Nicholas[124] described a similar fracture face to that shown in Figure 34 as quasi-cleavage. Relative to the prior β grain, this is an appropriate description of the fractures observed here. That is, the facets observed are large compared to the α_2 plate thickness and appear to represent cleavage of the β grain, with some of the evidence of plasticity which characterizes quasi-cleavage. However, an inspection of other samples revealed what appears to be actual

120

50 µm
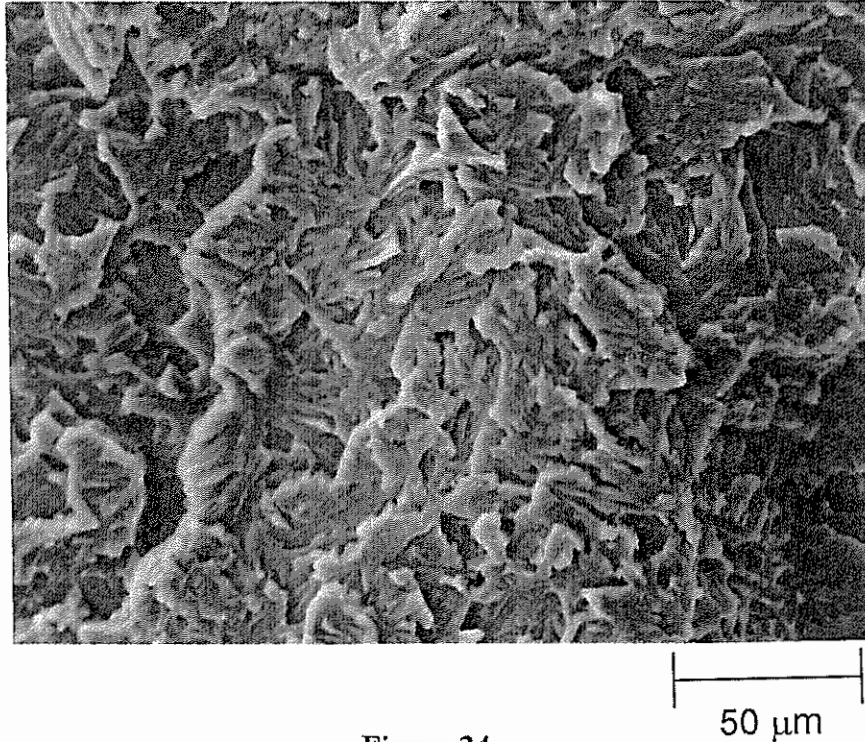
Figure 34
Quasi-cleavage in sample 4T/2.

cleavage of α_2 plates as shown at the lower left of center in Figure 35. On this basis, it would be most proper to describe the fracture as cleavage of α_2, with tearing of the surrounding β phase.

The sample shown in Figure 34 had a ductility of 0.3%, whereas the sample in Figure 35 had a ductility of 2.6%. It was not possible to correlate the appearance of the fracture face with the ductility of the material. Indeed, Figure 37 displayed greater tearing of the ductile β phase than was evident in the more ductile case of Figure 34.

Figure 37 again illustrates the appearance of quasi-cleavage, however, now it is in the presence of significant cracking. As given in Table 9, cracking was observed in both high and low ductility fractures. Figure 37 also shows the presence of two prior β
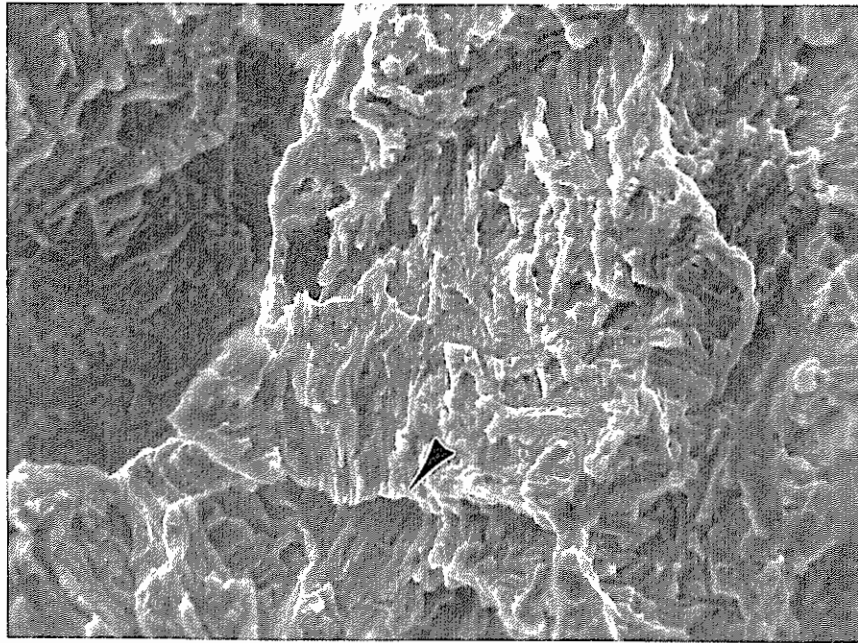
Figure 35
Actual cleavage of α_2 plates in sample 3T/4.

50 μm

grain boundaries in the upper right hand quadrant of the fractograph. The prior β grain

boundaries were evident from the parallel colonies of aligned α_2 plates. The crack did not

appear to follow these grain boundaries. On higher magnification of the crack in Figure

37, the appearance of quasi-cleavage again gave way to the appearance of cleavage of α_2

and tearing of the β phase.

Dimpling, which is evidence of ductile fracture, was observed in isolated areas

of both high and low ductility samples. Figure 36 shows dimpling of a sample with 2.4%

ductility. The dimpled material appears to be surrounding an α_2 plate. From this case and

the other isolated observations of dimpling, the geometry of the dimpled regions appears

not to be associated with the geometry of an α_2 plate. Thus, the appearance of ductility
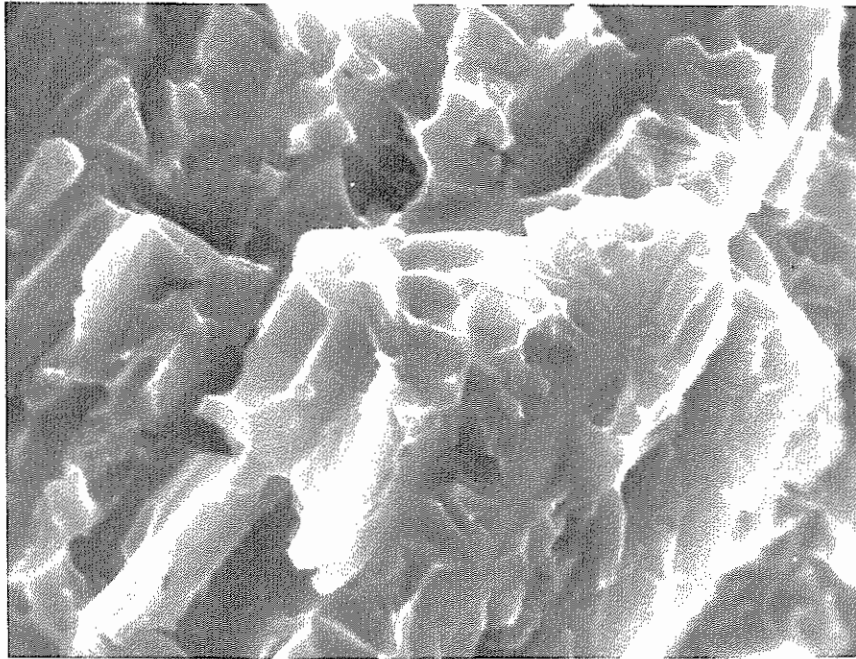
Figure 36
Dimpling of sample 6T/2.

10 μm

in the fracture faces is ascribable to the β phase as also noted by Ward,[64] as opposed to

favorably oriented α_2 as discussed by Marquardt, *et.al.*[119]

In the presence of crystallographic texture, in addition to changes in ductility,

fracture features such as dimpling would be expected to vary with texture, *i.e.*, the extent

of brittle fracture features observed should correlate with ductility. Considering that most

fracture features were observed in samples with both low and high ductility and in both

L and R tensile axis orientations, no fractographic evidence of texture exists. The

resolution of fracture morphology to indicate differences in processing conditions,

orientation and composition is well founded in historical mill practice, where the

appearance of fracture faces provided a means of process and quality control.

123

a

250 μm

b
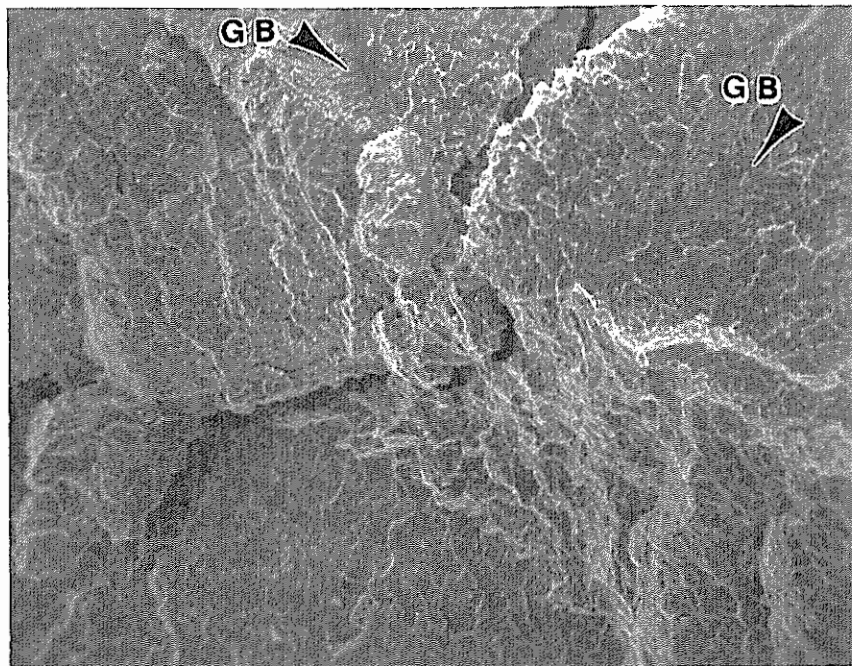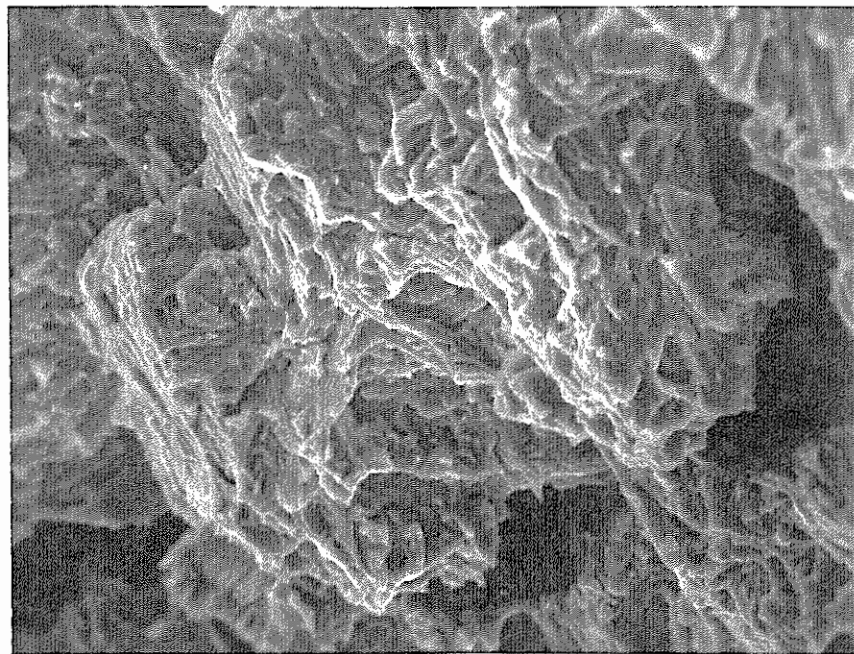
50 μm

Figure 37
Transgranular cracking in sample 4T/2.

124

CHAPTER 6

CRYSTALLOGRAPHIC TEXTURE

This chapter is concerned with x-ray analysis of texture in the Ti-25-10-3-1 isothermal forging. While nearly all experimental techniques employed in this research are sensitive to texture, x-ray methods offered the potential to reveal the most quantitative information. After a review of texture studies in Titanium alloys, the results focus on lack of significant texture in the forging and possible explanations based on superplastic deformation, and the effects of recrystallization during the β anneal.

6.1 Background

The most significant body of information on the texture of titanium alloys is based on the industry standard Ti-6-4. Most of this work focuses on sheet and foil. Only minimal information is available on isothermal forgings, or intermetallic titanium alloys. The following reviews this work as it relates to the intermetallic alloy Ti-25-10-3-1, again relying on the similarity of $\alpha + \beta$ and $\alpha_2 + \beta$ alloy behavior. This assumption of similarity is especially appropriate for the hot working operations, where the effects of ordering are of minimal significance.

The importance of texture in titanium alloys cannot be over emphasized. The hexagonal structure of the α and α_2 phases inherently leads to mechanical property anisotropy. For example, in Ti-6-4 sheet, longitudinal tensile yield strengths and ultimate strengths significantly lag the transverse oriented properties, giving rise to strength differences of 140 MPa and 100 MPa for yield and ultimate strength, respectively.[129] McDarmaid, *et.al.*[130] observed similar effects. Lütjering *et.al.*[131] showed that texture in Ti-6Al-4V, can be responsible for a constant 100 MPa increase in fatigue strength, independent of cycle count.

Inagaki[132] performed a thorough investigation of the texture in Ti-6-4 following hot rolling both below and above the β transus. Many of his observations parallel those in this work. In general, significant texture did not develop until at least 75% rolling reduction was obtained. The extent of texturing was evident in optical micrographs of the Widmanstätten α structure. Inagaki[132] emphasized the need for a more thorough description of texture than the typical plane and direction of maximum orientation, obtaining from one pole figure, based on the low symmetry of the HCP α phase. He employed crystallographic orientation distribution functions (CODF) to this end. The CODF essentially provides a three-dimensional map of the orientation of every crystallite in the sample material. From the CODF, he found that the predominant α phase rolling texture component in sub-transus processed material was $(\bar{2}111)[0\bar{1}10]$. In super-transus processed material, β to α transformation textures were observed: $(\bar{1}010)[0001]$ and $(\bar{2}110)[0\bar{1}10]$. These textures in the β processed material followed from the observed

126

rolling elongation of the prior β grains. He noted the difficulty of obtaining texture data from the β processed material, where prior β grain sizes were large. This issue is discussed in greater detail in the results section. Of all the texture studies reported here, the ones using the CODF provided the best description. The CODF can quantitatively show the extent of deviation from perfect fiber or sheet textures which were assumed by the other investigators.

Hon, *et.al.*,[125] identified a possible strong basal texture in the rolling direction (RD) following hot rolling and $\alpha_2 + \beta$ annealing of Ti-24-10. This initial work was based on peak height differences in the XRD pattern for the material in the as-rolled vs. powdered and annealed form. Their material showed elongation of α_2 plates in the RD after rolling. Annealing of the material developed an equiaxed α_2 structure. Sukonnik, *et.al.*[133] confirmed, using pole figures, the strong basal texture following cold rolling of Ti-24-11.

Verma and Ghosh[134] observed a bimodal texture following hot rolling of β forged Ti-24-11. The consensus of $\{11\bar{2}0\}$, $\{10\bar{1}0\}$, $\{11\bar{2}1\}$ and $\{0001\}$ α_2 pole figures revealed idealized $\{11\bar{2}0\}<5\bar{4}\bar{1}0>$ prism and $(0001)<11\bar{2}0>$ basal texture. This was a case where the CODF would have been useful, as the assignment of these idealized textures required many assumptions. It was not clear why a CODF was not generated, as the authors had sufficient pole figure data. From $\alpha_2 + \beta$ swaging trials, Kumpfert, *et.al.*,[135] observed <211> fiber texture in Ti-25Al-10Nb-3V-1Mo. No details of the texture measurement

127

method were provided. Again, a CODF would help significantly with interpretation, however, additional pole figure experiments would probably have had to be done.

Minimal work has been advanced on the texture of β Ti. This is the result of both typically large prior β grain size, and minimal phase fraction at room temperature. While Humbert, et.al.[136] have developed a novel approach to determination of β textures by electron back scatter microtexture measurements on α in Ta-Al, the method has not yet been employed for Ti alloys. Bowen, et.al.[137] found a <110> fiber texture of the β phase in Ti-6-4, following sub-β transus non-superplastic rolling. In superplastic rolling, texture intensity decreased significantly. They state that this texture should enhance <0001> fiber texture of α on transformation from β. They note that α variant selection would complicate the development of a perfect [0001] fiber texture.

Limited information on transformation texture, i.e., texture of α_2 after transformation from β, was available. In an investigation of CP Ti, Zhu, et.al.[138] observed that transformation from β can suppress textures from prior α processing. Besides the work of Inagaki,[132] previously reviewed in this section, Bowen, et.al.[137] emphasize the need to consider transformation texture, as most of the deformation occurs in the β phase on hot working both above and below the β transus. Superplastic deformation has been shown to significantly affect texture in Ti and many other alloys. Cutler and Edington[139] showed that textured eutectic Sn-Pb sheet experienced a reduction in texture through subsequent superplastic deformation. This effect was attributed to either grain boundary sliding during superplastic deformation or inhomogeneous strain accommodation at grain/phase

boundaries, both of which can give rise to random rotation of the grains, thus reducing texture. Further investigation by Melton, Edington, et.al.[140] on Zn-Al, showed for the first time that slip can occur during superplastic deformation. The incidence of slip or diffusional creep makes possible the stabilization of texture. Thus, the superplastic deformation process represents a tradeoff between texture increasing and texture decreasing factors. The extent of texture reduction varied with decreasing strain-rate, i.e., increasing superplastic behavior. Further work employing CODF's showed conclusively that slip can be operational during superplastic deformation.[141] Reduced crystallographic texture has also been noted in single phase alloy sheets deformed superplastically.[142]

Although texture reduction attributable to superplastic deformation has not been observed explicitly in intermetallic titanium alloys, it has been observed in Ti-6-4. McDarmaid, et.al.[130] observed that while a "basal edge texture" ($(0001)<11\bar{2}0>$) remained strong, other strong poles were reduced in intensity following superplastic deformation. Note that the pole figures were generated from samples cut perpendicular to the RD. Room temperature mechanical properties were less anisotropic following superplastic deformation and the attendant texture reduction. Bowen, et.al.[137] addressed texture in β Ti-6-4 following superplastic deformation below the β transus. They observed that texture of β decreased with superplastic deformation, and point out that the texture of α precipitated in the prior β grains would also show reduced texture by virtue of the Burgers relationship. They also found that the majority of plasticity at the working temperature

was located in the β phase. In earlier work, they showed that microstructural alignment of α was reduced during superplastic deformation.[143]

6.2   Experimental Procedure

Samples for x-ray pole figure determination were electrical discharge machined from the forging. Surface grinding was not used to remove recast as it had the potential to impart textural artifacts at the surface. The 22.5 mm diameter samples were cut from the T, T/4 and T/2 RC principal planes, *i.e.*, parallel to the flat surface of the forging, centered at 33 mm (sample 26) and 102 mm (sample 23) from the center of the forging. The specimen thickness was 2.54 mm. Notches in the edge of the specimens indicated the "RD" orientation, which was arbitrarily chosen to point radially.

The specimens were mounted in Bakelite for preparation of the analysis surfaces. Specimens were ground using 320, 400 and 600 grit SiC paper to remove the EDM recast surface. The specimens were subsequently polished using a sequence of 6 μm diamond, 1, 0.3 and 0.05 μm Al_2O_3. Finally, macro-etching was performed by immersion and swabbing for 60 s in 10%HF + 45%HNO$_3$ + 45%H$_2$O (vol. %).[76] Extensive etching was performed to remove the work hardened surface. This etching procedure revealed the prior β grain boundaries clearly. However, the Widmanstätten α_2 structure was not clearly resolved. The specimens were removed from the Bakelite mounts before pole figure analysis.

130

For crystallographic orientation distribution function (CODF) generation, it is necessary to have a minimum of 3 pole figures from the α_2 phase. Selection of crystallographic planes for pole figure determination was complicated by the presence of multiple phases in the forging. It was desirable to use the basal, pyramidal and prismatic planes for pole figures. However, pyramidal plane could not be used due to convolution with the (300) α_2 peak. Similarly, the basal refection could not be used due to convolution with the (110) β peak. The α_2 peaks ultimately chosen for pole figure measurements were as given in Table 10. The relevant diffraction angles were as measured by Lambda Research, as they were the source for the pole figure data.

Pole figure measurements were performed by Lambda Research, Inc. The stepper motor driven Schultz back-reflection[144] pole figure device was mounted on a General Electric horizontal goniometer. Diffraction intensities were measured for 1 s at points spatially separated by *ca.* 4°. Table 10 gives the maximum ϕ (tilt) angle. The azimuth ψ angle was swept over 360°. A 5 mm oscillation in the plane of the specimen surface

Table 10

α_2 Reflections for Pole Figure Measurement

Diffraction Plane	Bragg Angle (°2θ)*	Maximum °ϕ
(101)	26.03	80
(200)	35.94	72
(210)	46.59	80

* $\lambda = 0.154178$ nm

was imposed to increase the effective number of grains from which diffraction could occur.

Background and defocusing corrections are required prior to interpretation of the pole figure data. Background intensity correction was performed by interpolating the intensity on either side of the diffraction peak to the 2θ corresponding to maximum intensity, for each angle ϕ. The maximum ϕ for back reflection was found by Schultz[144] to be limited to 80°. At greater tilt angles, accounting for defocusing effects becomes impossible. Defocusing correction is required at angles of $\phi > 40° - 50°$.[145] The correction is best obtained by measuring the integrated intensity from a texture free sample of the same or similar material at the angles of ϕ chosen for pole figure measurement, and subsequently correcting the integrated intensities from the textured samples proportionaly.[103]

Planar flow cast (rapidly solidified) Ti-25-10-3-1 was employed for the defocusing correction standard. The rapidly solidified powder had been subsequently canned in Fe and hot isostatically pressed to achieve densification. The analysis surface of the standard was normal to the can axis. This sample was polished to the 0.3 µm level, and etched identically to the forging test samples. After etching, flow lines were observed in the standard. However, these were attributed to prior particle boundaries, based on experience of the author with similarly processed materials. The standard, taken from the bottom of the can, had not been cold worked, and as such, was assumed to be texture free. This was verified by Lambda Research. The defocusing correction for the (210) pole

figure was performed based on a Cu random sample, due to insufficient diffracted intensity from the rapidly solidified sample. As shown in Table 10 the tilt was limited to 72° for the (101) pole figures. This was an experimental necessity to eliminate negative intensities after defocusing correction for $\phi > 72°$.

The pole figure results were provided by Lambda Research in stereographic plots, generated using a proprietary contour generation program. The data were also provided in a Fortran format controlled ASCII data structure as described by Kallend, *et.al.*[146] for use in CODF analysis. In this data structure, intensity data were recorded on 5° increments of ψ and ϕ. CODF analysis and additional pole figures were generated by the author using the Los Alamos National Laboratory developed popLA texture analysis software.[146]

6.3   Pole Figure Results & Discussion

Pole figure analyses were performed to quantify the degree of α_2 texture in the forging. Unfortunately, the pole figures revealed little quantitative information regarding the texture in the Ti-25-10-3-2 isothermal forging. Qualitatively, however, the lack of significant texture in the pole figure results was self-consistent with the results of other parts of this project.

As indicated in the Experimental Procedure Section, pole figures were corrected for defocusing error using a rapidly solidified, canned, and HIP'ed sample of the same alloy. This sample showed a maximum times normal intensity of 2.04 in the (200) orientation, while most areas did not exceed 1.5 times normal. This sample was unusable

for the (210) pole figures, as the diffracted intensity was too weak. A Cu texture free standard was employed in its stead for the (210) pole figure correction.

The pole figure data files were processed by popLA using the ROTATE program to account for sample misalignment. The rotate program maximizes the orthotropic sample symmetry through a rotation of the pole figure followed by renormalization of the data. The pole figures at this stage of analysis are presented in Figures 38-43 as output by the popLA POD program. The gray scale indicates times normal intensity, as opposed to times random, as the samples were multiphase. This distinction is based on the fact that a multiphase material will not exhibit a true random orientation. At first, these pole figures appeared to be significantly textured. However, note that the high times normal poles were often isolated and disjoint. The only exceptions were in the (210) pole figures, where high intensities were typically observed near the center of the stereographic projections. However, lacking any corroborating texture in the other pole figures, *i.e.,* (200), it is hard to attribute the observed high times normal region to a real texture element.

Both the author and Lambda Research generated CODF's from the pole figure data. Lambda Research employed a spherical harmonic analysis employing the popLA HEXAN2 code, with imposition or four fold sample symmetry. The author used the WIMV[147] analysis as embodied in the popLA BWIMV code, with imposed orthorhombic sample symmetry. An important feature of the CODF is the ability to calculate pole figures for planes not actually investigated with x-rays. In this way, recalculation of the

134

input pole figure is a test of the validity of the CODF calculation. In both cases, the recalculated pole figures bore no significant resemblance to the input pole figures.

In discussion with Lambda Research, the lack of correlation of raw and calculated pole figures was possibly attributed to the presence of isolated high intensity regions, deriving from a large grain effect. The large grain effect was established in the XRD Results section. No information was available on the sampling area employed at Lambda Research. Intensity histograms were generated from the raw popLA formatted pole figure data files. These histograms are presented alongside the pole figures in Figures 38-43. The histograms revealed that the majority of the pole figure intensity data points were low intensity. The clustering of the intensities corresponds to minimal texture. However, isolated points of high intensity were always observed. In the majority of cases, breaks in the histograms were observed between the high and low intensity regions. These high intensity points were atributed to isolated prior β grains orriented for opportune reflection

Klenk[148] developed a method of quantifying pole figures in single phase materials which assumed operation of a random and variable preferred orientation processes. While this was a multiphase material, the notion of a random component of texture was considered a possible means of extracting useful texture data from the results. If it is assumed that the random component is attributable to the spurious high intensity data points, then a low pass digital filter should enhance any underlying low intensity variable texture. The author wrote a Pascal program to delete data points with intensities in excess a user specified threshold. In their place, the averages of the nearest neighbor intensities

135

were inserted. While this treatment resulted in substantially sharper pole figures, recalculated pole figures following analysis with BWIMV did not resemble the censored data set. Thus, the censoring approach was invalid.

Pole figures were thus incapable of showing the presence of significant texture in the material. However, attributing the isolated high intensity points to favorably oriented α_2 plates relative to the x-ray beam, the remaining points only displayed a maximum times normal intensity of about 5. Thus any texture if present was small, based on the limited number of effective grains analyzed. It was hoped that the CODF would have supported generation of pole figures for other crystallographic planes such as (0002) which may have shown significant texture, and thus would have allowed comparison to the literature. The operation of superplastic deformation during forging, as discussed in the thermo-mechanical processing chapter, is a plausible explanation for the low texture observed in the material. Superplastically deformed materials show a reduction in texture through the randomizing effect of grain boundary sliding. In contrast, slip processes lead to texture enhancement.

Figure 38
Pole figures and intensity distribution histograms for sample 23T'.

137

Figure 39
Pole figures and intensity distribution histograms for sample 23T'/4.

138

Figure 40
Pole figures and intensity distribution histograms for sample 23T'/2.

139
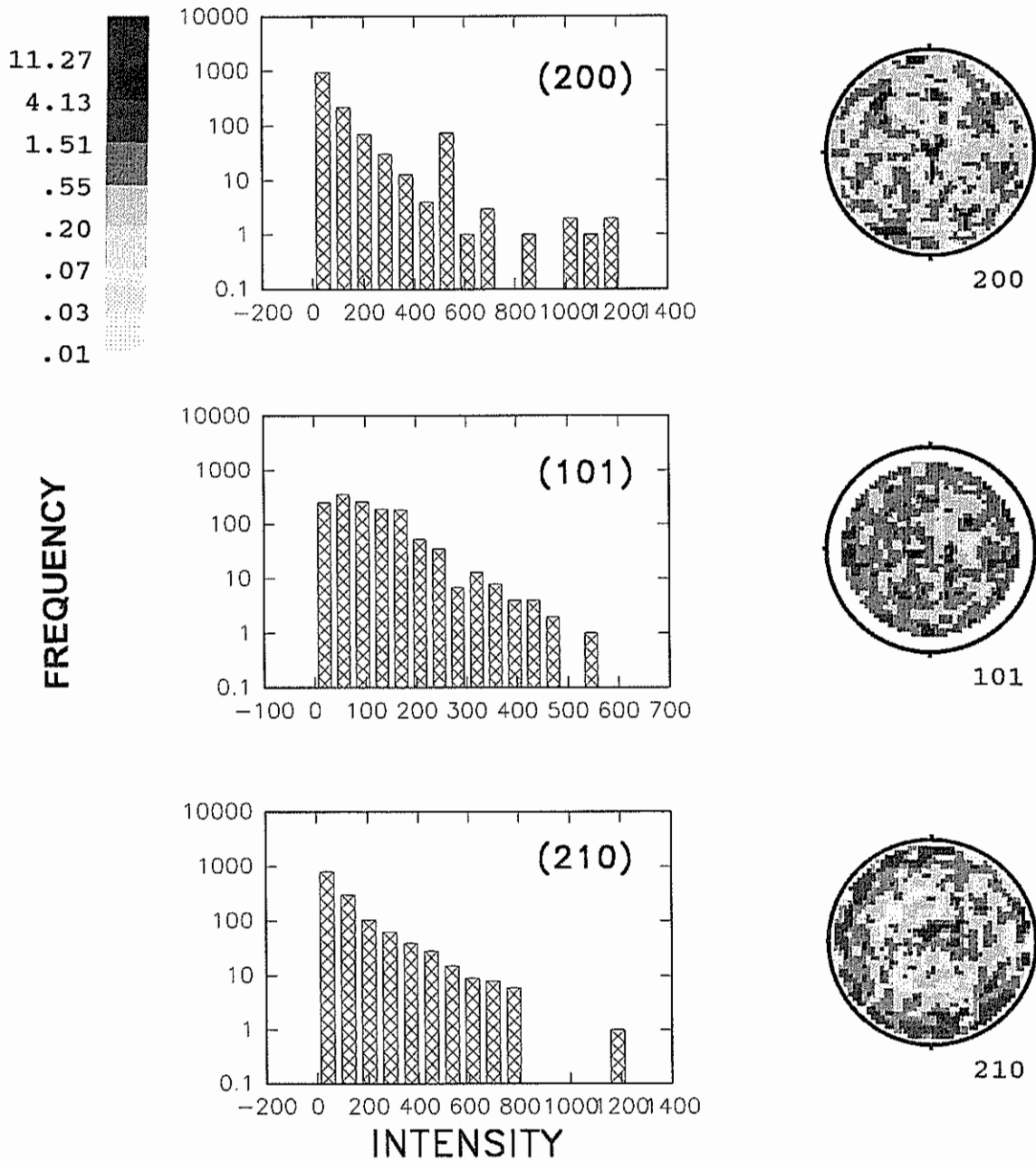
Figure 41
Pole figures and intensity distribution histograms for sample 26T'.

140
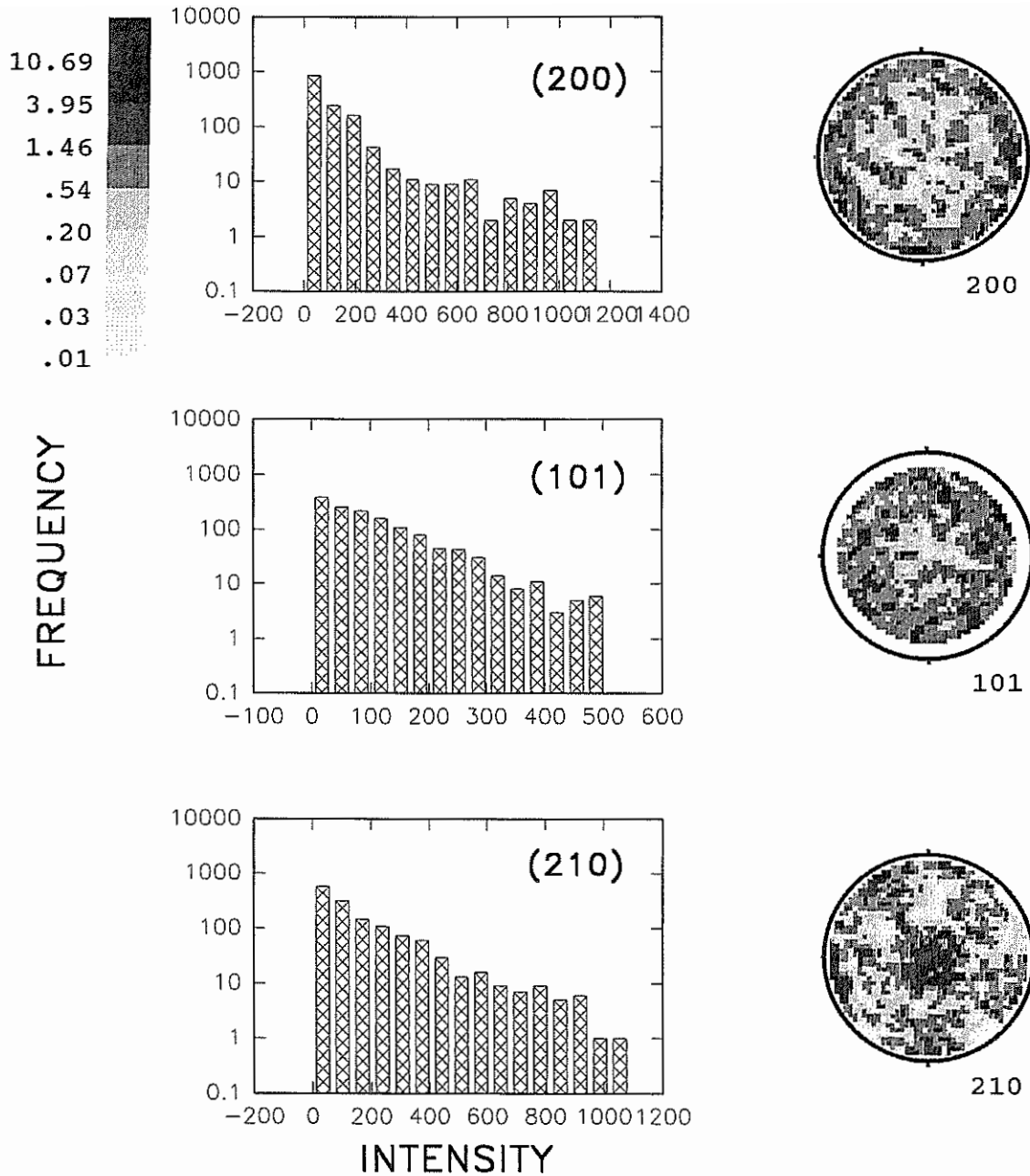
Figure 42
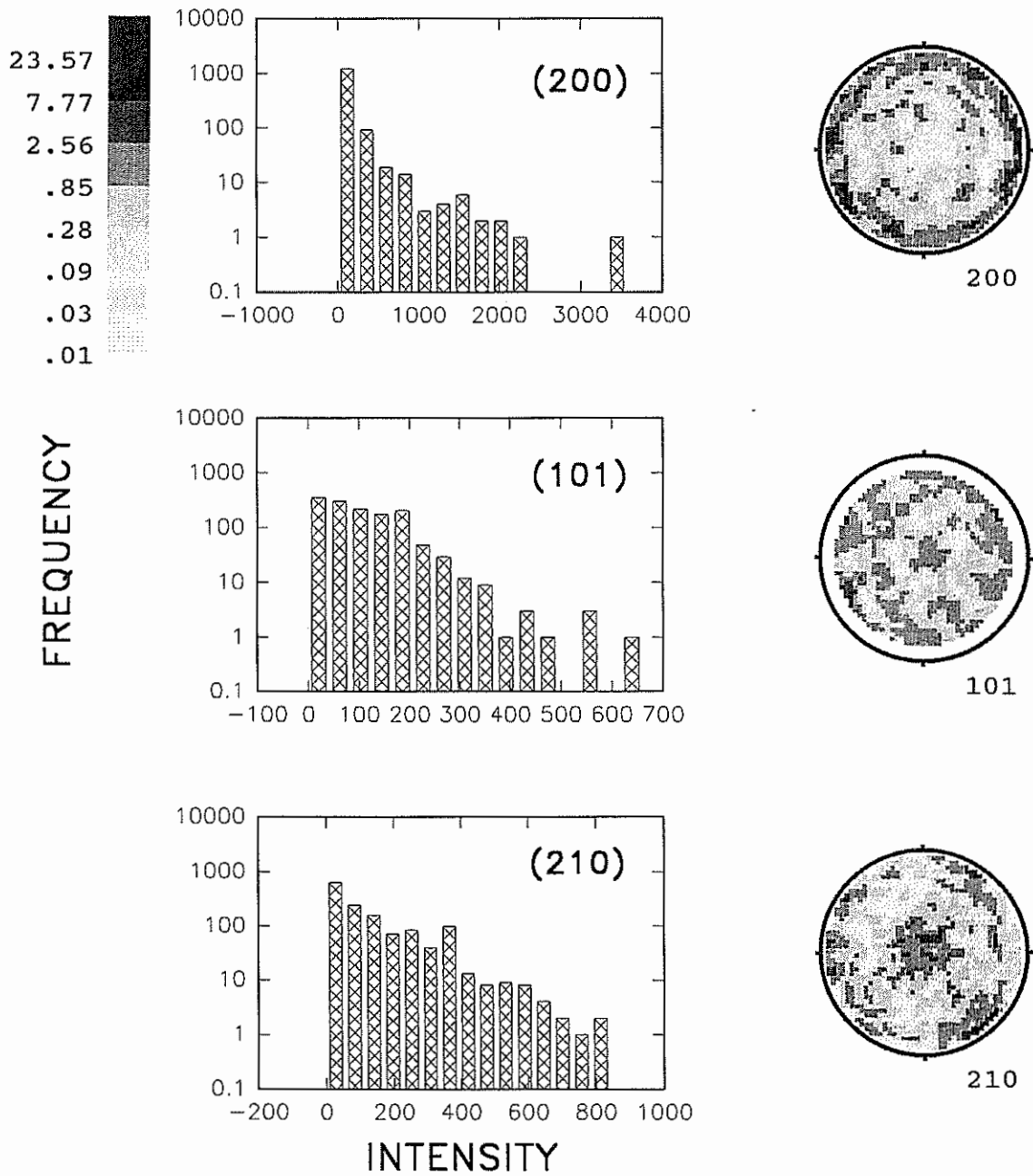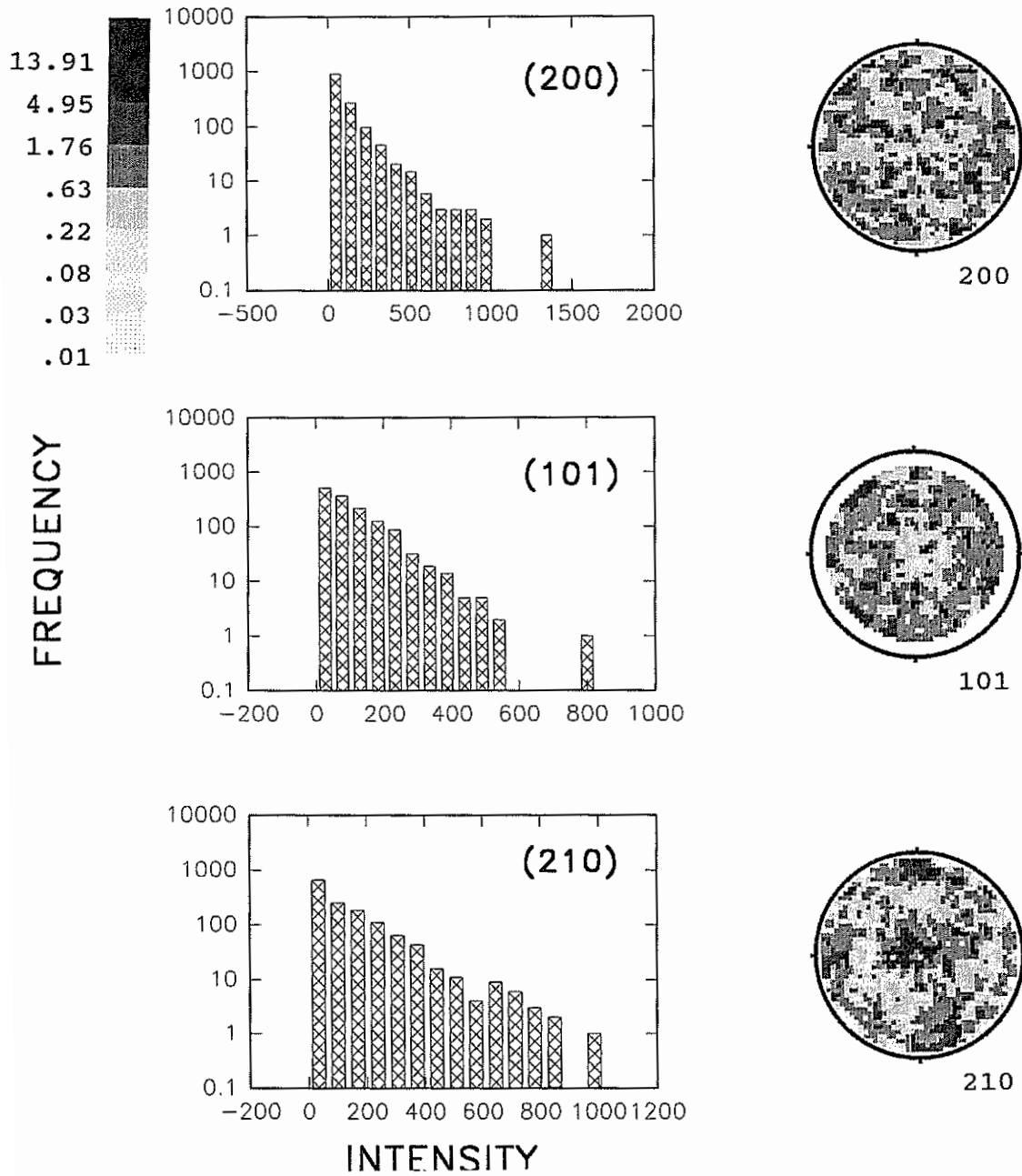Pole figures and intensity distribution histograms for sample 26T'/4.
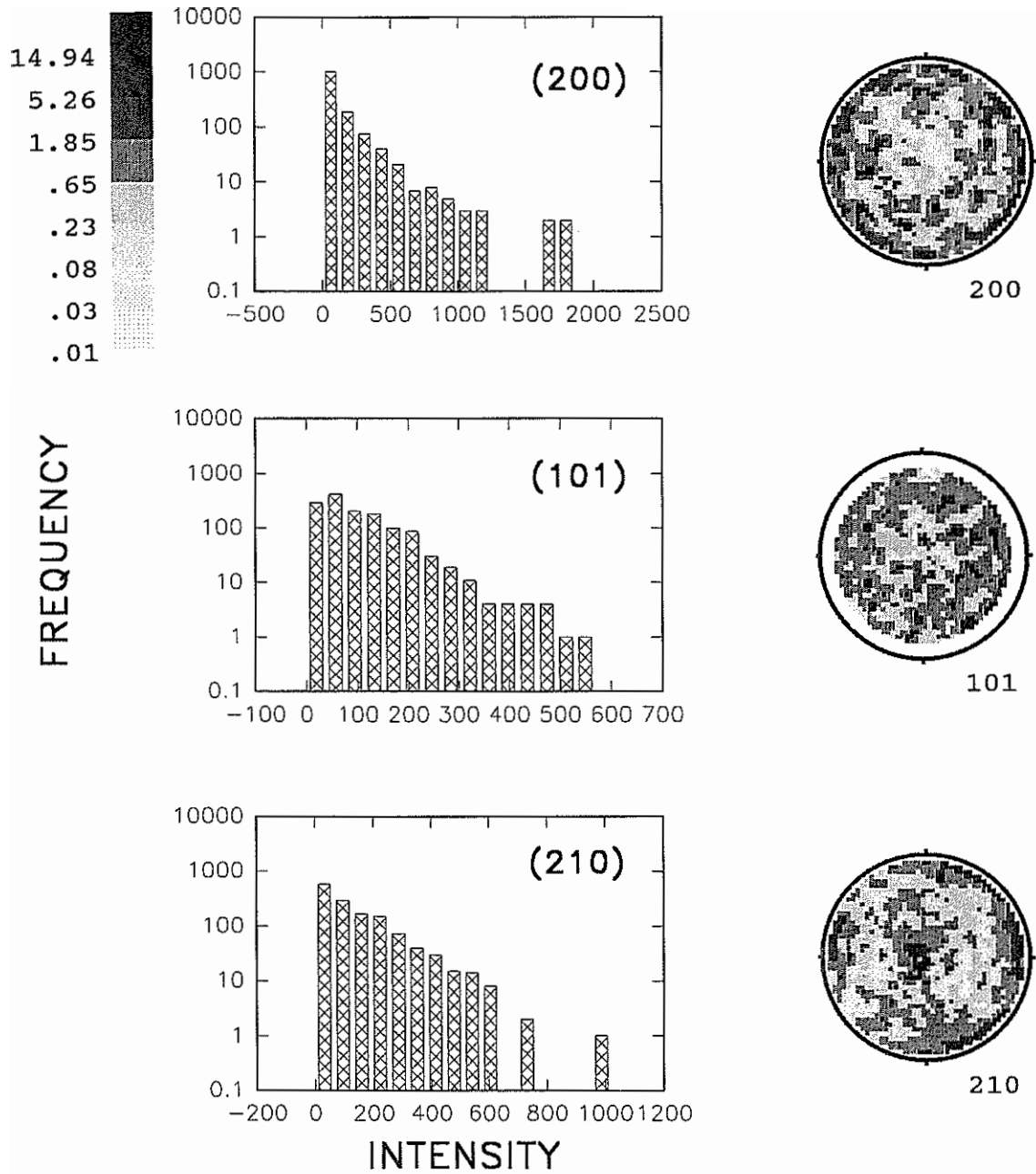
Figure 43
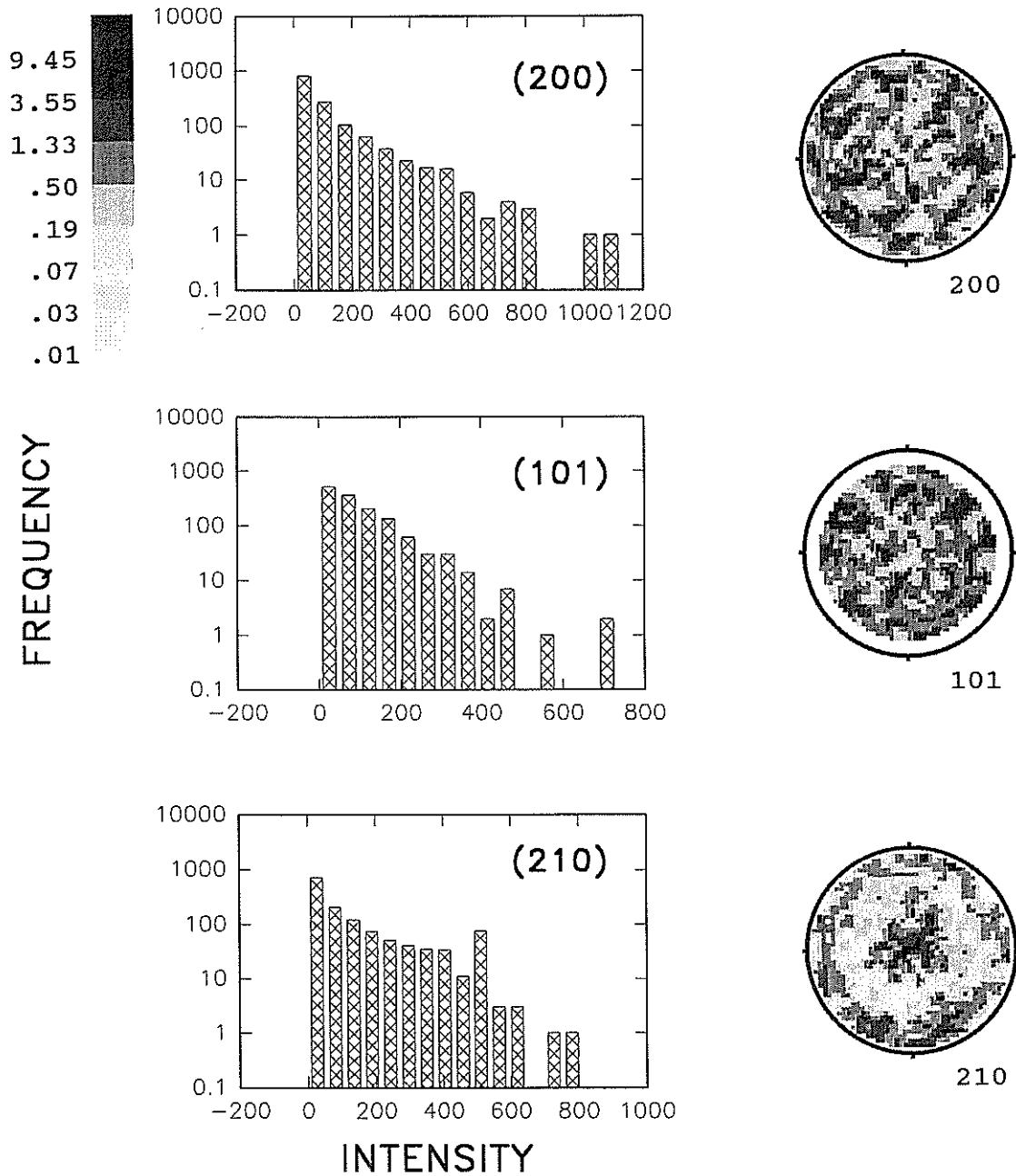Pole figures and intensity distribution histograms for sample 26T'/2.

142

CHAPTER 7

CONCLUSIONS

The principal conclusion of this research was that isothermal open die forging of Ti-25-10-3-1 in the α_2 + β phase field, followed by β solution treatment did not result in appreciable crystallographic texture development. From an engineering design standpoint, this was the desired outcome of the thermo-mechanical process employed. Hence, designs based on this material/processing combination can be assumed isotropic with regard to monotonic mechanical properties.

Metallographic investigation revealed that the thermo-mechanical processing sequence gave rise to grain refinement and reduced grain shape anisotropy, compared to the billet. Few flow lines were observed compared to the billet, giving credence to the homogeneity of flow during forging and the attendant reduction in grain shape anisotropy. However, the resulting Widmanstätten structure was finer than desired. While the general cooling was controlled, the smaller than expected plate size was attributed to the high initial cooling rate from the β solution heat treat temperature. Large (M 9.5) prior β grain sizes were consistent with typical behavior of β processed material. It should be noted that the β annealing time employed in this research was not optimized. Through

optimization, the prior β grain size should be controllable. Qualitatively, the α_2 plate distribution did not reveal any extensive texture at any location inspected.

Optical image analysis of Widmanstätten chord angle did not prove to be a useful macro-texture measurement aid. As a consequence of low angular resolution, this analysis revealed from 2 to 3 variants out of a possible 12 variants of α_2 orientation. However, this observation may also be partially attributable to transformation texturing during the cooling from β solution treatment. However, the lack of variants, coupled with the large prior β grain size and the orientation relationship of α_2 to β, severely crippled the quantitative effectiveness of XRD and x-ray pole figure investigations. This alloy with a fine Widmanstätten α_2 distribution actually displayed large grain diffraction behavior. As a result, only the qualitative conclusion from pole figures that the material was essentially non textured can be advanced.

Tensile testing in all principal directions on multiple cutting planes did not reveal strength differences unexplainable by statistical scatter or sample geometry. This was the strongest evidence supporting lack of texture in the alloy as processed.

Returning to the thermo-mechanical processing results, the dependence of flow stress on strain was observed to be consistent with material experiencing a combination of superplastic and non-superplastic deformation. Superplastic deformation is known to reduce texture. This was the most plausible explanation for the lack of texture in the forging. The resulting implication was that thermo-mechanical processing employing

144

higher strain rate, *i.e.*, in non-isothermal forging, would not be expected to give rise to a minimally textured forging with attendant isotropic tensile and creep properties.

Finally, no single experimental approach employed in this research was independently able to show minimal texture in the forging. However, taken as a group, the combination of metallographic, XRD, and tensile testing present a self consistent picture of a material with minimal texture.

REFERENCES

1. R.L. Fleisher, D.M. Dimiduk, H.A. Lipsitt, "Intermetallic Compounds for Strong High-Temperature Materials: Status and Potential", *Annu. Rev. Mater. Sci.* [19] 231-263 (1989).

2. H.A. Lipsitt, "Titanium Aluminides - An Overview", *Mat. Res. Soc. Symp. Proc.* [39] 351-364 (1985).

3. J.L. Murray, "Al-Ti (Aluminum-Titanium)", *Binary Alloy Phase Diagrams*, T.B. Massalski, Ed., ASM, Metals Park, OH, 1986.

4. M.J. Blackburn, M.P. Smith, "R&D on Composition and Processing of Titanium Aluminide Alloys for Turbine Engines", AFWL-TR-82-4086, AFWAL Mat. Lab. WPAFB, OH.

5. P.A. Blenkinsop, D.F. Neal, R.E. Goosey, "Effect of Heat Treatment on the Microstructure and Properties of IMI 685", *Titanium and Titanium Alloys*, Proceedings of the 3'd International Conf. on Titanium, Moscow State Univ., Plenum, New York, 1976 2003-2013.

6. J. Maltz, V. DePierre, *Metal Progr.* [58] 189 (1950).

7. J.V. Scanlan, G.J.G. Chambers, "Forging in Titanium Alloys", *The Science, Technology and Application of Titanium*, R.I. Jaffee, N.E. Promisel, eds., Pergamon, Oxford, 1968, 79-95.

8. J.E. Coyne, "The Beta Forging of Titanium Alloys", *The Science, Technology and Application of Titanium*, R.I. Jaffee, N.E. Promisel, eds., Pergamon, Oxford, 1968, 97-110.

9. E.A. Brandes, ed., *Smithells Metals Reference Book*, 6 ed., Butterworths, London, 1983.

10. M.J. Donachie, Jr., ed., *Titanium and Titanium Alloys Source Book*, ASM, Materials Park, OH, 1982, 222-225.

11. A.D. McQuillan, M.K. McQuillan, *Titanium*, Academic Press, New York, 1956.

12. W. Cho, A.W. Thompson, J.C. Williams, "Creep Behavior of Ti-25Al-10Nb-3V-1Mo" *Metal. Trans. A* [21A] 641-651 (1990).

13. E.W. Collings, *The Physical Metallurgy of Titanium Alloys*, ASM, Materials Park, OH, 1984.

14. G.W. Greenwood, W.E. Seeds, S. Yue, "The Isothermal Forging of Titanium Alloys for Aerospace Applications", *Forging and Properties of Aerospace Materials*, The Metals Society, London, 1978, 255-265.

15. A. Dutta, D. Banerjee, "Superplastic Behavior in a Ti₃Al-Nb Alloy", *Scripta Metall.*, [24] 1319-1322 (1990).

16. P. Bania, TIMET Corporation, private communication.

17. T.H. Quach-Kamimura, D. David, G. Béranger, "A Comparative Investigation of Oxygen Diffusion in Titanium and its Binary Alloys During Corrosion at High Temperature", *Titanium Science and Technology, Proceedings of the Fifth International Conference on Titanium*, G. Lütjering, U. Zwicker, W. Bunk, eds., Deutsche Gessellschaft Für Metallkunde E.V., 1984, 2687-2693.

18. S. Shah, "Isothermal and Hot-Die Forging", *Metals Handbook*, vol. 14, 9 ed., ASM, Materials Park, OH, 150-157.

19. D. Byrd, Cammeron Iron Works, private communication.

20. S. Reichman, Wyman-Gordon, private communication.

21. T. Watmough, K.M. Kulkarni, N.M. Parikh, "Isothermal Forging of Titanium Alloys Using Large Precision-Cast Dies" Air Force Materials Laboratory, Wright-Patterson AFB, AFML-TR-70-161 (1970).

22. J.D. Snow, C.R. Cook, "Less Materials Used Via Isothermal Forging" *ManTech J.* [5] (3) 33-41 (1980).

23. "Forging Materials: Titanium Alloys", *Forging Topics*, [37] 4-7 (1979).

24. C. Bassi, J.A. Peters, "Effect of Thermo-mechanical Processing on Microstructures and Properties of Titanium Aluminide Foils", *Scripta Metal.* [24] 1363-1368 (1990).

25. W.A. Reinsch, "Terminology for Titanium Microstructures", *Metal Progress*, Feb. 1982, 51-53.

26. J.A. Peters, C. Bassi "Isothermal Transformations in a β-Stabilized Ti₃Al Intermetallic", *Scripta Metal.* [24] 915-920 (1990).

27. R.M. Brick, R.G. Gordon, A. Phillips, *Structure and Properties of Alloys*, 3'rd ed., McGraw Hill, New York, 1965.

28. S.M.L. Sastry, H.A. Lipsitt, "Ordering Transformations and Mechanical Properties of Ti₃Al and Ti₃ Al-Nb alloys", *Metal. Trans. A* [8A] 1543-1552 (1977).

30. Rowe, R.G.; Gigliotti, M.F.X.; Marquardt, B.J.; "Creep and Discontinuous Precipitation in a Ti3Al-Nb alloy at 923 °K", *Scripta Met.* [24] 1209-1214 (1990).

31. H.M. Flower, "Microstructural Development in Relation to Hot Working of Titanium Alloys", *Mater. Sci. & Tech.* [6] 1082-1092 (1990)

32. J.A. Hall, Allied-Signal Aerospace, Garrett Engine Division, private communication.

33. D.J. Skinner, AlliedSignal Research & Technology, private communication.

34. "Microstructure of Titanium and Titanium Alloys", *Metals Handbook*, 8 ed., ASM, Materials Park, OH, [7] 1972.

35. P.J. Bania, J.A. Hall, "Creep Studies of Ti-6242-Si Alloy", *Titanium Science and Technology, Proceedings of the Fifth International Conference on Titanium*, G. Lütjering, U. Zwicker, W. Bunk, eds., Deutsche Gessellschaft Für Metallkunde E.V., 1984, 2371-2378.

36. Mishra, R.S.; Banerjee, D; "On the Influence of Cooling Rate in β Solution Treatment for a Ti-25Al-11Nb Alloy", *Scripta Metal.*, [24] 1477-1482 (1990).

37. R.W. Hayes, "On the Creep Behavior of the Ti₃Al Titanium Aluminide Ti-25Al-10Nb-3V-1Mo", *Acta Metal.* [39] (4) 569-577 (1991).

38. M.A. Stucke, H.A. Lipsitt, "The Effects of Heat Treatment on the Fatigue Crack Growth Behavior of Ti₃Al + Nb", *Titanium, Rapid Solidification Technology*, TMS-AIME, Warrendale, PA, 1986, 255-262.

39. D.L. Davidson, J.B. Campbell, R.A. Page, "The Initiation and Growth of Fatigue Cracks in a Titanium Aluminide Alloy", *Metal. Trans. A* [22A] 377-391 (1991).

40. T.L. Wardlaw, Timet, Letter of 23 December 1991 to R.G. Rateick, Jr.

41. M. Khan, Wyman-Gordon Company, Fax of 3/29/92 to R.G. Rateick, Jr.

42. C. Huang, Z. Chen, T.A. Dean, M.H. Loretto, "Hot Upset Forging of Ti_3Al Base Superalpha-2 Alloy", *Mater. Sci. Tech.* [9] 737-741 (1993).

43. E. Siebel, *Stahl und Eisen,* [43] 1295 (1923).

44. R. Hill, *The Mathematical theory of Plasticity*, Oxford, London, 1950.

45. W. Schroeder, D.A. Webster, "Press-Forging Thin Sections: Effects of Friction, Area, and Thickness on Pressures Required", *J. Appl. Mech.* [16] 289-294 (1949).

46. S.L. Semiatin, J.J. Jonas, *Formability and Workability of Metals, Plastic Instability and Flow Localization*, ASM, Metals Park, OH, 1984.

47. S.I. Oh, S.L. Semiatin, J.J. Jonas, "An Analysis of the Isothermal Hot Compression Test", *Metal. Trans A* [23A] 963-975 (1992).

48. S.L. Semiatin, G.D. Lahoti, "Deformation and Unstable Flow in Hot Forging of Ti-6Al-2Sn-4Zr-2Mo-0.1Si", *Metall. Trans. A* [12A] 1705-1717 (1981).

49. S.L. Semiatin, P.A. McQuay, V. Seetharaman, "A Novel Process for Breakdown Forging Coarse-Grain Intermetallic Alloys", *Scripta. Metal.* [29] 1235-1240 (1993).

50. P.K. Chaudhury, D. Zhao, "Atlas of Formability of Super α_2 Titanium Aluminide", Naval Industrial Resources Support Activity, NTIS No. AD-A268 321.

51. H.S. Yang, P. Jin, E. Dalder, A.K. Mukherjee, "Superplasticity in a Ti_3Al-Base Alloy Stabilized by Nb, V and Mo", *Scripta Metal.* [25] 1223-1228 (1991).

52. G.J. Davies, J.W. Edington, C.Pl Cutler, K.A. Padmanebhan, "Superplasticity: A Review", *J. Mater. Sci.* [5] 1091-1102 (1970).

53. A. Dutta, D. Banerjee.; "Suprplastic Behaviour in a Ti_3Al-Nb Alloy", *Scripta Metal.* [24] 1319-1322 (1990).

54. J.C.F. Millett, J.W. Brooks, I.P. Jones, "The Isothermal Forging of the Ti_3Al Based Alloy Superalpha 2", *Titanium '92 Science and Technology,* Proceedings of the Seventh World Converence on Titanium, San Diego, CA, 28 June - 2 July 1992, F.H. Froes, I.L. Caplan, eds., TMS, Warrendale, PA, 979-986.

55. C. McCullough, J.J. Valencia, C.G. Levi, R. Mehrabian, "Phase Equilibria and Solidification in Ti-Al Alloys", *Acta. Metall.*, [37] (5) 1321-1336 (1989)

56. J.C. Mishurda, J.H. Perpezko, "Phase Equilibria in Ti-Al Alloys", *Microstrucure/Property Relationships in Titanium Aluminides and Alloys*, Y-W Kim, R.R. Boyer, eds., TMS, Warrendale, PA, 1991.

57. H. Lipsit, Private Communication, Titanium 7, 1992.

58. R. Strychor, J.C. Williams, W.A. Soffa, "Phase Transformations and Modulated Microstructures in Ti-Al-Nb Alloys", *Metal. Trans. A* [19A] 225-234 (1988).

59. D. Banerjee, A.K. Gogia, T.K. Nandi, V.A. Joshi, "A New Ordered Orthorhombic Phase in a Ti$_3$Al-Nb Alloy", *Acta Metal.* [36] (4) 871-882 (1988).

60. H.T. Kestner-Weykamp, C.H. Ward, T.F. Broderick, M.J. Kaufman, "Microstructures and Phase Relationships in the Ti$_3$Al-Nb System", *Scripta Metal.* [23] 1697-1702 (1989).

61. H.I. Aaronson, "The Proeutectoid Ferrite and the Proeutectoid Cementite Reactions", *Decomposition of Austenite by Diffusional Processes*, V.F. Zackay, H.I. Aaronson, eds., Interscience Publishers, New York, 1962, 387-546.

62. H.M. Ottte, "Mechanism of the Martensitic Transformation in Titanium and its Alloys", *The Science, Technology and Application of Titanium*, R.I. Jaffee, N.E. Promisel, eds., Pergamon Press, Oxford, 1970, 645-657.

63. E.W. Collings, *The Physical Metallurgy of Titanium Alloys*, American Society of Metals, Metals Park, Oh., 1984.

64. C.H. Ward, Jr., "Deformation and Fracture of the Alloy Ti-25Al-10Nb-3B [*sic*, V] -1Mo", PhD Thesis, Carnegie Mellon University, Pittsburgh, PA, 1992, (WL-TR-92-4104).

65. W.G. Burgers, *Physica* [1] 561 (1934).

66. H.T. Weykamp, D.R. Baker, D.M. Paxton, M.J. Kaufman, "Continuous Cooling Transformations in Ti$_3$Al + Nb Alloys", *Scripta Metal.* [24] 445-450 (1990).H.T.

67. J.W. Christian, *The Theory of Transformations in Metals and Alloys*, Pergamon Press, Oxford, 1965.

68. J. Béchet, C. Angelier, B. Cormier, O. Lacagne, M. Lhermitte, "Phase Transformations in a Near β - Ti Alloy: Microstrudture and Mechanical

Properties", *Titanium '92 Science and Technology*, Proceedings of the Seventh World Conference on Titanium, San Diego, CA, 28 June - 2 July 1992, F.H. Froes, I.L. Caplan, eds., TMS, Warrendale, PA, 643-654.

69.   J.C. Chesnutt, C.G. Rhodes, J.C. Williams, "Relationship Between Mechanical Properties, Microstructure, and Fracture Topography in $\alpha + \beta$ Titanium Alloys", *Fractography-Microscopic Cracking Processes, ASTM STP 600*, American Society for Testing and Materials, 1976, 99-138.

70.   C.G. Rhodes, J.C. Williams, "Observations of an Interface Phase in the α/β Boundaries in Titanium Alloys", *Metal. Trans. A* [6A] 1670-1671 (1975).

71.   W.J. Porter, R.R. Boyer, D. Eylon, "Effects of Microstructure on the Mechanical Properties of Ti-15V-3Cr-3Al-3Sn", *Titanium '92 Science and Technology*, Proceedings of the Seventh World Conference on Titanium, San Diego, CA, 28 June - 2 July 1992, F.H. Froes, I.L. Caplan, eds., TMS, Warrendale, PA, 1511-1518.

72.   J.E. Allison, W. Cho, J.W. Jones, W.T. Donlon, J.V. Lasecki, "The Influence of Elevated Temperature on the Mechanical Behaviour of α/β-Titanium Alloys", *Proc. 6th World Conf. on Ti, France* 293-298 (1988).

73.   *Titanium and its Alloys*, P.C. database developed by the Titanium Information Group and the Titanium Development Association.

74.   Z.X. Guo, T.N. Baker, "On the Mirostructure and Thermo-Mechanical Processing of Titanium Alloy IMI685, *Mater. Sci. Engr.* [A156] 62-76 (1992).

75.   G.F. Vander Voort, *Metallography Principles and Practice*, McGraw-Hill, Inc., New York, 1984.

76.   *Metallogrpahy Principles and Procedures*, Leco, Corp., St. Joseph, Mi.

77.   E.E. Underwood, *Quantitative Stereology*, Addison-Wesley, Reading, MA, 1970.

78.   J.G. Byrne, *Recovery, Recrystallization, and Grain Growth*, Macmillan, New York, 1965.

79.   D.A. Lukasak, D.A. Koss, "The Flow and Fracture of a Ti3Al-Nb Alloy", *Metal. Trans.* [21A] 135-143 (1990).

80.   Z.S. Zhu, J.L. Gu, N.P. Chen, "On the Phase Transformation Texture in Commercially Pure Titanium Sheet", *Scripta Metal.* [30] (5) 605-609 (1994).

81. M. Humbert, H. Moustahfid, F. Wagner, M.L. Philippe, "Evaluation of the High Temperature Texture of the β Phase of a TA-6V [*sic, Ti*] Sample from the Individual Orientations of Grain of the Low Temperature α Phase", *Scripta Metal.* [30] 377-382 (1994).

82. H.R.Ogden, D.J. Maykuth, W.L. Finlay, R.I. Jaffee, "Constitution of Titanium-Aluminum Alloys", *Trans. AIME, J.O.M.* [191] 1150-1155 (1951).

83. E.S. Bumps, H.D. Kessler, M. Hansen, "Titanium-Aluminum System", *Trans. AIME, J.O.M.,* [194] 609-614 (1952).

84. R.G. Baggerly "X-Ray Analysis of Ti₃Al Precipitation in Ti-Al Alloys" *Adv. X-Ray Anal.* [18] 502-513 (1977).

85. M.J. Marcinkowski, "Theory and Direct Observation of Antiphase Boundaries and Dislocations in Superlattices", *Electon Microscopy and Strength of Crystals*, G. Thmoas, J. Washburn, eds., Interscience, New York, 1963, 333-440.

86. E. Ence, H. Margolin, "Compounds in the Titanium-Rich Region of the Ti-Al System", *Trans. AIME* [209] 484 (1957).

87. J.L. Murray, "Al-Ti", *Binary Alloy Phase Diagrams*, T.B. Massalski, ed., American Society for Metals, Metals Park, OH, 1986.

88. A.J. Goldak, J.Gordon Parr, "The Structure of Ti₃Al", *Trans. AIME* [221] 639-640 (1961).

89. E. Ence, H. Margolin, "Phase Relations in the Titanium-Aluminum System", *Trans. AIME* [221] 151-157 (1961).

90. D. Clark, K.S. Jepson, G.I. Lewis "A Study of the Titanium-Aluminum System up to 40 at% Aluminum", *J. Inst. Metal.* [91] 197-203 (1962-63).

91. L.A. Bendersky, W.J. Boettinger, A. Roytburd, "Coherent Precipitates in the BCC/Orthorhombic Two-Phase Field of the Ti-Al-Nb System", *Acta Metall.* [39] (8) 1959-1969 (1991).

92. C. Suryanarayana, D.S. Lee, "Phase Relations in Ti-Al-Nb Alloys at 1200°C", *Scripta Met. Mater.* [26] (6) 919-924 (1992).

93. R. Strychor, J.C. Williams, "Phase Transformations in Ti-Al-Nb Alloys", *Solid Solid Phase Transformations*, H.I. Aaronson, *et.al.*, eds., TMS, Warrendale, PA, 249-253, 1982.

152

94. R.Strychor, J.C. Williams. W.A. Soffa, "Phase Transformations and Modulated Microstructures in Ti-Al-Nb Alloys", *Metal. Trans. A* [19A] 225-234 (1988).

95. M.A. Morris, "Creep and High Temperature Deformation of Titanium Aluminide Alloys: Influence of α_2 Phase Distribution and B2 Phase Decomposition", *Matl. Sci. Engr.* [A148] 33-43 (1991).

96. L.A. Bendersky, W.J. Boettinger, B.P. Burton, F.S. Biancaniello, C.B. Shoemacker, "The Formation of Ordered ω-related **Phases** in Alloys of Composition Ti_4Al_3Nb", *Acta Metall.* [38] (6) 931-943 (1990).

97. L.M. Hsiung, H.N.G. Wadley, "A New Ordered Tetragonal Phase in the Ti_3Al+Nb System", *Scripta Met.* [26] 35-40 (1992).

98. D.J. Skinner, AlliedSignal Research & Technology, unpublished research.

99. P. Villars, L.D. Calvert, eds., *Pearson's Handbook of Crystallographic Data for Intermetallic Phases*, ASM, Metals Park, OH, 1985, p3238.

100. Diano SPG-2 operating manual page 24 figure 8.

101. Lambda Research Report 629-0-001, "Pole Figure Analysis of the Alpha-2 Phase in Six Ti-Al Forging Specimens". Work performed under contract from AlliedSignal Aerospace Company, Bendix Engine Controls Division.

102. M.U. Cohen, *Rev. Sci. Instr.* [6] 68ff (1935) and [7] 155ff (1936).

103. B.D. Cullity, *Elements of X-Ray Diffraction*, 2nd. ed., Addison-Wesley, Reading, MA, 1978.

104. A.J. Bradley, A.H. Jay, *Proc. Phys. Soc. (London)*, [44] 563 (1932).

105. L.P. Lehman, *The Influence of Phosphorous on the Isothermal Ordering Kinetics of Ni_2Cr*, PhD dissertation University of Notre Dame, May 1987.

106. E.F. Kaelble, ed., *Handbook of X-Rays For Diffraction, Emission, Absorption, and Microscopy*, McGraw Hill, New York, 1967.

107. J.D.H. Donnay, H.M. Ondik, eds., *Crystal Data Determinative Tables*, 3d ed., NSRDS.

108. D.E. Gray, ed., *American Institute of Physics Handbook*, 3d ed., McGraw-Hill, New York, 1972, p4-131.

109. D. Hull, D.J. Bacon, *Introduction to Dislocations*, 3d ed., Pergamon, Oxford, 1984.

110. R. von Mises, *Z. angew. Math. Mech.*, [8] 161 (1928).

111. A.T. Churchman, "The Slip Modes of Titanium and the Effect of Purity on their Occurance During Tensile Deformation of Single Crystals", *Proc. Roy. Soc.* [226A] 216 (1954).

112. T.R. Cass, "Slip Modes and Dislocation Substructrues in Titanium and Titanium-Aluminum Single Crystals", *The Science, Technology and Application of Titanium*, R.I. Jaffee, N.E. Promisel, eds., Pergamon, Oxford, 1970, 459-477.

113. E.A. Anderson, D.C. Jillson, S.R. Dunbar, "Deformation Mechanisms in Alpha Titanium", *Trans. AIME*, [197] 1191-1197 (1953).

114. F.D. Rosi, C.A. Dube, B.H. Alexander, "Mechanism of Plastic Flow in Titanium-Determination of Slip and Twinning Elements", *Trans. AIME*, [197] 257-265 (1953).

115. A.T. Churchman, "The Slip Modes of Titanium and the Effect of Purity on their Occurance During tensile Deformation of Single Crystals", *Proc. Roy. Soc.*, [226A] 216-227 (1954)

116. M.J. Blackburn, J.C. Williams, "Strength, Deformation Modes and Fracture in Titanium-Aluminum Alloys", *Trans. ASM*, [62] 398-409 (1969).

117. H.A. Lipsitt, D. Shechtman, R. E. Schafrik, "The Deformation and Fracture of Ti_3Al at Elevated Temperatures", *Metal. Trans.* [11A] 1369-1375 (1980).

118. S.M.L. Sastry, H.A. Lipsit, "Plastic Deformation of TiAl and Ti_3Al", *Titnium '80 Science and Technology, Proceedings of the Fourth International Conference on Titanium, Koyoto, Japan, May 19-22, 1980*, Metallurgical Society of AIME, Warrendale, Pa, 1980, 1231-1243.

119. B.J. Marquardt, G.K. Scarr, J.C. Chesnutt, C.G. Rhodes, H.L. Fraser, Deformation in Alpha-2 Titanium Alloys", *Sixth World Conference on Titanium: Proceedings, Cannes, June 6-9, 1988*, Les Editions de Physique, Cedex Rrance, 1989, 955-960.

120. E. Schmidt, W. Boas, *Plasticity of Crystals, With Special Reference to Metals*, tr., Chapman & Hall, London, 1968.

121. S.A. Court, J.P.A. Löfvander, M.H. Loretto, H.L. Fraser, "The Influence of Temperature and Alloying Additions on the Mechanisms of Plastic Deformation

of Ti₃Al", *Phil. Mag. A*, [61] (1) 109-139 (1990).

122. Z. Chen, F. Simca, M.T. Cope, "Microstructure and tensile Properties of Aged Superalpha 2 Intermetallic Compound", *Mater. Sci. Tech.* [8] 729-738 (1992).

123. R.J. Kerans, "Deformation in Ti₃Al Fatigued at Room and Elevated Temperatures", *Metal. Trans. A* [15A] 1721-1729 (1984).

124. G. Malakondaiah, T. Nicholas, "The Influence of Laser Glazing on Fatigue Crack Growth in Ti-24Al-11Nb", *Metal. Trans.* [25A] 183-192 (1994).

125. W.P. Hon, S.K. Wu, C.H. Koo, "The Tensile Properties of a Textured Ti65Al25Nb10 Alloy", *Mater. Sci. Eng.* [A131] 85-91 (1991).

126. C.D. Beachem, R.M.N. Pelloux, "Electron Fractography -- a Tool for the Study of Micromechanims of Fracturing Processes", *Fracture Toughness Testing and its Applications, STP 381*, ASTM, Philadelphia, 1965, 210-245.

127. K.S. Chan, "Influence of Microstructure on Intrinsic and Extrinsic Toughening in an Alpha-Two Titanium Aluminide Alloy", *Metal. Trans.* [23A] 183-199 (1992).

128. R.B. Abernethy, J.E. Breneman, C.H. Medlin, G.L. Rinman, "Weibull Analysis Handbook", Aero Propulsion Laboratory, Wright-Patterson AFB, AFWAL-TR-83-2079, AD-A143 100, Final Report, Nov. 1983.

129. M.J. Donachie, Jr., *Titanium, A Technical Guide*, ASM International, Metals Park, OH, 1988.

130. D.S. McDarmaid, A.W. Bowen, P.G. Partridge, "Tensile Properties of Strongly Textured Ti-6Al-4V After Superplastic Deformation", *Mater. Sci. Engr.* [64] 105-111 (1984).

131. G. Lütjering, J. Albrecht, A. Gysler, "Mechanical Properties of Titanium Alloys", *Titanium '92 Science and Technology*, Proceedings of the Seventh World Conference on Titanium, San Diego, CA, 28 June - 2 July 1992, F.H. Froes, I.L. Caplan, eds., TMS, Warrendale, PA, 1635-1646, 1993.

132. H. Inagaki, "Evolution of Textures and Microstructres in Thermo-Mechanical Processing of Ti-6Al-4V", *Z. Metallkde.* [81] (6) 433-445 (1990).

133. I.M. Sukonnik, S.L. Semiatin, M.Haynes, "Effect of Texture on the Cold Rolling Behavior of an Alpha-Two Titanium Aluminide", *Scripta. Metal.* [26] 993-998 (1992).

134. R. Verma, A.K. Ghosh, "Microstructural and TexturalChanges During Rolling of Alpha-2 Titanium Aluminide Foils", *Titanium '92 Science and Technology*, Proceedings of the Seventh World Conference on Titanium, San Diego, CA, 28 June - 2 July 1992, F.H. Froes, I.L. Caplan, eds., TMS, Warrendale, PA, 995-1002, 1993.

135. J. Kumpfert, C.H. Ward, Y.T. Lee, M. Peters, "Improvement of Ductility and Strength of Ti-25Al-10Nb-3V-1Mo by TMT", *Titanium '92 Science and Technology*, Proceedings of the Seventh World Conference on Titanium, San Diego, CA, 28 June - 2 July 1992, F.H. Froes, I.L. Caplan, eds., TMS, Warrendale, PA, 1685-1692, 1993.

136. M. Humbert, H. Moustahfid, F. Wagner, M.L. Philippe, "Evaluation of the High Temperature Texture of the β Phase of a TA-6V Sample from the Individual Orientations of Grain of the Low Temperature α Phase", *Scripta Metal.* [30] 377-382 (1994).

137. A.W. Bowen, D.S. McDarmaid, P.G. Partridge, "Effect of High-Temperature Deformation on the Texture of a Two-Phase Titanium Alloy", *J. Mater. Sci.* [26] 3457-3462 (1991).

138. Z.S. Zhu, J.L. Gu, N.P. Chen, "On the Phase Transformation Texure in Commercially Pure Titanium Shet, *Scripta. Metal.* [30] (5) 605-609 (1994).

139. C.P. Cutler, J.W. Edington, "Textures in the Superplastically Deformed Tin-Lead Eutectic Alloy", *Metal Sci. J.*, [5] 201-205 (1971).

140. K.N. Melton, J.W. Edington, J.S. Kallend, C.P. Cutler, "Textures in Superplastic Zn-40 wt.% Al", *Acta Met.* [22] 165-170 (1974).

141. K.N. Melton, J.W. Edington, "Crystallographic Slip During Superplastic Deformation of the Zn-Al Eutectoid Alloy", *Scripta. Metal.* [8] (10) 1141-1144 (1974).

142. K. Matsuki, H. Moriata, M. Yamada, Y. Murakami, "Relative Motion of Grains During Sperplastic Flow in an Al-9Zn-1 wt%Mg Alloy", *Metal Science* [11] 156-163 (1977).

143. D.S. McDarmaid, A.W. Bowen, P.G. Partridge, "Superplastic Deformation of Strongly Textured Ti-6Al-4V", *J. Mater. Sci.* [19] 2378-2386 (1984).

144. L.G. Schultz, "A Direct Method of Determining Preferred Orientation of a Flat Reflection Sample Using a Geiger Counter X-Ray Spectrometer", *J. Appl. Phys.*

[20] 1030-1033 (1949).

145. W.P. Chernock, P.A. Beck, "Analysis of Certain Errors in the X-Ray Reflection Method for the Quantitative Determination of Preferred Orientations", *J. Appl. Phys.* [11] (3) 341-345 (1952).

146. J.S. Kallend, U.F. Kocks, A.D. Rollett, H.-R. Wenk, "Operational Texture Analysis", *Mater. Sci. Eng.* [A132] 1-11 (1991).

147. S. Matthies, G.W. Vinel, "On the Reproductionof the Orientation Distribution Function of textureized Samples from Reduced Pole figures using the Conception of a Conditional Ghost Correction", *Phys. Status Solidi B*, [112] K111-K120 (1982).

148. M.M. Klenck, "A Simplified Method of Quantitating Preferred Orientation", *Advances In X-Ray Analysis*, [11] 447-453 (1968).